Two-layer Heisenberg model of quasi-2D triangular lattice antiferromagnet and study of the magnetoelastic coupling in $Ba_3CoSb_2O_9$ using sound velocity measurements

by

© **Ming Li**

A thesis submitted to the School of Graduate Studies in partial fulfillment of the requirements for the degree of Doctor of Philosophy.

Department of Physics and Physical Oceanography

Memorial University

September 2020

St. John's, Newfoundland and Labrador, Canada

Abstract

The magnetic field evolution of ground spin states of the stacked planar triangular antiferromagnet with antiferromagnetic interlayer interaction J_c is explored using a minimal 3D classical Heisenberg model (published in Ref. [1]). A bi-quadratic coupling is also used to mimic the effect of spin fluctuations [2] which are known to stabilize the magnetization plateau. A single ion anisotropy is included and states with a magnetic field applied in the ab-plane and along the c-axis are determined. For $\mathbf{H} \parallel ab$-plane, an additional state, in contrast to the 2D model [2], is obtained with weak interlayer interaction. Meanwhile the magnetization plateau decreases with the increment of J_c and vanishes at medium values of J_c. Moreover, two new states with a small z components of spins emerge with large J_c. For $\mathbf{H} \parallel c$-axis, an extra state, compared with the 2D model, is obtained with a weak interlayer interaction. When J_c is large enough, only the state corresponding to the Umbrella phase in the 2D model exists.

High-resolution ultrasonic measurements are used to study magnetoelastic coupling as a function of the inplane magnetic field orientation in the spin-1/2 triangular lattice antiferromagnet $Ba_3CoSb_2O_9$ (published in Ref. [3]). Via these measurements, the relevance of this coupling in stabilizing the 1/3 magnetization plateau (up-up-down state) is explored. The analysis indicates that, while the magnetoelastic coupling in $Ba_3CoSb_2O_9$ is large, in comparison to other triangular lattice antiferromagnets, the strength of this coupling is still too small to fully account for the magnetization

plateau width in $Ba_3CoSb_2O_9$. Spin fluctuations are therefore the dominant mechanism inducing and stabilizing the magnetization plateau. Our results also show that the amplitude of the spin fluctuations suddenly drops as the V phase is induced at higher field. Furthermore, as the temperature approaches the uud phase boundary from the paramagnetic state, the short range spin correlation, responsible for the softening of the acoustic modes, are also observed. Comparing the experimental results in ordered states at different temperatures, our results indicate that the effect of the thermal fluctuations on the magnetoelastic coupling are negligible at low temperatures in comparison to that of the quantum fluctuations.

General summary

In magnetic materials, the magnetic properties are mainly decided by the neighboring magnetic moments, usually related to the spins of electrons. When the temperature is higher than a critical temperature, called the Néel temperature (T_N) or Curie temperature (T_C), the interaction between the magnetic moments is negligible, which is known as the paramagnetic state. In typical antiferromagnetic materials with $T < T_N$, the nearest neighboring magnetic moments lie in antiparallel alignment due to the interaction. However, considering an equilateral triangle formed by three magnetic ions, the three magnetic moments cannot be antiparallel to each other at the same time. These materials, comprised of equilateral triangular sublattices, are called geometrically frustrated antiferromagnets, such as triangular lattice antiferromagnets (TLAF). Quasi two dimensional TLAF are composed of stacked basal planes formed by triangular sublattices, in which the interaction between the interlayer nearest neighboring magnetic ions is much smaller than the interaction between the nearest neighboring magnetic ions in the basal plane. The quasi-2D TLAF have been widely studied in recent decades, since they show an impressive variety of exotic magnetic ground states.

Although the intra-plane interaction in the quasi-2D TLAF is dominant, the weak interlayer interaction still plays an important role. Therefore, we explore the effects of the interlayer interaction with different values in the quasi-2D TLAF using a 3D

classical Heisenberg model. Moreover, the mechanism, which is derived from spin fluctuations or lattice distortion, are included for stabilizing the magnetic ground states. Compared with 2D model, new ground states are obtained with the interlayer interaction.

$Ba_3CoSb_2O_9$ is a typical quantum quasi-2D TLAF, in which quantum and thermal fluctuations are considered to stabilize the magnetic ground states. While the spin-lattice coupling (magnetoelastic coupling) is also an important mechanism, which is studied using high-resolution ultrasonic measurements in $Ba_3CoSb_2O_9$ at different low temperatures and applied magnetic fields. The experimental results show that the spin fluctuations not only dominate stabilizing the magnetic ground states, but also present strong effects on the magnetoelastic coupling. Furthermore, the results at the two lowest temperatures indicate that the quantum fluctuations are dominant while the thermal fluctuations are negligible.

Acknowledgements

I would like to express my great appreciation to my supervisor, Dr. Guy Quirion, for his guidance through the process of my PhD. Working with him in the lab has been a great experience, as he shows unlimited passion and experimental knowledge. Actually, I have learned much more, since Dr. Quirion is not only an experienced and knowledgeable physicist, but also a very serious scholar.

I am very grateful to my co-supervisor, Dr. Martin L. Plumer, for his guidance, the theoretical model he provided and the helpful discussion. Especially, without the mean-field model Dr. Plumer has studied for decades, we cannot understand what we obtained in the ultrasonic measurement.

I wish to acknowledge Dr. Jeffrey Quilliam for providing the equipment of the sound velocity measurements in his lab, and Mr. Mario Castonguay for the technical support.

I would like to express my appreciation to our collaborators, Dr. Haidong Zhou and Dr. Zhiling Dun, who provided $Ba_3CoSb_2O_9$ sample for our measurements.

I would like to acknowledge Dr. Jolanta B. Lagowski and Dr. Anand Yethiraj, the members in my PhD committee, for their advice on my research.

It is a pleasure to thank all staffs in Department of Physics and Physical Oceanography for their help for my work.

I am thankful to all my friends in Canada. Especially, Mr. Carl Hansen provides much help for my life in St. John's, and helped me develop my hobby, photography, to be my part-time job.

At last, I would like to express my gratitude to my family, my wife Jing Wang, my parents and parents-in-law, for their endless support and encouragement.

Table of contents

List of tables

List of figures

Chapter 1

Introduction

1.1 Geometrical frustration

In typical antiferromagnets, nearest neighbour spins form collinear configuration with their magnetic moments antiparallel to each other. However, for some geometries, such as three atoms forming an equilateral triangle, not all neighbouring spins can be antiparallel at the same time to form the lowest energy state. Thus, due to their geometry these antiferromagnets are said to be geometrically frustrated (as illustrated in Fig. 1.1(a)). Due to this frustration, the ground state energy of a triangular lattice antiferromagnet (with nearest-neighbor exchange) is known to be minimized by forming a non-collinear configuration with spins at an angle of 120° relative to each other, leading to two degenerate chiral states shown in Fig. 1.1(b) and (c). This type of magnetic configuration has been effectively observed in many geometrically frustrated systems based on triangular and kagomé lattice types (Figure 1.2(a) and (b)); while more complicated frustrated systems such as the four-neighbor pyrochlore lattice (1.2(c)) lead to more complex non-collinear spin configurations. Therefore,

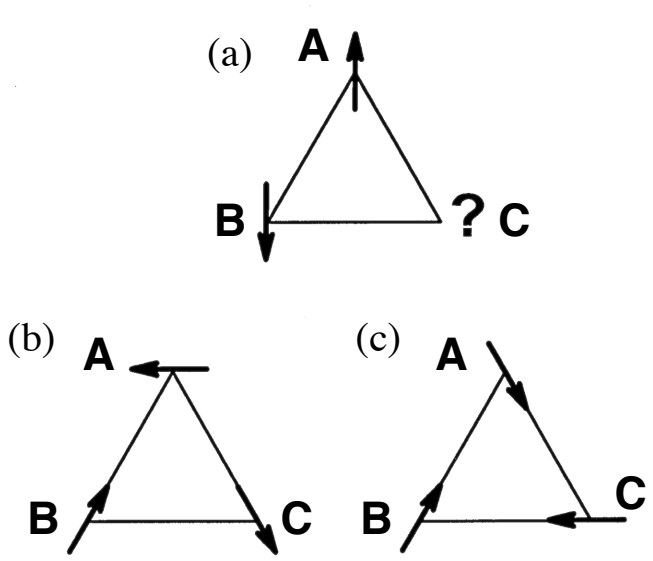

Figure 1.1: Frustrated triangular lattice antiferromagnet [4]. (a) shows the geometric frustration; (b) and (c) are two 120° degenerate chiral states.

frustrated magnets have been widely studied in recent decades because they show an impressive variety of exotic magnetic ground states [4, 12–16].

Due to the degeneracy associated with frustration, a lower temperature is needed for the ordering of the spin system to take place. Since the scale for magnetic ordering in a typical antiferromagnet can be estimated by the Curie-Weiss temperature Θ_{CW} [17], by comparing Θ_{CW} with the critical temperature T_c, an empirical measurement of the level of frustration can be determined by the frustration parameter [13], defined as

$$f = \frac{|\Theta_{CW}|}{T_c}. \tag{1.1}$$

Here, $f > 1$ corresponds to a suppression of the ordering of the spins, as a result of frustration. In the extremely frustrated limit $f = \infty$, the spins keep fluctuating and avoid ordering even at $T = 0$ K, which applies for spin liquids [18–25], such as

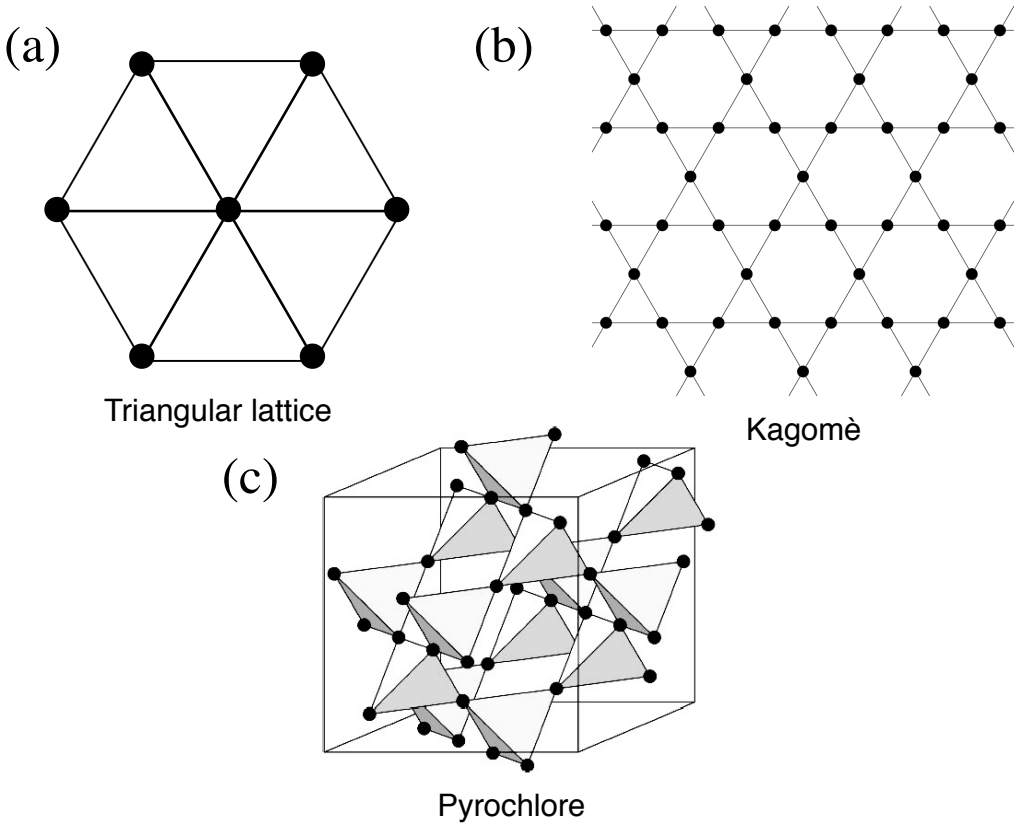

Figure 1.2: Three kinds of geometrically frustrated antiferromagnets: (a) triangular lattice, (b) kagomé lattice, (c) pyrochlore lattice.

$Tb_2Ti_2O_7$ [26–29], $YbMgGaO_4$ [30–32] and $ErMgGaO_4$ [33, 34]. Spin ice state, which is analogous to the configurations and the positions of protons and O^{2-} in water ice, is another example of exotic ground state due to frustration. Each O^{2-} in water ice has two near protons with covalent bonds, and two further protons with hydrogen bonds [35]. Analogously, in each tetrahedron comprised by magnetic ions as shown in Fig. 1.3, the four magnetic Ising moments are along their local $\langle 111 \rangle$ axes, with two spins pointing inward and the other two pointing outward from the centre of the tetrahedron. In several pyrochlore lattice materials, such as $Ho_2Ti_2O_7$ [36, 37], $Dy_2Ti_2O_7$ [38, 39] and $Ho_2Sn_2O_7$ [40], the spin ice states have been discovered at low

temperatures.

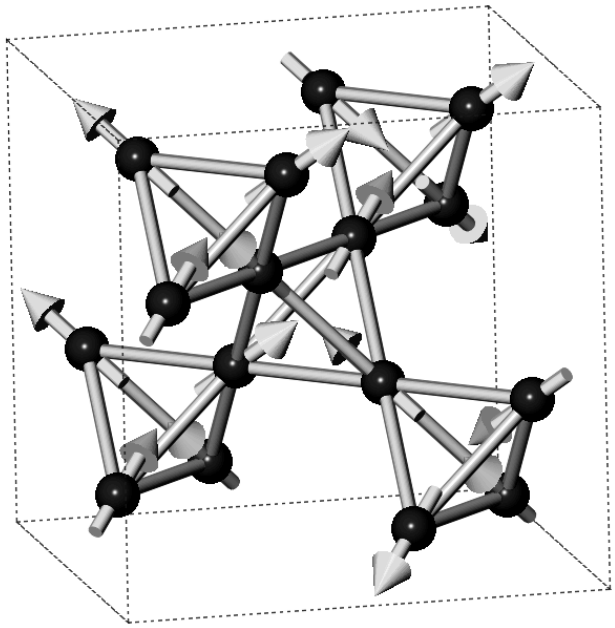

Figure 1.3: The spin ice states with the two-in and two-out spin configuration in each tetrahedron are shown in the pyrochlore lattice of corner-sharing tetrahedra.

1.2 Stacked triangular lattice antiferromagnets

For the triangular lattice antiferromagnets (TLAF), while the effects of frustration are mostly understood by now, there has been renewed interest due to the observation of a magnetization plateau (see Fig. 1.4 and Fig. 1.5) in a variety of TLAFs [6,41–47]. So far, magnetic materials composed of stacked triangular lattices have been widely studied, including quasi-1D and quasi-2D materials with easy-plane or easy-axis anisotropy or other types of anisotropy [4]. Quasi-1D magnetic systems, such as quasi-1D TLAF $CsNiCl_3$ [48–51], have been well described by classical models. While the observation of magnetization plateau in quasi-2D TLAFs, well below the saturation limit, is

accounted for by different mechanisms. As an example, the magnetization plateau observed with magnetic field applied normal to the basal plane of $Rb_4Mn(MoO_4)_3$ with spin-5/2 [52, 53], is stabilized by the easy-axis anisotropy. In contrast, different mechanisms are needed to explain the magnetization plateaus induced by the in-plane field in the TLAFs with easy-plane anisotropy as follows. Cs_2CuBr_4 [42,54–56], which has spin-1/2, is the first quasi-2D TLAF compound showing a magnetization plateau; however, the triangular lattice is slightly distorted. This distortion, in that case, can therefore be partially responsible for the magnetization plateau along with spin fluctuations. While, for TLAF with equilateral triangular lattice, such as $RbFe(MoO_4)_2$ with spin-5/2 [44, 45, 57–63] and $Ba_3CoSb_2O_9$ with spin-1/2 [6, 46, 64–66], the mechanism accounting for the magnetization plateau is believed to be attributed to spin fluctuations [2, 67, 68]. Finally, it has been proposed that strong magnetoelastic coupling [69–73] can also lead to the observation of a magnetization plateau.

The magnetic phase diagram by M. V. Gvozdikova *et al.* [5], determined from Monte Carlo simulations using a classical Heisenberg model for isotropic 2D TLAFs, is shown in Fig. 1.4. According to these simulations and other numerical works [8,74–76], the anticipated spin configurations are illustrated in Fig. 1.4, which are consistent with the experimental results with $\mathbf{H} \parallel ab$ plane as shown in Fig. 1.5. At $\mathbf{H} = 0$, the spins adopt a 120° configuration in the basal plane. At low field, a so-called Y state corresponds to a configuration where two moments are at some angle relative to the field while the other is opposed to the field direction. At intermediate field values, the magnetization plateau is associated with the up-up-down (uud) state where two spins are parallel to magnetic field while the third one is antiparallel. Finally the V_{xy} state has two parallel spins with an angle less than 180° with respect to the third spin. As shown in Fig. 1.6, these predictions compare well with recent experimental results obtained for the spin-1/2 easy-plane quasi-2D TLAF $Ba_3CoSb_2O_9$ where T_N

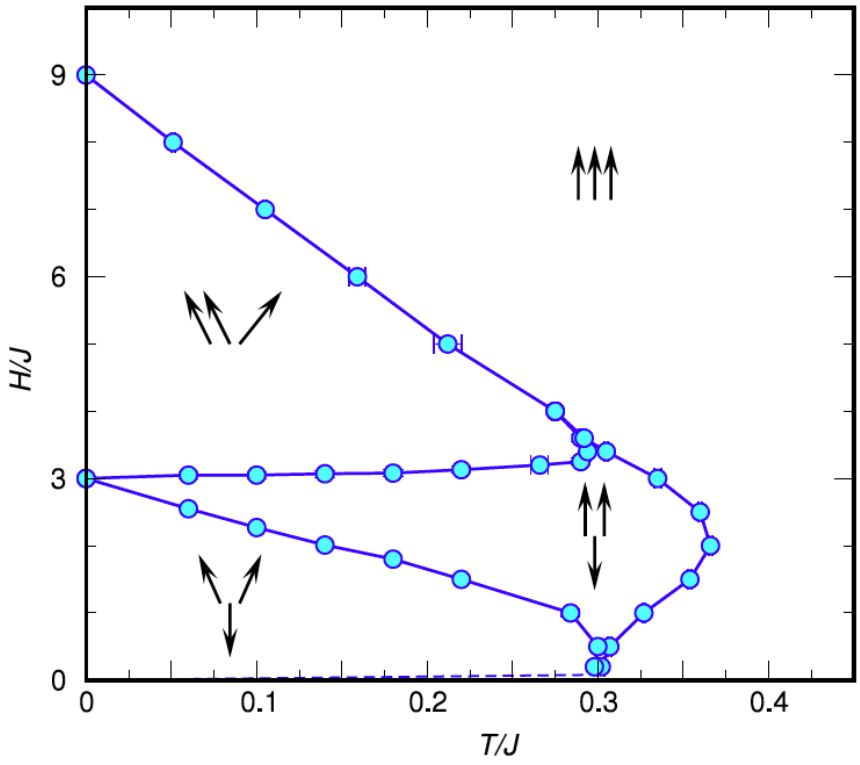

Figure 1.4: The H-T phase diagram of TLAFs determined using Monte Carlo simulations by Gvozdikova *et al.* [5]. Reprinted with permission from [M V Gvozdikova, P-E Melchy, and M E Zhitomirsky, Journal of Physics: Condensed Matter, 23(16):164209, 2011]. Copyright (2011) by Institute of Physics.

= 3.8 K [9]. While this simple classical model accounts well for the observed phase sequence as a function of the field, as well as a magnetization plateau associated with the collinear uud state for $T > 0$ K [5], it fails considerably at $T = 0$ K where the width of the magnetization plateau collapses, in contradiction with the experimental observations (Fig. 1.6 [9]). Considering that thermal fluctuations, which is known as entropic order by disorder mechanism [67,68], generally favor collinear states [5,68,75], it has been proposed and shown that quantum fluctuations can be the mechanism for lifting the classical degeneracy in favor of the uud state at $T = 0$ K [74, 75, 77].

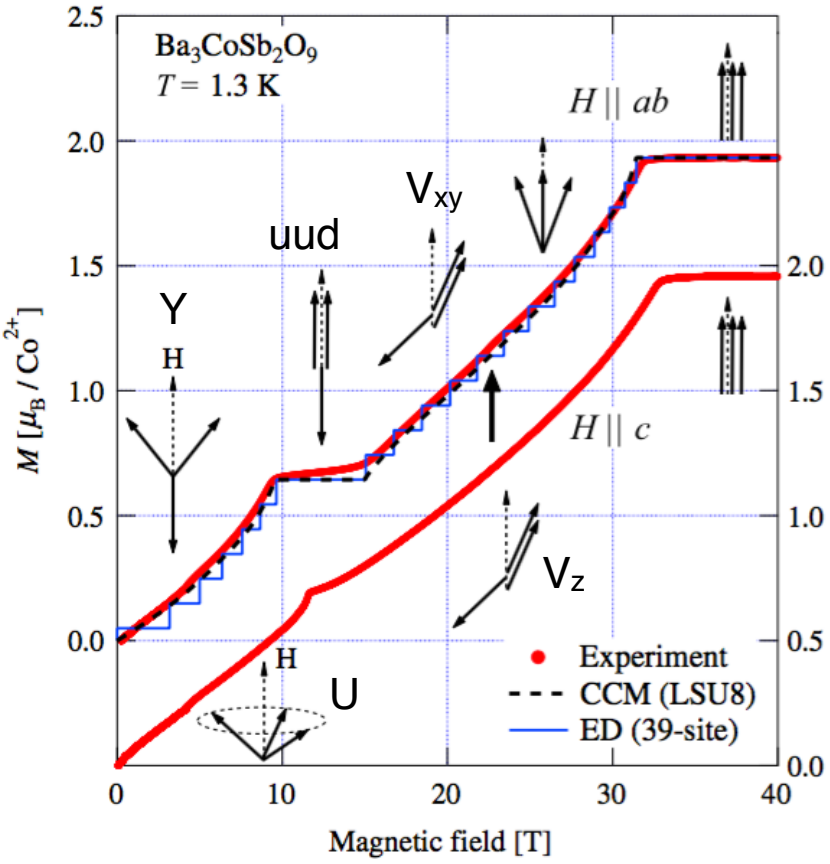

Figure 1.5: Magnetization processes of $Ba_3CoSb_2O_9$ at 1.3 K for **H** $\parallel$ ab-plane (left) and **H** $\parallel$ c-axis (right) [6]. The dashed black and solid blue lines represent the results of a higher-order coupled cluster method (CCM) [7] and exact diagonalization (ED) for a 39-site rhombic cluster [8], respectively. Reprinted with permission from [Takuya Susuki, Nobuyuki Kurita, Takuya Tanaka, Hiroyuki Nojiri, Akira Mat- suo, Koichi Kindo, and Hidekazu Tanaka, Phys. Rev. Lett., 110:267201, 2013]. Copyright (2013) by American Physical Society.

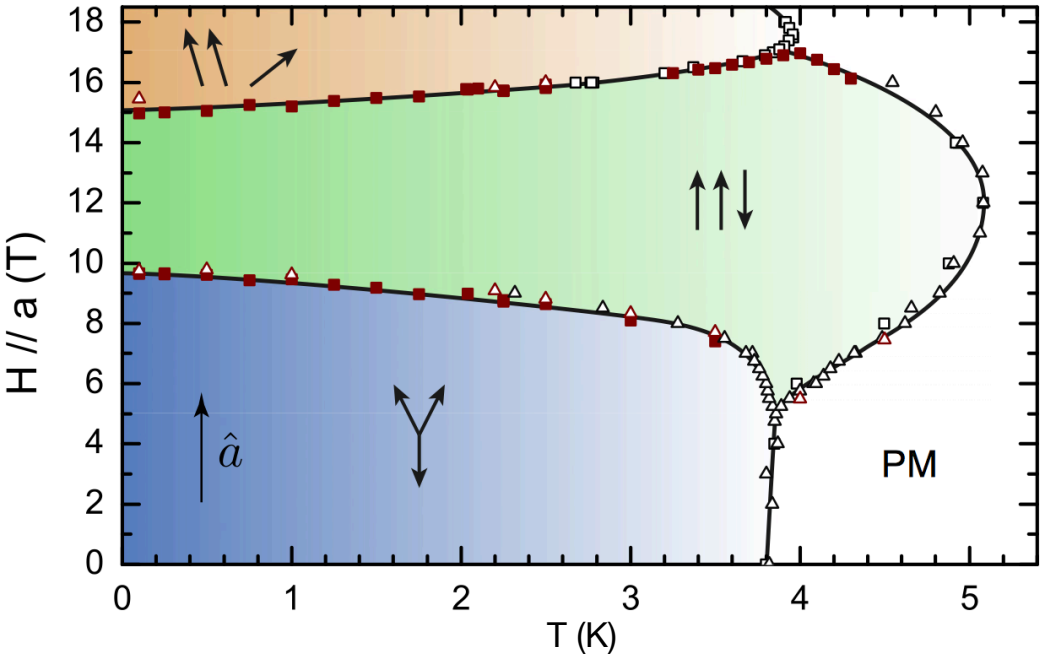

Figure 1.6: Experimental H-T phase diagrams of $Ba_3CoSb_2O_9$ obtained by ultrasonic measurements for **H** $\parallel$ a-axis [9]. Reprinted with permission from [G. Quirion, M. Lapointe-Major, M. Poirier, J. A. Quilliam, Z. L. Dun, and H. D. Zhou, Phys. Rev. B, 92:014414, 2015]. Copyright (2015) by American Physical Society.

1.3 Properties of $Ba_3CoSb_2O_9$

As a paradigmatic quantum quasi 2D TLAF, $Ba_3CoSb_2O_9$ is an ideal crystal to explore the contribution of the spin fluctuations and the magnetoelastic coupling for lifting the classical degeneracy and stabilizing the magnetization plateau. In this chapter, we present the properties of $Ba_3CoSb_2O_9$, including the crystal symmetry, the nearest-neighbor exchange coupling, spin value and anisotropy, which is applied in the mean-field model used for analyzing the experimental results in Chapter 7.

The hexagonal crystal structure of $Ba_3CoSb_2O_9$ with space group $P6_3/mmc$ [64,78] is shown in Fig. 1.7. The Co^{2+} ions, located at the center of the blue octahedrons comprised of O^{2-}, form a perfect triangular lattice which are stacked directly on top of each other [6]. Due to the double layers of nonmagnetic Sb^{5+} ions, the intralayer nearest-neighbor exchange interaction $J_{ab} = 18$ K is nearly two orders of magnitude larger than the interlayer interaction $J_c = 0.48$ K [6]. Moreover, due to the spin-orbit coupling and uniaxial crystal field, the magnetic properties of Co^{2+} ions at low temperatures ($T \lesssim 250$ K) are determined by the lowest Kramers doublets [46]. As a result, Co^{2+} ions in $Ba_3CoSb_2O_9$ have an effective spin equal to 1/2. Thus, so far $Ba_3CoSb_2O_9$ is probably the best prototype of a spin-1/2 triangular antiferromagnetic frustrated quantum system. This is supported by magnetization measurements which show a well defined magnetization plateau (Fig. 1.5) for a field applied in the basal plane at a value that corresponds to 1/3 M_s, where M_s represents the saturation magnetization. However, for a field applied along the c-axis, while there is also a magnetic phase transition around the same field value, no plateau is observed [6]. The experimental results of Ref. [6] also indicate the magnetic anisotropy of $Ba_3CoSb_2O_9$ is of the easy-plane type.

We present in Figure 1.8 the magnetic phase diagram of $Ba_3CoSb_2O_9$ determined

by sound velocity measurements [9] with a sketch of the spin configurations determined from neutron scattering at low fields [66], while at higher fields they are derived from numerical models [11]. From the experiment results, it is known that $Ba_3CoSb_2O_9$ begins to order at a critical temperature $T_N = 3.8$ K at $H = 0$ and forms the expected 120° phase in the ab plane [9,46,47] with a magnetic wave vector $\mathbf{Q} = (1/3, 1/3, 1)$ [47]. With an increasing magnetic field $\mathbf{H} \parallel ab$-plane, Y, uud and V states in the basal plane are shown in Fig. 1.8. Due to the easy-plane anisotropy, the observed spin orders are different with $\mathbf{H} \parallel c$-axis. As shown in Fig. 1.8, the umbrella state (U state) corresponds to a state where the spins adopt a 120° configuration in the ab-plane with a uniform component along the c-axis (the field direction in this case). At higher field another V_z state is observed with all spins lying in a plane including the c-axis. These results at low temperatures shown in Fig. 1.8 agree with the numerical work with $J/J_c < 0.06$ presented in Chapter 3.

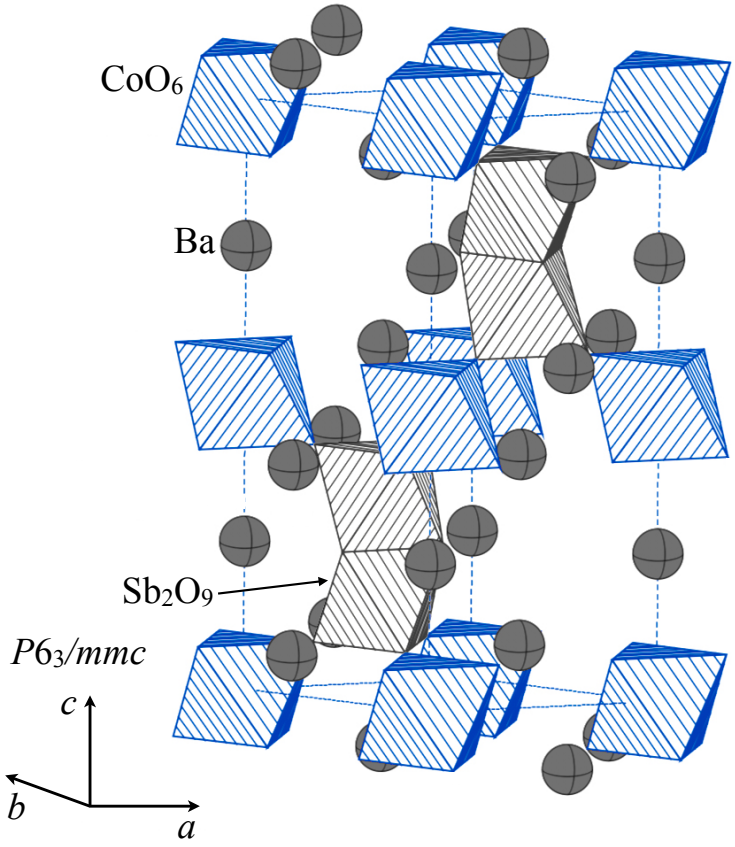

Figure 1.7: Crystal structure of $Ba_3CoSb_2O_9$. The magnetic Co^{2+} ions, located at the center of the blue octahedrons comprised of O^{2-}, form a perfect triangular lattice [6]. The double layers of nonmagnetic Sb^{5+} ions locate between two planes of the magnetic ions.

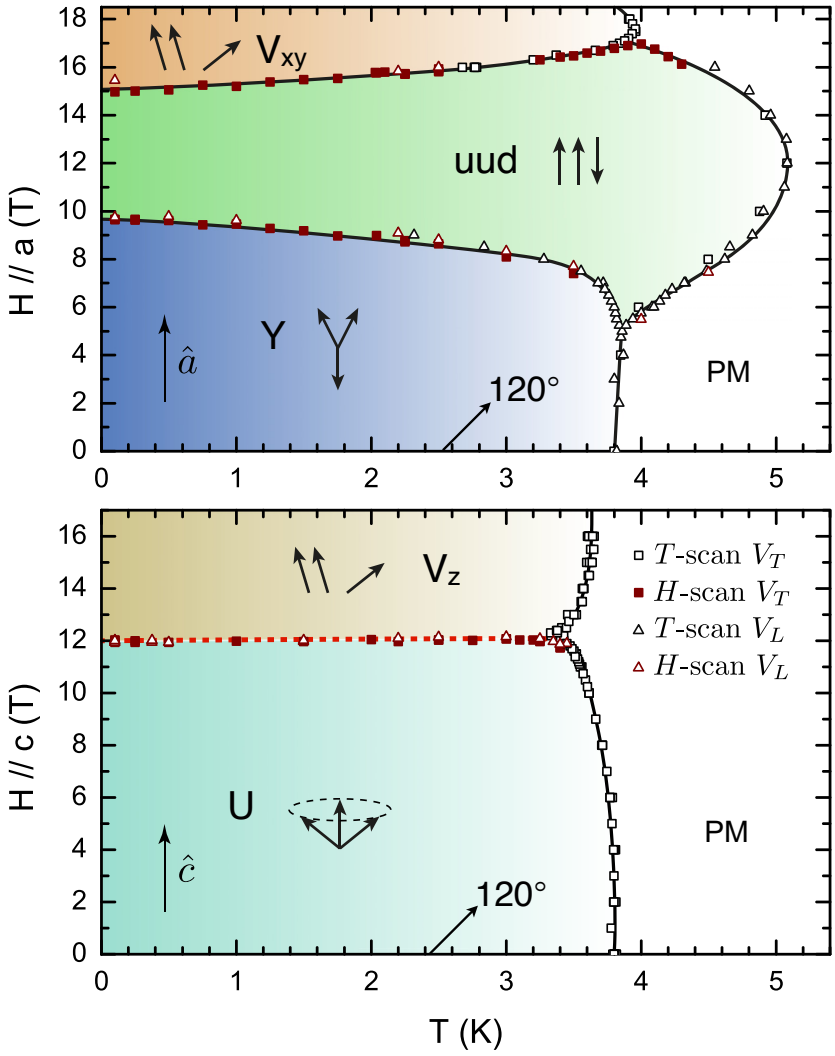

Figure 1.8: Experimental H-T phase diagrams of $Ba_3CoSb_2O_9$ obtained by ultrasonic measurements for $\mathbf{H} \parallel a$-axis and $\mathbf{H} \parallel c$-axis [9]. Reprinted with permission from [G. Quirion, M. Lapointe-Major, M. Poirier, J. A. Quilliam, Z. L. Dun, and H. D. Zhou, Phys. Rev. B, 92:014414, 2015]. Copyright (2015) by American Physical Society.

1.4 Motivation

In order to mimic effect of spin fluctuations, which is important for stabilizing the magnetization plateau of the equilateral TLAF with easy-plane anisotropy (see Section 1.2), we includes a bi-quadratic exchange coupling between nearest-neighbour ions within the basal plane [2, 79] in the Heisenberg model. Meanwhile, as shown in Fig. 1.5, the magnetization anomaly observed near 3/5 M_s in $Ba_3CoSb_2O_9$ with $\mathbf{H} \parallel ab$-plane indicates an extra phase [6, 80] between uud and V states which could be accounted for by a weak interlayer exchange coupling [11, 74]. As we will show, this classical approach allows us to study in detail the effects of interlayer interaction. Furthermore, as the bi-quadratic exchange coupling term, responsible for the magnetization plateau, can also be associated with the spin-lattice coupling (magnetoelastic coupling) [69–73], the strength of this possible contribution is explored experimentally via ultrasonic velocity measurements in $Ba_3CoSb_2O_9$. Finally, a mean field model, in which the symmetry of hexagonal lattice is taken into consideration, is applied to analyze the experimental results.

1.5 Thesis outline

The remainder of this thesis is organized as follows. We first present the H-T phase diagrams with $\mathbf{H} \parallel x$-axis and $\mathbf{H} \parallel z$-axis using a Landau model in Chapter 2. This same model will be expanded in order to analyzed the effect of the magnetoelastic coupling on the sound velocity data presented in Chapter 7. In Chapter 3, we explore the effects of interlayer and bi-quadratic exchange coupling on layered triangular lattice antiferromagnets using a 3D Heisenberg model (the subject of our publication Ref. [1]). The ultrasonic measurement, which is used for exploring the magnetoelastic

coupling of $Ba_3CoSb_2O_9$ sample (the subject of our publication Ref. [3]), is described in Chapter 4. Then, the experimental setup and the results of the field angular dependence of relative velocity variation, $v(\phi)/v$, measured at constant temperatures and fields are presented in Chapter 5. In order to analyze the experimental results, a mean-field model which explicitly takes into account the magnetoelastic coupling for a hexagonal lattice structure is presented in Chapter 6. In Chapter 7, we show the analysis of experimental results for the magnetoelastic coupling and spin fluctuations. Finally, a summary and conclusions are contained in Chapter 8.

Chapter 2

Landau model

2.1 Introduction to Landau model

2.1.1 Landau free energy and order parameter

Landau model is a macroscopic mean-field model which gives a phenomenological description of both first order and second order phase transitions without knowing the microscopic causes of the phase transitions [81]. In Landau theory, phase transitions are described by an order parameter which is nonzero in the ordered state and zero in the disordered state. Furthermore, in our work describing magnetic phase transitions, it is assumed that the Gibbs free energy can be expanded in a power series of the order parameter (S), as given by

$$G = c_1 S + c_2 S^2 + c_3 S^3 + c_4 S^4 + c_5 S^5 + c_6 S^6 + ..., \tag{2.1}$$

where S is the local magnetic moment. In order to explore a real system, the symmetries of the system must be satisfied. As one of the most important characteristics, the

time reversal symmetry changes the sign of the odd powers of S due to the property of pseudo-vector. Thus, only even powers of the order parameter are allowed. The Landau free energy reduces to

$$F_L = \frac{A}{2}S^2 + \frac{B}{4}S^4 + \frac{C}{6}S^6, \tag{2.2}$$

when ignoring the higher order terms. Moreover, it is assumed that only the coefficient A is temperature dependent and defined as

$$A = a\left(T - T_0\right), \tag{2.3}$$

where T_0 is a transition temperature. In order to change the sign of A at T_0 corresponding to a phase transition, a is set to be a positive constant. For a stable state, the coefficient of the highest order term must be positive ($C > 0$). Finally, the sign of the coefficient B (Eq. 2.2) then determine whether the character of the transition is first or second order.

2.1.2 Second order phase transition

For $B > 0$, only the first two terms of Eq. 2.2 are needed in most second order phase transitions, hence

$$F_L = \frac{A}{2}S^2 + \frac{B}{4}S^4. \tag{2.4}$$

Minimizing Eq. 2.4 relative to S, we obtain

$$\frac{\partial F_L}{\partial S} = S(A + BS^2) = 0, \tag{2.5}$$

with two solutions,

$$S = \begin{cases} 0, & \text{for } T > T_0 \\ \sqrt{-\frac{A}{B}}, & \text{for } T \leq T_0, \end{cases} \tag{2.6}$$

where

$$A = a(T - T_0) \tag{2.7}$$

with $a > 0$. For $T > T_0$, the system has its minimum energy with $S = 0$ which corresponds to the disordered phase. The solution below T_0 describes the ordered state where the order parameter temperature dependence is given by,

$$S = \sqrt{a(T_0 - T)/B}, \tag{2.8}$$

and shown in Fig. 2.1.

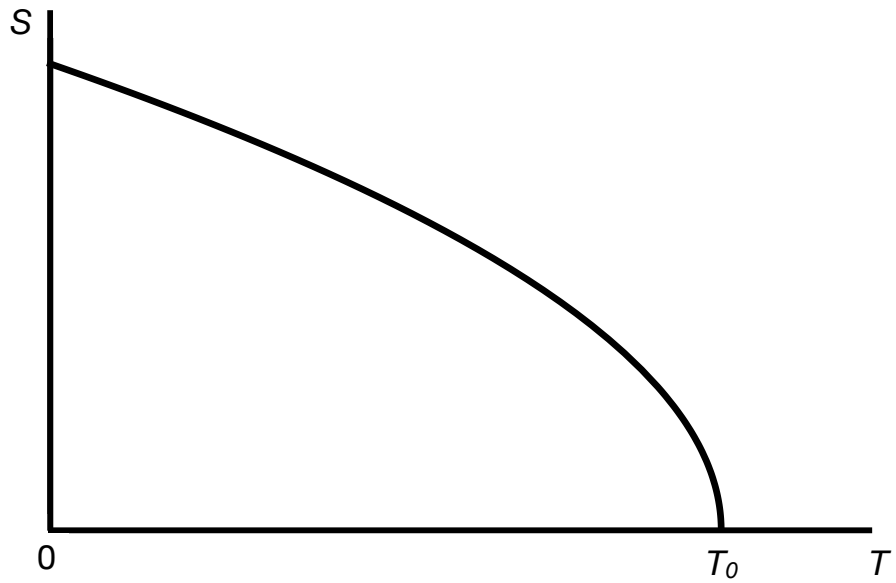

Figure 2.1: The order parameter S as a function of temperature for a second order phase transition.

The Landau free energy F_L as a function of the order parameter S at different temperatures is illustrated in Fig. 2.2. For $T > T_0$, the minimum value of F_L is observed at $S = 0$. When $T < T_0$, the equilibrium point shift to $|S| \neq 0$. As shown in Fig. 2.1, the magnitude of the order parameter changes continuously at T_0, which denotes a second order phase transition or continuous phase transition.

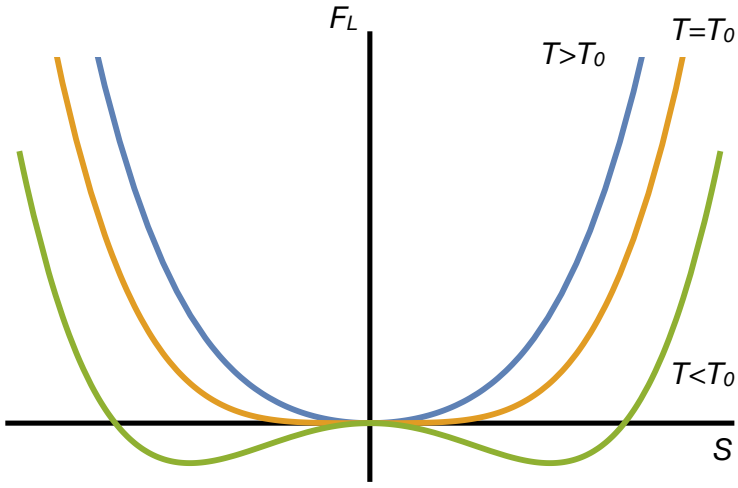

Figure 2.2: Landau free energy as a function of the order parameter S at various temperatures for a second order phase transition.

2.1.3 First order phase transition

For $B < 0$, the positive 6^{th} order term ($C > 0$) of Eq. 2.2 is needed to stabilize a minimum Landau free energy. Solving the equation

$$\frac{\partial F_L}{\partial S} = S(A + BS^2 + CS^4) = 0, \tag{2.9}$$

we obtain

$$S = \begin{cases} 0, \\ \sqrt{\frac{-B-\sqrt{B^2-4AC}}{2C}}, & T_0 \leq T \leq T_1, \\ \sqrt{\frac{-B+\sqrt{B^2-4AC}}{2C}}, & T \leq T_1, \end{cases} \tag{2.10}$$

where

$$T_1 = \frac{B^2}{4aC} + T_0, \quad A = a(T - T_0). \tag{2.11}$$

The curves of the Landau free energy (Eq. 2.4) as a function of the order parameter S at various temperatures are illustrated in Fig. 2.3. Decreasing the temperature (red arrows in Fig. 2.4) from $T > T_1$ down to $T = T_0$, the system remains in the disordered state associated with $S = 0$ due to the energy barrier, even if a local minimum (associated with a metastable state) exists. Then, the system transfers to the ordered state ($S \neq 0$) at $T = T_0$ with the disappearance of the energy barrier. In contrast, when the temperature increases from $T < T_0$, the system stays in the ordered state until the phase transition occurs at $T = T_1$ (blue arrows in Fig. 2.4). Therefore, in general, first order phase transition is identified by the observation of thermal hysteresis and a sudden change of the measured order parameter at the critical temperature.

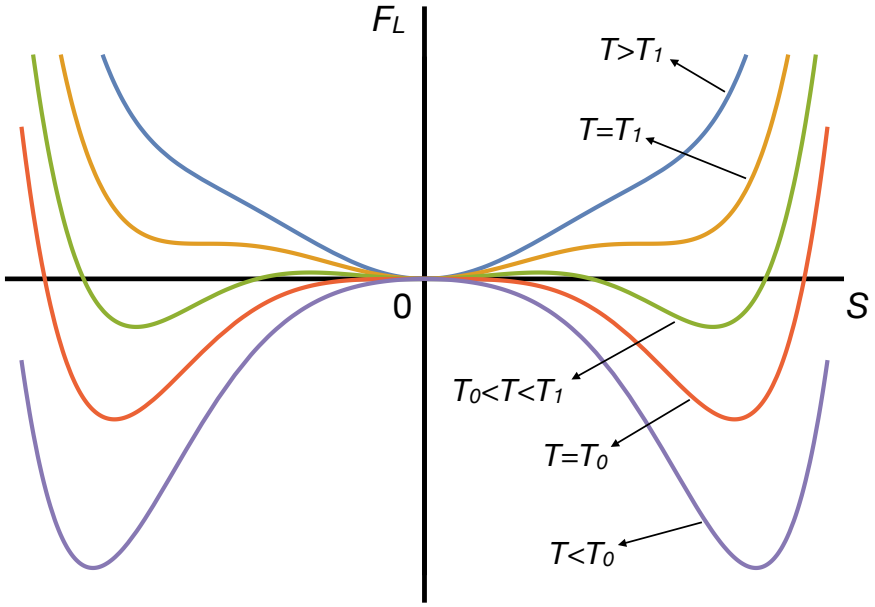

Figure 2.3: Landau free energy as a function of the order parameter S at various temperatures for a first order phase transition.

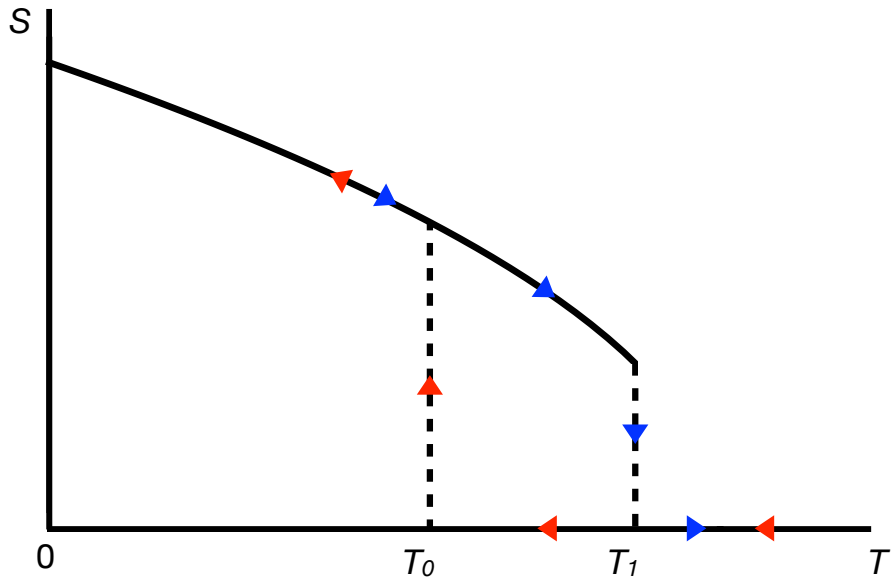

Figure 2.4: The order parameter S as a function of temperature for a first order phase transition.

2.2 Landau free energy of TLAF

The phenomenological Landau free energy can also be obtained from some microscopic details associated with a specific system, where the crystal symmetry is taken into account. This nonlocal free energy approach has been used with success to account for the magnetic phase diagrams of many magnetic systems by M. L. Plumer [82,83]. In this work we adopt the same approach by expanding the free energy of 2D TLAF in term of the spin density $\mathbf{s}(\mathbf{r})$ up to fourth order. In this case, the isotropic terms in the free energy are

$$\begin{aligned} F_s = & \frac{1}{2V}\int d\mathbf{r}\int d\mathbf{r}' J_{ij}(\tau)s_i(\mathbf{r})s_j(\mathbf{r}') \\ & + \frac{1}{4V}\int d\mathbf{r_1}\int d\mathbf{r_2}\int d\mathbf{r_3}\int d\mathbf{r_4} B_{ijkl}(\mathbf{r_1},\mathbf{r_2},\mathbf{r_3},\mathbf{r_4})s_i(\mathbf{r_1})s_j(\mathbf{r_2})s_k(\mathbf{r_3})s_l(\mathbf{r_4}) \\ & - \int d\mathbf{r}\ \mathbf{s}(\mathbf{r})\cdot\mathbf{H}, \end{aligned} \tag{2.12}$$

where V is the crystal volume, i,j,k,l correspond to the x,y,z coordinates, $\tau = \mathbf{r}-\mathbf{r}'$. Furthermore, we assume that the coefficients J_{ij} and B_{ijkl} depend only on differences between pairs of coordinates. While the inversion symmetry requires that $J(\tau) = J(-\tau)$. We consider that the local spin density $\mathbf{s}(\mathbf{r})$ is given by

$$\mathbf{s}(\mathbf{r}) = \frac{V}{N}\sum_{\mathbf{R}}\rho(\mathbf{r})\delta(\mathbf{r}-\mathbf{R}), \tag{2.13}$$

where $\rho(\mathbf{r})$ represents a spin density expressed in term of a single Fourier component $\mathbf{Q} = (1/3, 1/3)$ (determined from neutron scattering measurements [47]), so that

$$\rho(\mathbf{r}) = \mathbf{m} + \mathbf{S}e^{i\mathbf{Q}\cdot\mathbf{r}} + \mathbf{S}^* e^{-i\mathbf{Q}\cdot\mathbf{r}}, \tag{2.14}$$

where $\mathbf{R}$ is the positions of the magnetic ions, $\mathbf{m}$ is the uniform magnetization induced by the magnetic field, and $\mathbf{S}$ is the spin polarization vector. In this description, the total spin is decomposed into a ferromagnetic component represented by $\mathbf{m}$ and the antiferromagnetic configuration defined by $\mathbf{S}$. While the net magnetization $\mathbf{m}$ increases with the increment of $\mathbf{H}$, the sum over $\mathbf{S}_i$ remains equal to zero at all temperature and magnetic field.

After integration, the free energy F (as derived by M. L. Plumer [10, 82, 84]) can be written in term of isotropic terms F_I and an anisotropic contributions F_A (here higher power anisotropic terms are ignored), where

$$F = F_I + F_A, \tag{2.15}$$

$$\begin{aligned} F_I = {} & A_Q S^2 + \frac{1}{2} A_0 m^2 - \mathbf{m} \cdot \mathbf{H} \\ & + B_1 S^4 + \frac{1}{2} B_2 \left| \mathbf{S} \cdot \mathbf{S} \right|^2 + \frac{1}{4} B_3 m^4 + 2 B_4 \left| \mathbf{m} \cdot \mathbf{S} \right|^2 + B_5 m^2 S^2, \end{aligned} \tag{2.16}$$

and

$$F_A = -A_z \left| S_z \right|^2 - \frac{1}{2} A_{0z} m_z^2, \tag{2.17}$$

where A_Q and A_0 are both temperature dependent coefficients defined as

$$A_Q = a \left(T - T_Q \right) \quad \text{and} \quad A_0 = a \left(T - T_0 \right), \tag{2.18}$$

with $a > 0$, while T_Q and T_0 represent the Néel temperature and the Curie temperature, respectively. To allow for possible nonlinear spin configurations, the complex polarization vector $\mathbf{S}$ is written as

$$\mathbf{S} = \mathbf{S_1} + i\mathbf{S_2}, \tag{2.19}$$

with

$$\begin{aligned} \mathbf{S_1} &= -S\cos\beta\ (\sin\theta\hat{\rho}_1(\phi) + \cos\theta\hat{\mathbf{z}}), \\ \mathbf{S_2} &= -S\sin\beta\ \hat{\rho}_2(\phi), \end{aligned} \tag{2.20}$$

and

$$\begin{aligned} \hat{\rho}_1(\phi) &= \cos\phi\ \hat{\mathbf{x}} + \sin\phi\ \hat{\mathbf{y}}, \\ \hat{\rho}_2(\phi) &= -\sin\phi\ \hat{\mathbf{x}} + \cos\phi\ \hat{\mathbf{y}}, \end{aligned} \tag{2.21}$$

where $\hat{\mathbf{x}} \perp \hat{\mathbf{y}} \perp \hat{\mathbf{z}}$ are orthogonal unit vectors. Here, in order to possibly account for the spin polarization of the V phase, as observed in $Ba_3CoSb_2O_9$ [6, 9] and $RbFe(MoO_4)_2$ [45, 62], we modify $\mathbf{S_1}$ and $\mathbf{S_2}$ by adding the angle ϕ which was not considered by M. L. Plumer [10, 82, 84]. The values of β, θ and ϕ, which depict the possible configuration of spin polarization with $\mathbf{H} \parallel x$-axis and $\mathbf{H} \parallel z$-axis, are presented in Table 2.1. As shown in Fig 2.5, the three phases with $\mathbf{H} \parallel x$-axis, Y, uud and V, and the two phases with $\mathbf{H} \parallel z$-axis, U and V_z, are comprised of the uniform magnetization ($\mathbf{m}$) induced by the magnetic field and the spin polarization vector ($\mathbf{S}$). For $\mathbf{H} \parallel x$-axis, all spins orient in the basal plane due to the easy-plane anisotropy, which corresponds to $\theta = \frac{\pi}{2}$ for all states. Here β represents the configuration of the spin polarization, while ϕ indicates the orientation of the configuration relative to the field direction. For $\mathbf{H} \parallel z$-axis, the spin polarization $\mathbf{S}$ also orients in the basal plane, meanwhile ϕ can be any value due to the isotropy of the basal plane.

$\mathbf{H} \parallel x$-axis	120° ($\mathbf{H} = 0$)	Y	uud	V
β	$\pi/4$	$0 < \beta < \pi/4$	0	0
θ	$\pi/2$	$\pi/2$	$\pi/2$	$\pi/2$
ϕ	0	0	0	$\pi/2$

$\mathbf{H} \parallel z$-axis	120° ($\mathbf{H} = 0$)	U	V_z
β	$\pi/4$	$\pi/4$	0
θ	$\pi/2$	$\pi/2$	$\pi/2$

Table 2.1: The values of β, θ and ϕ for 120°, Y, uud and V states with $\mathbf{H} \parallel x$-axis, and for U and V_z states with $\mathbf{H} \parallel z$-axis.

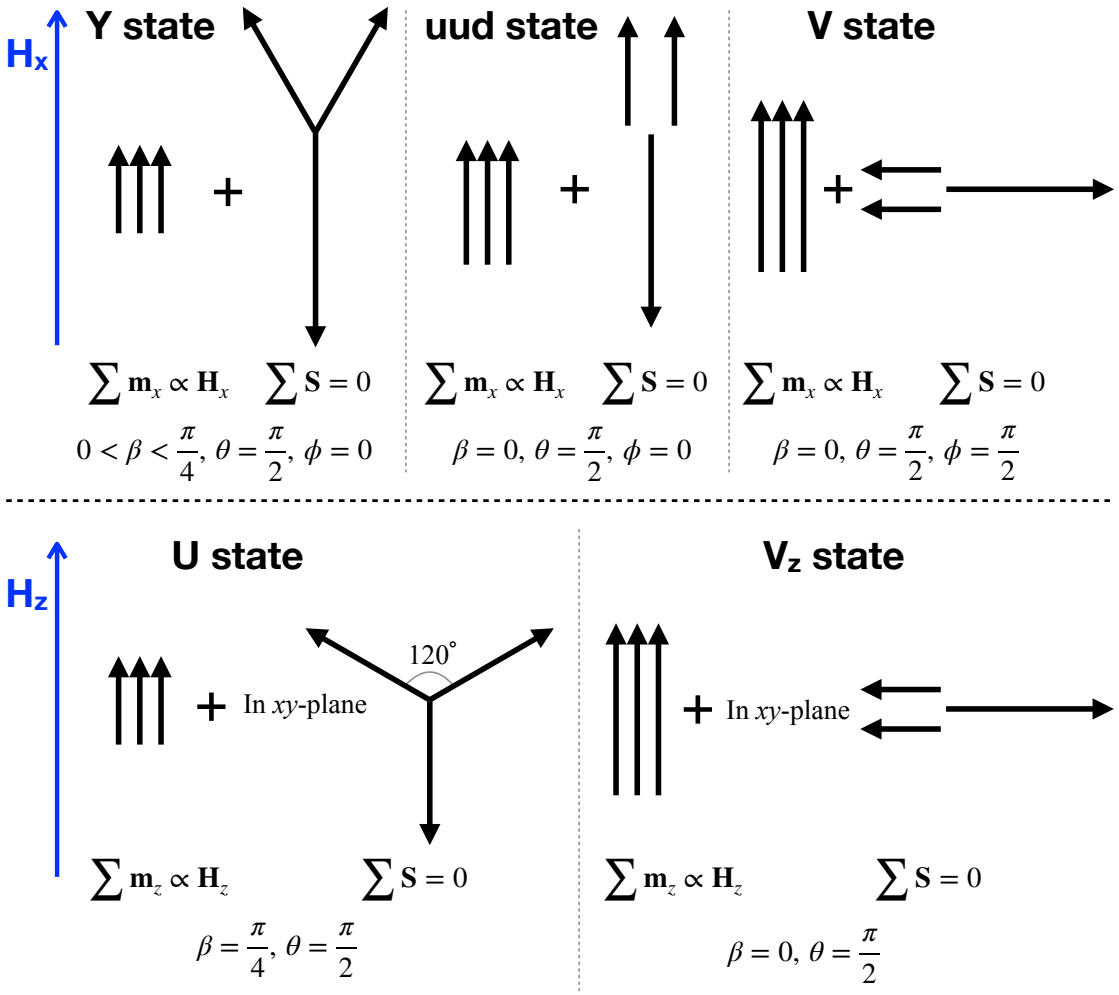

Figure 2.5: The ground states of the magnetization process of TLAF with $\mathbf{H} \parallel x$-axis and $\mathbf{H} \parallel z$-axis are illustrated using the uniform magnetization ($\mathbf{m}$) induced by the magnetic field and the spin polarization vector ($\mathbf{S}$). With the increment of the magnetic field, the magnetization increases, while $\mathbf{S}$ shrinks and changes the configuration.

2.3 Schematic H-T phase diagrams by the Landau model with 4^{th} order

The competition between several terms in the free energy determine the spin configurations in different phases. The free energy of a triangular based lattice has been already studied in detail by M. Plumer [10] and the role of each coefficient is well understood. Since $Ba_3CoSb_2O_9$ has an easy-plane anisotropy, we must impose $A_z < 0$ so that the term $-A_z |S_z|^2$ favours configurations with $\mathbf{S} \perp \hat{\mathbf{z}}$ at $\mathbf{H} = 0$, while the term $-\frac{1}{2}A_{0z}m_z^2$ can be omitted for convenience. Moreover, with $B_2 > 0$, the term $\frac{1}{2}B_2 |\mathbf{S} \cdot \mathbf{S}|^2$ is minimized for a helical polarization state. Furthermore, we must consider $B_4 < 0$, as $\mathbf{S} \parallel \mathbf{H}$ minimizes the term $2B_4 |\mathbf{m} \cdot \mathbf{S}|^2$ at high field value. Although from Ref. [10] it is known that the H_x-T phase diagram of $Ba_3CoSb_2O_9$ shown in Fig. 1.8 cannot be obtained using the 4^{th} order Landau model, we can still explore the values of the parameters in Eq. 2.15 which can assist to determine the coefficients of high order Landau model in Sec. 2.4. Theoretically, the spin density can account for the V phase (see Fig. 2.5), but we only obtain the 120°, Y, uud states minimizing numerically the free energy at T = 0. Therefore, we determine only the phase boundaries for P→uud and uud→Y in this section.

In the paramagnetic state, as $\mathbf{S}$ is zero, the Landau free energy reduces to

$$F_P = -H_x m_x + \frac{1}{2}A_0 m_x^2 + \frac{1}{4}B_3 m_x^4, \tag{2.22}$$

so that m_x can be obtained by minimizing F_P with respect to m_x. According to Eq. 2.22, we have

$$\frac{\partial F_P}{\partial m_x} = -H_x + A_0 m_x + B_3 m_x^3 = 0 \tag{2.23}$$

Solving for m_x, we obtain

$$\begin{aligned} m_x(P) = &- \frac{\left(\frac{2}{3}\right)^{1/3} A_0}{\left(9B_3^2 H_x + \sqrt{3}\sqrt{4A_0^3 B_3^3 + 27B_3^4 H_x^2}\right)^{1/3}} \\ &+ \frac{\left(9B_3^2 H_x + \sqrt{3}\sqrt{4A_0^3 B_3^3 + 27B_3^4 H_x^2}\right)^{1/3}}{2^{1/3}3^{2/3}B_3} \\ &= \frac{H_x}{A_0} + O[H_x]^2, \end{aligned} \tag{2.24}$$

for low field. Considering that $m_x = \chi H_x$ in the paramagnetic state, where χ is the magnetic susceptibility, we obtain that

$$\chi = \frac{1}{A_0} = \frac{1}{a(T - T_0)}, \tag{2.25}$$

for the Curie-Weiss susceptibility.

In the uud state, where $\beta = 0$, $\theta = \frac{\pi}{2}$, and $\phi = 0$, the Landau free energy can be written as

$$\begin{aligned} F_{uud} = &- H_x m_x + \frac{1}{2}A_0 m_x^2 + \frac{1}{4}B_3 m_x^4 + A_Q S^2 \\ &+ 2B_4 m_x^2 S^2 + B_5 m_x^2 S^2 + B_1 S^4 + \frac{1}{2}B_2 S^4. \end{aligned} \tag{2.26}$$

Thus, minimizing Eq. 2.26 relative to m_x and S, we obtain the equations

$$\begin{aligned} \frac{\partial F_{uud}}{\partial m_x} &= -H_x + A_0 m_x + B_3 m_x^3 + 4B_4 m_x S^2 + 2B_5 m_x S^2 = 0, \\ \frac{\partial F_{uud}}{2S\partial S} &= A_Q + 2B_4 m_x^2 + B_5 m_x^2 + 2B_1 S^2 + B_2 S^2 = 0. \end{aligned} \tag{2.27}$$

Solving Eqs. 2.27 with the condition that $|S| = 0$ at the paramagnetic (P)→uud phase boundary, we obtain the condition

$$H_x(uud \to P) = A_0 m_x + B_3 m_x^3, \tag{2.28}$$

where

$$m_x = \sqrt{-\frac{A_Q}{2B_4 + B_5}}. \tag{2.29}$$

In the Y state, considering $0 < \beta < \frac{\pi}{4}$, $\theta = \frac{\pi}{2}$, and $\phi = 0$, the Landau free energy is

$$\begin{aligned} F_Y = &- H_x m_x + \frac{1}{2}A_0 m_x^2 + \frac{1}{4}B_3 m_x^4 + A_Q S^2 \sin^2\beta + B_5 m_x^2 S^2 \sin^2\beta \\ &+ B_1 S^4 \sin^4\beta + \frac{1}{2}B_2 S^4 \sin^4\beta + A_Q S^2 \cos^2\beta + 2B_4 m_x^2 S^2 \cos^2\beta \\ &+ B_5 m_x^2 S^2 \cos^2\beta + 2B_1 S^4 \sin^2\beta \cos^2\beta - B_2 S^4 \sin^2\beta \cos^2\beta \\ &+ B_1 S^4 \cos^2\beta^2 + \frac{1}{2}B_2 S^4 \cos^2\beta^2 \end{aligned} \tag{2.30}$$

Minimizing Eq. 2.30 relative to S, m_x and β, we have that

$$\begin{aligned} \frac{\partial F_Y}{2S\partial S} &= A_Q + 2B_4 m_x^2 + B_5 m_x^2 + 2B_1 S^2 + B_2 S^2 \\ &\quad - 2B_4 m_x^2 \sin^2\beta - 4B_2 S^2 \sin^2\beta + 4B_2 S^2 \sin^4\beta = 0, \\ \frac{\partial F_Y}{\partial m_x} &= -H_x + A_0 m_x + B_3 m_x^3 + 2B_5 m_x S^2 + 4B_4 m_x S^2 \cos^2\beta = 0, \\ \frac{1}{4S^2 \cos\beta \sin\beta}\frac{\partial F_Y}{\partial \beta} &= -B_4 m_x^2 - B_2 S^2 + 2B_2 S^2 \sin^2\beta = 0. \end{aligned} \tag{2.31}$$

Solving Eqs. 2.31 with the condition that $\beta = 0$ at the Y→uud phase boundary, we obtain the analytical solution

$$H_x(Y \to uud) = A_0 m_x + \frac{B_2 B_3 - 4B_4^2 - 2B_4 B_5}{B_2} m_x^3, \tag{2.32}$$

where

$$m_x = \sqrt{\frac{A_Q B_2}{2B_1 B_4 - B_2 B_4 - B_2 B_5}}. \tag{2.33}$$

For $\mathbf{H} \parallel z$-axis, the U state is obtained at low field, where $\beta = \frac{\pi}{4}$, $\theta = \frac{\pi}{2}$ and $\phi = 0$. Therefore, the landau free energy is

$$F_U = -H_z m_z + \frac{1}{2} A_0 m_z^2 + \frac{1}{4} B_3 m_z^4 + A_Q S^2 + B_5 m_z^2 S^2 + B_1 S^4. \tag{2.34}$$

Using the same method, we obtain that

$$\begin{aligned} \frac{\partial F_u}{\partial m_z} =& - H_z + A_0 m_z + B_3 m_z^3 + 2 B_5 m_z S^2 = 0, \\ \frac{\partial F_u}{\partial S} =& A_Q + B_5 m_z^2 + 2 B_1 S^2 = 0. \end{aligned} \tag{2.35}$$

Solving Eqs. 2.35 with the condition that $S = 0$, we obtain the analytical solution of the boundary between U and paramagnetic states

$$H_z(U \to P) = A_0 m_z + B_3 m_z^3, \tag{2.36}$$

where

$$m_z = \sqrt{-\frac{A_Q}{B_5}}. \tag{2.37}$$

In order to determine all parameters (given in Table 2.3) in the Landau free energy Eq. 2.15, we solve the equations Eq. 2.18, Eq. 2.25, Eq. 2.28, Eq. 2.32 and Eq. 2.36 with data (listed in Table 2.2) obtained and estimated from experiments. The corresponding H_x-T and H_z-T phase diagrams are shown in Fig. 2.6, which are consistent with Ref. [10]. The second order phase transitions confirmed in experiments [9, 65], the Y→uud and paramagnetic (P)→uud with $\mathbf{H} \parallel x$-axis, the P→U with $\mathbf{H} \parallel z$-axis, are obtained. Moreover, the H_x-T phase diagram of the quasi 1D frustrated TLAF $CsMnBr_3$, which has the same space group as $Ba_3CoSb_2O_9$ ($P6_3/mmc$) [85] and easy-plane anisotropy [86], has been successfully reproduced by M. L. Plumer

et al. [87] using the 4^{th} order Landau free energy Eq. 2.15. However, in the case of $CsMnBr_3$ [88] the coefficient B_4 is positive, reproducing the elliptical and linear states with $\mathbf{S} \perp \mathbf{m}$ [87], while for $Ba_3CoSb_2O_9$ the two ordered states have $\mathbf{S} \parallel \mathbf{m}$ instead. Therefore, in order to reproduce the V state with $\mathbf{H} \parallel x$-axis and the V_z state with $\mathbf{H} \parallel z$-axis, 6^{th} order terms of Landau free energy, which favor $\mathbf{S} \perp \mathbf{m}$ at high field, are needed.

χ(10K, 0.5T)	1.72×10^{-3} [65]
$T_Q(H = 0)$	3.8 K [9]
T_0	-70 K
$H_x(Y \to uud)(T = 0)$	10 T [9]
$H_x(uud \to P)(T = 0)$	32 T
$H_z(U \to P)(T = 0)$	40 T

Table 2.2: The data obtained and estimated from experiments.

a	A_z	B_1	B_2	B_3	B_4	B_5
0.2	-0.1	0.81	0.66	1.63	-0.5	1.3

Table 2.3: Values of the parameters in the 4^{th} order Landau free energy Eq. 2.15.

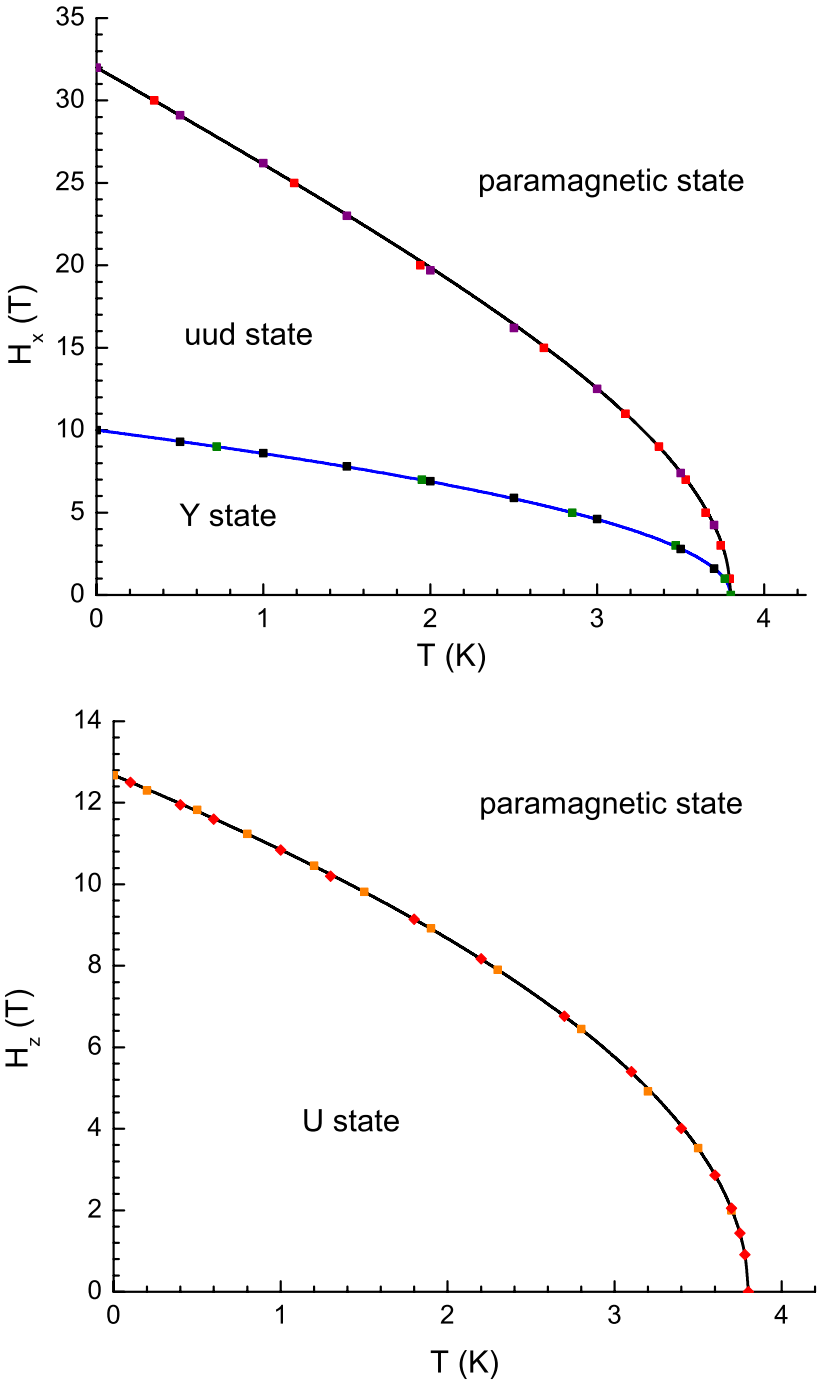

Figure 2.6: H_x-T and H_z-T phase diagrams by the Landau model with 4^{th} order. The solid curves represent the analytical solutions. The discrete points denote the numerical results. Also see Ref. [10].

2.4 Schematic H-T phase diagrams by the Landau model with 6^{th} order

In the experimental H-T phase diagrams of $Ba_3CoSb_2O_9$, shown in Fig. 1.8, there are several features which cannot be obtained using 4^{th} order Landau model. For $\mathbf{H} \parallel a$-axis, there are two multicritical points, (3.9 K, 5 T) at low field and (3.9 K, 17 T) at high field [9]. Meanwhile, the paramagnetic state transfers to the Y state at low fields. Moreover, T_Q increases with the increment of the applied field with medium values in the uud state. At last, the V state exists at high fields. For $\mathbf{H} \parallel c$-axis, the multicritical point and the V_z state are not reproduced. In an attempt to account for these features, we take into consideration 6^{th} order terms in the Landau free energy. The total Landau free energy, with higher-order anisotropy omitted, is then given as

$$\begin{aligned} F = & A_Q S^2 + \frac{1}{2} A_0 m^2 - A_z \left|S_z\right|^2 - \mathbf{m} \cdot \mathbf{H} \\ & + B_1 S^4 + \frac{1}{2} B_2 \left|\mathbf{S} \cdot \mathbf{S}\right|^2 + \frac{1}{4} B_3 m^4 + 2 B_4 \left|\mathbf{m} \cdot \mathbf{S}\right|^2 + B_5 m^2 S^2 \\ & + D_1 m^4 S^2 + D_2 S^6 \\ & + D_3 \left|\mathbf{m} \cdot \mathbf{S}\right|^2 m^2 + D_4 \left|\mathbf{S} \cdot \mathbf{S}\right|^2 S^2 \\ & + D_5 \left|\mathbf{m} \cdot \mathbf{S}\right|^2 S^2 + D_6 \left|\mathbf{S} \cdot \mathbf{S}\right|^2 m^2 + D_7 m^2 S^4 \\ & + D_8 m^6 + D_9 \left[(\mathbf{S} \cdot \mathbf{S})^3 + (\mathbf{S}^* \cdot \mathbf{S}^*)^3\right] \\ & + D_{10} \left[(\mathbf{m} \cdot \mathbf{S}^*)^2 (\mathbf{S} \cdot \mathbf{S}) + (\mathbf{m} \cdot \mathbf{S})^2 (\mathbf{S}^* \cdot \mathbf{S}^*)\right]. \end{aligned} \tag{2.38}$$

In this work, we ignore the last three 6^{th} order terms setting D_8, D_9, D_{10} equal to zero, since the other seven 6^{th} order terms are sufficient to determine the features missed using the 4^{th} order Landau model. As the V and V_z states at high fields correspond to configurations with $\mathbf{S} \perp \mathbf{m}$ (see Fig. 2.5), D_3 and D_5 are set to be positive in order to favor these two states. Moreover, we must consider $D_4 < 0$ and $D_6 < 0$ due to the

collinear configuration of the spin polarization ($\mathbf{S}$) in the V and V_z states.

The numerical minimization of Eq. 2.38 using Mathematica is applied to determine the states and the phase boundaries with the data estimated and obtained from experimental results listed in Table 2.4. The values of all coefficients are presented in Table 2.5.

χ(10K, 0.5T)	1.72×10^{-3} [65]
$T_Q(H = 0)$	3.8 K [9]
T_0	-70 K
(T_{M1}, H_{M1})	(4 K, 4 T)
(T_{M2}, H_{M2})	(4 K, 20 T)
T_Q(Max)	5 T [9]
$H_x(Y \rightarrow uud)(T = 0)$	10 T [9]

Table 2.4: The data obtained and estimated from experiments.

	a	A_z	B_1	B_2	B_3	B_4	B_5
4^{th}	0.2	-0.1	0.81	0.66	1.63	-0.5	1.3
6^{th}	0.2	-0.1	-0.55	0.3	3.4	-0.15	-0.54
6^{th}	D_1	D_2	D_3	D_4	D_5	D_6	D_7
	0.62	5.8	0.3	-0.2	0.5	-0.18	2.6

Table 2.5: Values of the parameters in the 6^{th} order Landau free energy Eq. 2.38 comparing with the values in Table 2.3 for the 4^{th} order Landau free energy Eq. 2.15.

2.4.1 H $\parallel$ x-axis

The H_x-T phase diagram, which mimics relatively well the experimental results (see Fig. 1.8), is shown in Fig. 2.7. In comparison to the 4^{th} order Landau free energy, B_1 and B_5 are negative when using the 6^{th} order Landau free energy (see Table 2.5). In order to obtain the multicritical point (T_{M1}, H_{M1}) (see Fig. 1.8), we find that $B_1 < 0$ lifts the degeneracy between the Y and uud phase at $H = 0$ as obtained with the 4^{th} order free energy. Meanwhile, $D_2 > 0$ for S^6 is needed for a stable system as the value of B_1 is negative (see Subsection 2.1.3). Moreover, $B_5 < 0$ accounts for the increment of T_Q at the paramagnetic (P)$\rightarrow$uud phase boundary, which is also observed in the case of $CsNiCl_3$ [83]. While we need m^4S^2 with $D_1 > 0$ to determine the other section of the P$\rightarrow$uud phase boundary. Furthermore, the V state and the multicritical point (T_{M2}, H_{M2}) at high field are other important features which cannot be obtained using the 4^{th} order Landau free energy. In order to reproduce the V state, $|\mathbf{m} \cdot \mathbf{S}|^2 m^2$ with $D_3 > 0$ is taken into consideration, which competes with $|\mathbf{m} \cdot \mathbf{S}|^2$ ($B_4 < 0$) corresponding to $\mathbf{S} \parallel \mathbf{m_x}$. At high fields, $|\mathbf{m} \cdot \mathbf{S}|^2 m^2$ is dominant and accounts for $\mathbf{S} \perp \mathbf{m_x}$ in the V state (see Fig. 2.5). Meanwhile, $|\mathbf{m} \cdot \mathbf{S}|^2 S^2$ with $D_5 > 0$ also corresponds to $\mathbf{S} \perp \mathbf{m_x}$ in the V state, which is important at medium fields. Due to the increment of S with the decrease of temperature (see Figs. 2.9 and 2.10), these two terms expand the range of the V state and reduce the range of the uud state, starting from the multicritical point (T_{M2}, H_{M2}). At last, $|\mathbf{S} \cdot \mathbf{S}|^2 S^2$ with $D_4 < 0$ and $|\mathbf{S} \cdot \mathbf{S}|^2 m^2$ with $D_6 < 0$ are needed for the collinear configuration of spin polarization in the V state as shown in Fig. 2.5, which compete with $|\mathbf{S} \cdot \mathbf{S}|^2$ with $B_2 > 0$ corresponding to the elliptical configuration of spin polarization.

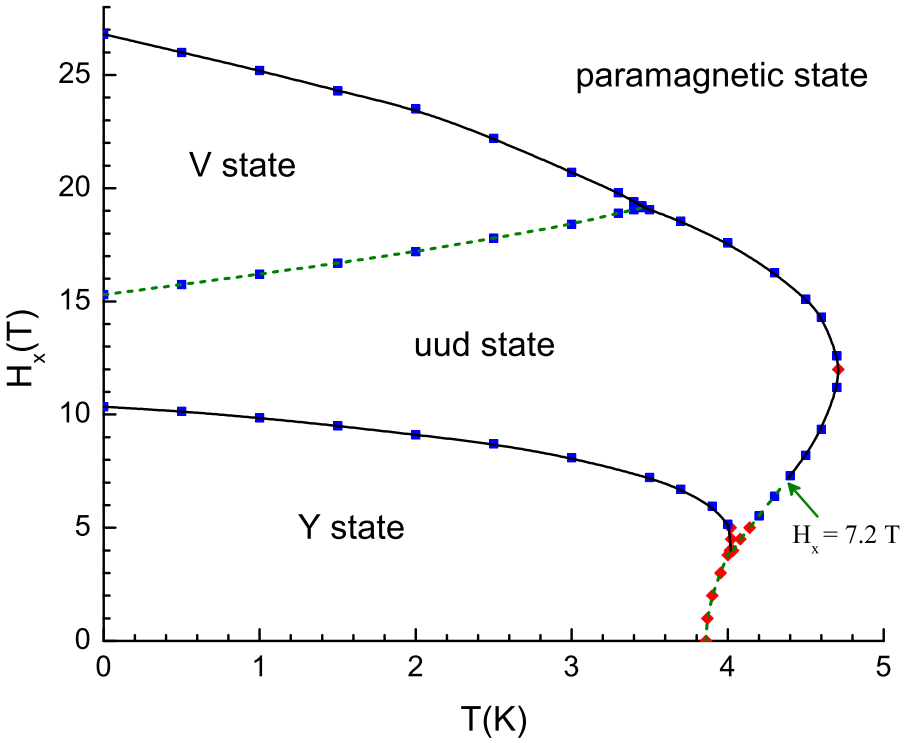

Figure 2.7: H_x-T phase diagram by the Landau model with 6^{th} order. The discrete points denote the numerical results of the Landau free energy Eq. 2.38. The dashed and solid curves are guides for the eye, which represent the first and second order phase transitions, respectively.

Although all phases are successfully reproduced using the 6^{th} order Landau free energy, this numerical phase diagram shows some features different from that of the experimental results [9,47,64,65]. The discontinuous variation of the spin polarization (S) and ϕ as a function of the magnetic field (H_x) (see the example at $T = 0$ shown in Fig. 2.8), obtained by numerical minimization of the free energy using Mathematica, indicates that the uud→V phase transition is predicted to be first order. Moreover, the paramagnetic (P)→Y phase transition is also predicted to be first order as shown by the discontinuous dependence of the spin polarization (S) and the uniform magnetization (m_x) as a function of temperature (T) (see the example with $H_x = 2$ T shown in Fig. 2.9). Meanwhile, the numerical results demonstrate that the P→uud phase transition with $H_x < 7.2$ T (the dashed lines in Fig. 2.7) is also first order (see Fig. 2.10). Referring to Subsection 2.1.3, it is known that the property of the phase transitions between the paramagnetic state and the ordered states are accounted for by the sign of the summation of all S^4 power terms in Eq. 2.38 (one 4^{th} order term and three 6^{th} order terms). Although the two 6^{th} order terms, $|\mathbf{m} \cdot \mathbf{S}|^2 S^2$ with $D_5 > 0$ and $m^2 S^4$ with $D_7 > 0$, determine the positive summation with large value of m_x at $H_x > 7.2$ T, the 4^{th} order term, S^4 with $B_1 < 0$, is dominant at low fields. As a result, the P→Y and P→uud ($H_x < 7.2$ T) phase transitions are first order. Considering that the transition between the paramagnetic and Umbrella (120°) states of $CsNiCl_3$ is confirmed to be first order by the observation of a small hysteresis [89], we could also assume that the P→Y and P→uud ($H_x < 7.2$ T) phase transitions in $Ba_3CoSb_2O_9$ are weakly first order, although no experimental evidence is provided until now. Due to the 1/2 spin of $Ba_3CoSb_2O_9$, it is possible that strong spin fluctuations, which have effects on the spin ordering [2,65,67,68] (magnetization plateau) and magnetoelastic coupling [3], decrease the hysteresis to a size which cannot be observed, even using the high-resolution ultrasonic measurement [9]. Moreover, the negative biquadratic

exchange coupling ($\gamma < 0$) in the Heisenberg model (see Section 3.1) could correspond to $B_1 < 0$, accounting for the first order P→Y phase transition. Therefore, further work using Monte Carlo simulation with the biquadratic exchange coupling ($\gamma < 0$) are needed in order to confirm the properties of these phase transitions.

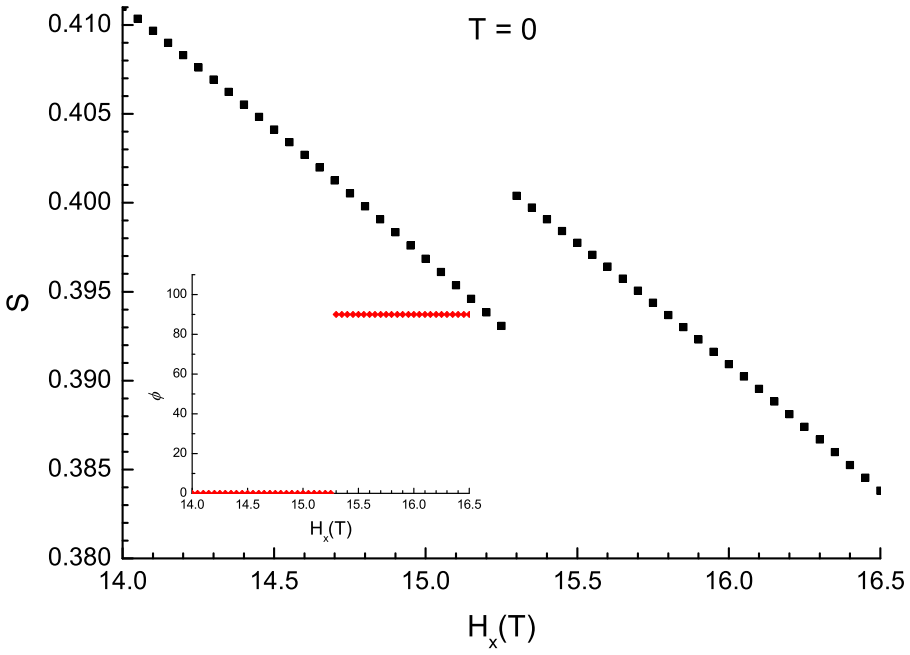

Figure 2.8: The numerical results of the spin polarization and ϕ (inserted figure) as a function of field with $T = 0$ using the Landau model with 6^{th} order.

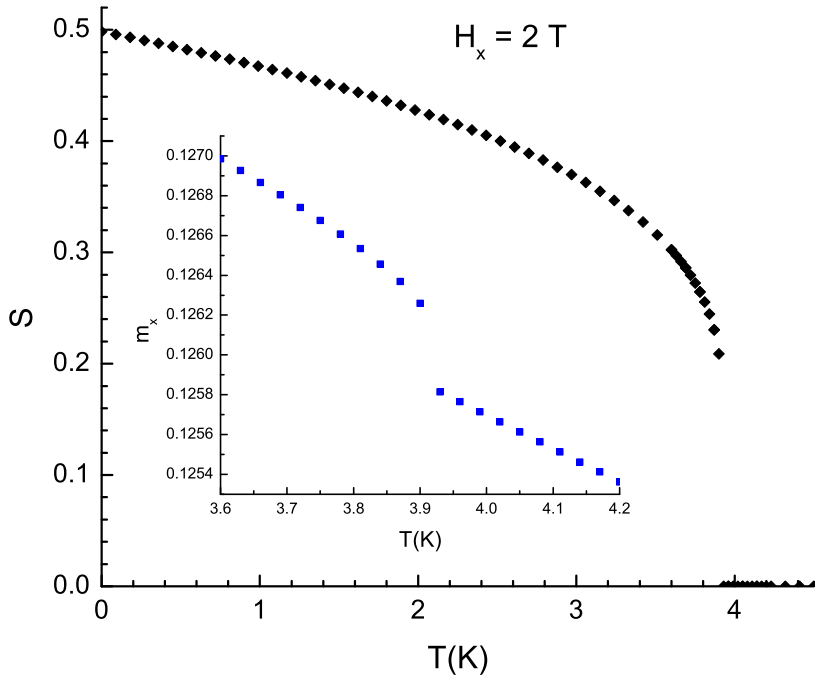

Figure 2.9: The numerical results of the spin polarization and the uniform magnetization (inserted figure) as a function of temperature with $H_x = 2$ T using the Landau model with 6^{th} order.

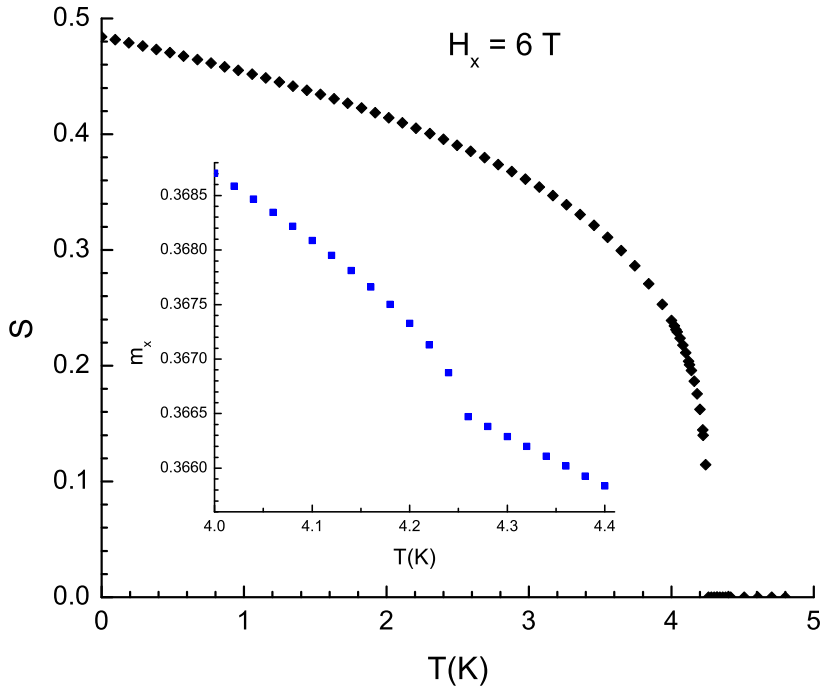

Figure 2.10: The numerical results of the spin polarization and the uniform magnetization (inserted figure) as a function of temperature with $H_x = 6$ T using the Landau model with 6^{th} order.

2.4.2 H $\parallel$ z-axis

For **H** $\parallel$ z-axis, the magnetic phase diagram is shown in Fig. 2.11, which is obtained by numerical minimization of the free energy using Mathematica. Note that all coefficients in Eq. 2.38 have been fixed using for the H_x-T phase diagram Fig. 2.7, therefore calculating the H_z-T phase diagram represents a good test for the significance of the proposed Landau model. The model does account for the first order phase transition, U$\rightarrow$V$_z$ (see the example at $T = 0$ shown in Fig. 2.12), and the second order phase transitions, P$\rightarrow$U ($H_z > 7.7$ T) and P$\rightarrow$V$_z$, consistent with the experimental results [9, 65]. However, due to the negative summation of the S^4 power terms in Eq. 2.38, the P$\rightarrow$U ($H_z < 7.7$ T) phase transition is of the first order, which is confirmed by the discontinuous variation of the spin polarization (S) and the uniform magnetization (m_z) as a function of the temperature (T) (see the example at $H_z = 6$ T shown in Fig. 2.13), in contrast to experimental results [9, 65].

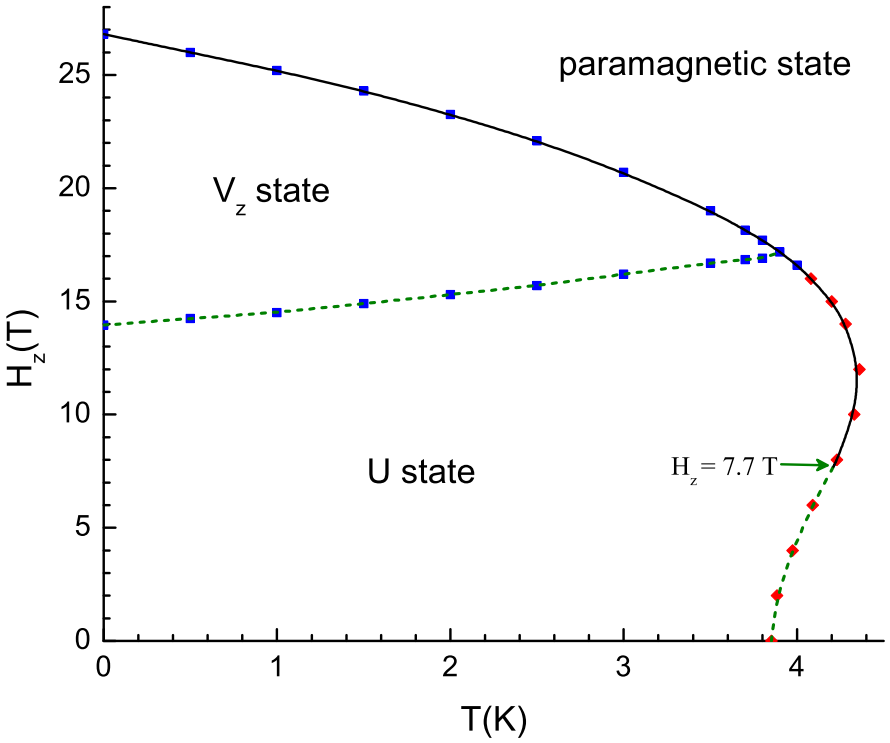

Figure 2.11: H_z-T phase diagram by the Landau model with 6^{th} order. The discrete points denote the numerical results of the Landau free energy Eq. 2.38. The dashed and solid curves are guides for the eye, which represent the first and second order phase transitions, respectively.

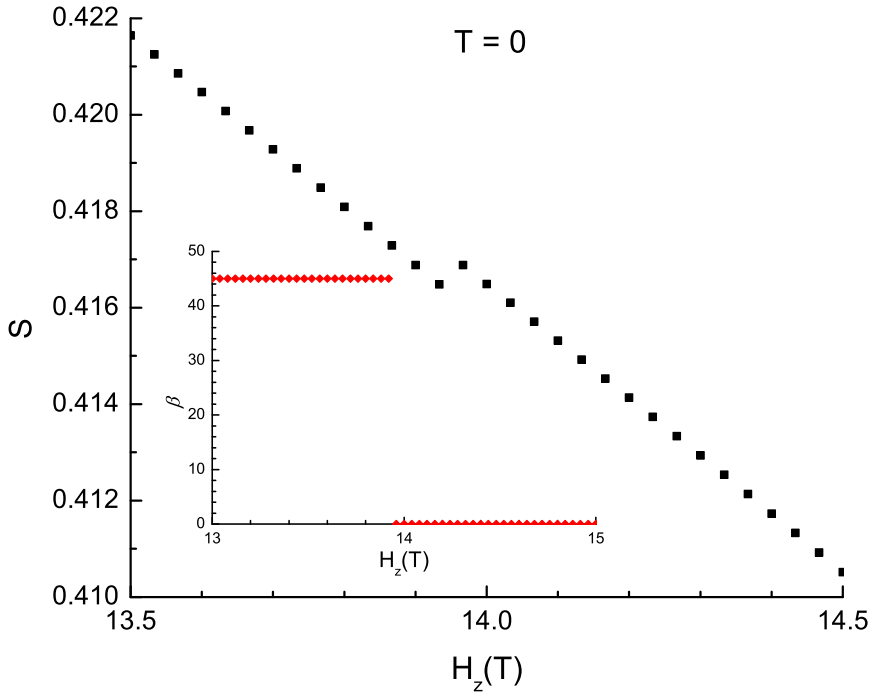

Figure 2.12: The numerical results of the spin polarization and β (inserted figure) as a function of field with $T = 0$ using the Landau model with 6^{th} order.

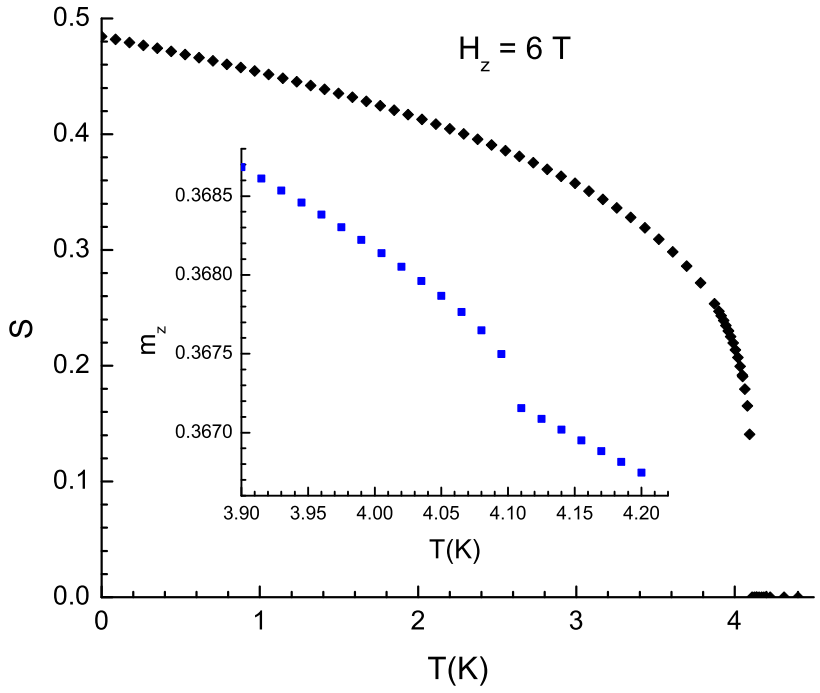

Figure 2.13: The numerical results of the spin polarization and the uniform magnetization (inserted figure) as a function of temperature with $H_z = 6$ T using the Landau model with 6^{th} order.

Chapter 3

Effects of interlayer exchange coupling on the layered triangular lattice antiferromagnets with bi-quadratic coupling

The two-dimensional (2D) geometrically frustrated triangular lattice antiferromagnets (TLAFs) are well known to display various exotic magnetic states due to the extensive degeneracy associated with magnetic frustration on a triangular lattice [4, 14, 19]. In particular, one of these exotic states, associated with a collinear up-up-down (uud) state, leads to the observation of a magnetization plateau in many quasi-2D TLAFs with easy-plane anisotropy at a value of 1/3 of the magnetization saturation (M_s) [6,9,41–43,45,57,62,65,66,90,91]. This plateau in the magnetization is believed to be stabilized by thermal/quantum spin fluctuations [2,5,8,92–94]. This conclusion is well supported by 2D quantum numerical studies [2,8,92–94] and Monte Carlo simulations

[5, 95] which successfully reproduce the observed phase sequence (120° state at zero field, Y state at low field, uud state at intermediate field, and V state at high field) for a magnetic field applied in the basal plane. Moreover, taken the hexagonal symmetry of 2D TLAF into account, the H-T phase diagrams with the ordered states discovered in experiments are obtained as shown in Chapter 2. However, a new phase between the uud state and the V state was proposed by D. Yamamoto *et al.* [11, 74] who took into consideration the interlayer exchange coupling. This finding could account for the magnetization anomaly observed near 3/5 M_s in $Ba_3CoSb_2O_9$ with $\mathbf{H} \parallel ab$-plane [6, 80], and it indicates the importance of the interlayer interaction, even when it is weak compared to the intralayer interaction. So far, the effect of the interlayer interaction in TLAFs has been limited to a few studies [11, 74], hence there is still a need to explore how the magnetic properties evolve as a function of the interlayer exchange coupling.

In this chapter, the effect of the antiferromagnetic interlayer interaction on the ground states of the layered easy-plane TLAFs is explored using a 3D classical Heisenberg model with bi-quadratic exchange coupling between nearest-neighbour ions within the basal plane. The bi-quadratic coupling plays an important role as it mimics the effect of spin fluctuations [2, 79] which are known to stabilize the magnetization plateau (uud state). On the other hand, the microscopic origin of the biquadratic exchange coupling term can also be associated with the spin-lattice coupling (magnetoelastic coupling) [69–73]. The effects due to the magnetoelastic coupling is studied in Chapter 6 and Chapter 7.

3.1 Model: Two-layer triangular lattice

Considering that thermal fluctuations generally favor collinear states [5, 75], it has been proposed and shown that quantum fluctuations can be the mechanism lifting the classical degeneracy in favor of the uud state at T = 0 K [74, 75, 77]. This is also supported by real-space perturbation theory [2,79] which shows that the effects of spin fluctuations in TLAFs can be taken into account by considering a classical model with a biquadratic exchange coupling term between nearest neighboring magnetic ions. The bi-quadratic coupling plays an important role as it mimics the effect of spin fluctuations [2, 96] which are known to stabilize the magnetization plateau (uud state). Considering first only one layer (see Fig. 3.1), the isotropic Hamiltonian of 2D Heisenberg model of the equilateral triangular lattice, with biquadratic exchange coupling, can then be expressed as

$$E = J \sum_{i \neq j} \mathbf{S}_i \cdot \mathbf{S}_j + \gamma \sum_{i \neq j} (\mathbf{S}_i \cdot \mathbf{S}_j)^2 - \frac{1}{3} \mathbf{H} \cdot \sum_i \mathbf{S}_i, \tag{3.1}$$

where the first term corresponds to the exchange coupling energy (J), the second term is the biquadratic exchange coupling energy (γ), the third term is Zeeman energy. Here the biquadratic coupling γ must be negative in order to account for the collinear spin configuration (uud state) [2].

The two-layer equilateral triangular lattice system is shown in Fig. 3.1, where each magnetic layer is comprised of three sublattices with spins at triangle vertices. As demonstrated previously [76, 97], note that six spins are sufficient to capture ground state spin configurations in the present model with NN exchange only. In the present model, Eq. 3.2 represents the energy per plane where only the intralayer exchange coupling constant (J) between the nearest neighbouring spins is taken into consideration.

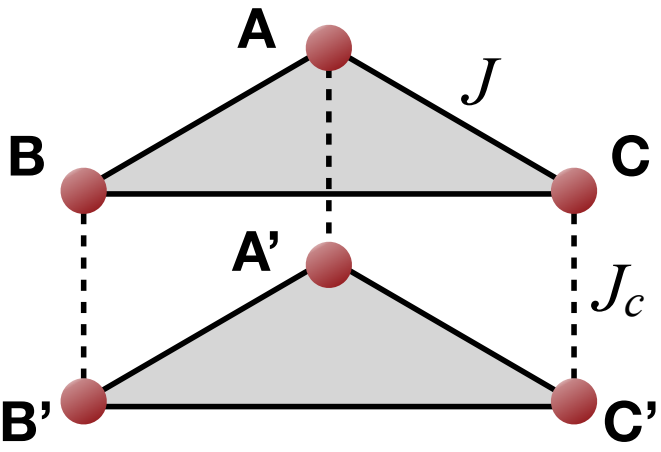

Figure 3.1: Two-layer triangular lattice with intralayer interaction J and interlayer interaction J_c. Reprinted with permission from [M Li, M L Plumer, and G Quirion, Journal of Physics: Condensed Matter, 32(13):135803, 2020]. Copyright (2020) by Institute of Physics.

The Heisenberg Hamiltonian per layer can be written as

$$E_\alpha = J \sum_{i \neq j} \mathbf{S}_{i\alpha} \cdot \mathbf{S}_{j\alpha} + \gamma \sum_{i \neq j} (\mathbf{S}_{i\alpha} \cdot \mathbf{S}_{j\alpha})^2 + D \sum_i {S_{i\alpha}}_z^2 - \frac{1}{3}\mathbf{H} \cdot \sum_i \mathbf{S}_{i\alpha}, \tag{3.2}$$

where E_α denotes the energy of layer α (stacked along the c-axis), i denotes one of the three magnetic ions at a triangle vertex. Here the single ion anisotropy energy (D) is also included in order to explore the magnetization of real systems for the magnetic field applied in and perpendicular to the basal plane. Furthermore, taking into consideration the interlayer nearest neighbouring exchange coupling (J_c), two layers are sufficient in order to obtain the ground states of 3D materials [11]. Thus, the total Hamiltonian for two layers (6 spins) can be written as

$$E = \frac{1}{2} \sum_\alpha E_\alpha + J_c \sum_{\alpha \neq \beta} \sum_i \mathbf{S}_{i\alpha} \cdot \mathbf{S}_{i\beta}, \tag{3.3}$$

where the second term is the sum over the interlayer nearest neighbouring spins. We omit the interlayer bi-quadratic coupling, since it is expected to be much smaller than the in-plane bi-quadratic coupling γ. Moreover, the interlayer bi-quadratic coupling is not expected to significantly affect the results due to the absence of frustration between two layers [98]. Here, the magnetization per site is thus given by

$$\mathbf{m} = \frac{1}{6} \sum_{\alpha} \sum_{i} \mathbf{S}_{i\alpha}, \tag{3.4}$$

with the spins written as 3D vectors described by the angles $\phi_{i\alpha}$ and $\theta_{i\alpha}$:

$$\mathbf{S}_{i\alpha} = (\cos\phi_{i\alpha} \sin\theta_{i\alpha}, \sin\phi_{i\alpha} \sin\theta_{i\alpha}, \cos\theta_{i\alpha}) \,. \tag{3.5}$$

In this work, the coefficient of the antiferromagnetic intralayer exchange coupling is set to $J = 1$, while the effect of the antiferromagnetic interlayer coupling ($0 < J_c < 0.24$) is explored. γ is set to -0.05 in order to stabilize uud state [2] and obtain a magnetization plateau width consistent with some experimental results [6, 9]. Since the single ion anisotropy and the exchange anisotropy have the same effect in the case of easy-plane anisotropy with the field in the plane [96], we set $D = 0.05$ close to the experimental value of the exchange anisotropy as determined for $Ba_3CoSb_2O_9$ [6].

3.2 Results without interlayer interaction

In this chapter, the magnetization and the spin configurations are first explored for different parameter and field values minimizing the Hamiltonian (Eq. 3.3) relative to $\phi_{i\alpha}$ and $\theta_{i\alpha}$ using Nelder-Mead method [99]. Without the interlayer interaction, the model describes a 2D TLAF. With the easy-plane anisotropy ($D = 0.05$), the

magnetization processes and spin configurations for the magnetic field applied parallel and perpendicular to the basal plane have been obtained as follows.

3.2.1 $\mathbf{H} \parallel ab$-plane: $J_c = 0$

The magnetization as a function of H_x which exhibits a magnetization plateau at 1/3 magnetization saturation is shown in Fig. 3.2. The width of the magnetization plateau is consistent with experimental results [6,65]. With an increasing magnetic field $\mathbf{H} \parallel x$-axis, the field dependence of the angles ϕ_i and the spin configurations are shown in Fig. 3.3 and Fig. 3.4, respectively. For $\mathbf{H} = 0$, the ground state corresponds to the 120° spin structure. At low field, a so-called Y state corresponds to a configuration where two moments are at some angle relative to the field while the other is opposed to the field direction. At intermediate field values, the magnetization plateau is associated with the up-up-down (uud) state where two spins are parallel to magnetic field while the third one is antiparallel. Finally, at high field values, the V state has two parallel spins with an angle less than 180° with respect to the third spin. The results presented in Fig. 3.2 and Fig. 3.4, obtained using the classical 2D effective Hamiltonian (Eq. 3.2) are in good agreement with previous results based on 2D Monte Carlo simulations [5] and 2D quantum models [2, 8, 11, 74, 92–94].

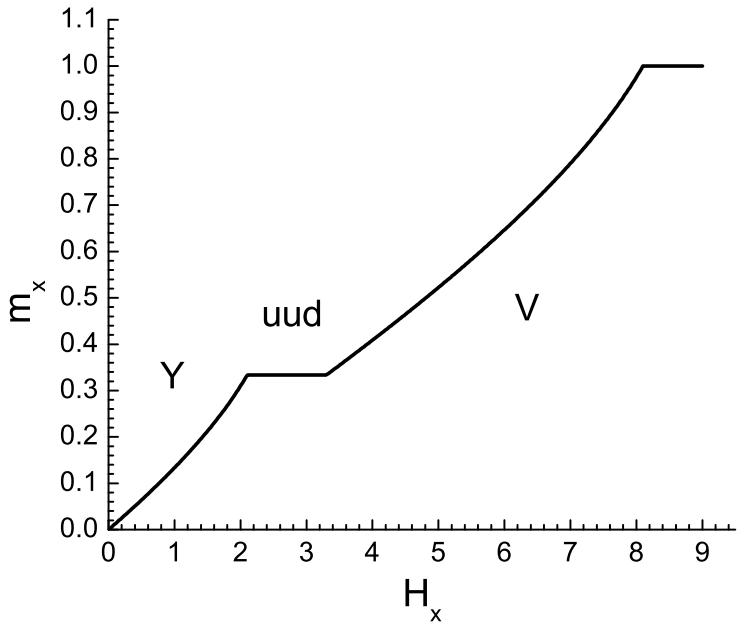

Figure 3.2: Magnetization process of the single-layer TLAF with $\gamma = -0.05$, $D = 0.05$, and $\mathbf{H} \parallel x$-axis. Reprinted with permission from [M Li, M L Plumer, and G Quirion, Journal of Physics: Condensed Matter, 32(13):135803, 2020]. Copyright (2020) by Institute of Physics.

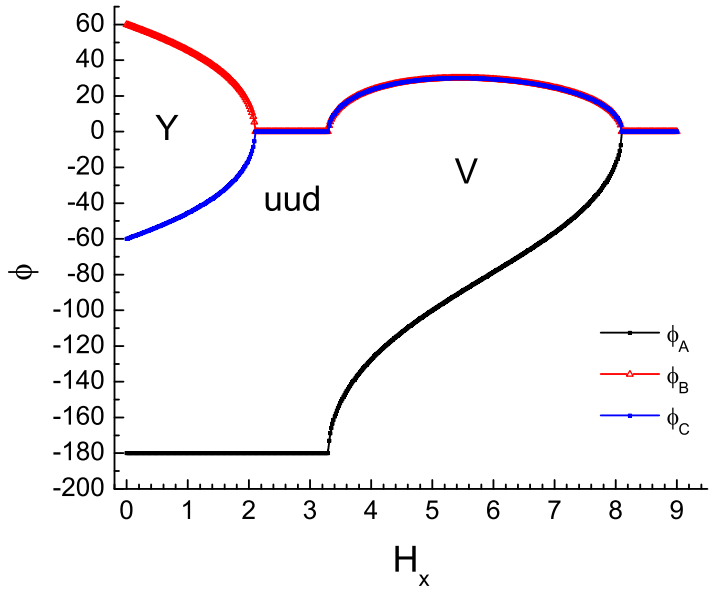

Figure 3.3: The field dependence of the angles ϕ_i for the single layer TLAFs with $\gamma = 0.05$, $D = 0.05$, and $\mathbf{H} \parallel x$-axis. The angles $\theta_i = 90°$ due to the easy-plane anisotropy. Reprinted with permission from [M Li, M L Plumer, and G Quirion, Journal of Physics: Condensed Matter, 32(13):135803, 2020]. Copyright (2020) by Institute of Physics.

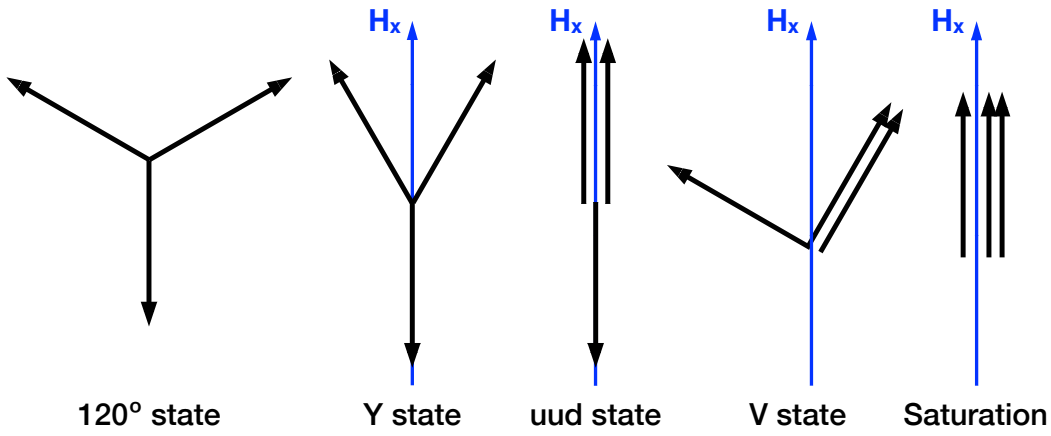

Figure 3.4: Spin configurations of a 2D TLAF with easy-plane anisotropy and $\mathbf{H} \parallel a$-axis in different phases. Arrows represent spins of the ions on the sublattice vertices. Also see Ref. [11]. Reprinted with permission from [M Li, M L Plumer, and G Quirion, Journal of Physics: Condensed Matter, 32(13):135803, 2020]. Copyright (2020) by Institute of Physics.

3.2.2 $\mathbf{H} \parallel c$-axis: $J_c = 0$

With $\mathbf{H} \parallel z \parallel \hat{c}$, the magnetization curve m_z obtained from the one-layer model ($J_c = 0$) is shown in Fig. 3.5, while the different spin congurations are presented in Fig. 3.6. The Umbrella state (U state) and V_z state, associated with the observation of a first order phase transition in experiments [6,9,65], are stabilized at low fields and high fields, respectively. In the U state, the spins adopt a 120° configuration in the ab plane with a uniform component along the z-axis (the field direction in this case). V_z state is observed with all spins lying in a plane including the z-axis. Furthermore, the V_z state is also characterized by a small none-zero magnetization perpendicular to the z-axis (shown in the inset of Fig. 3.5).

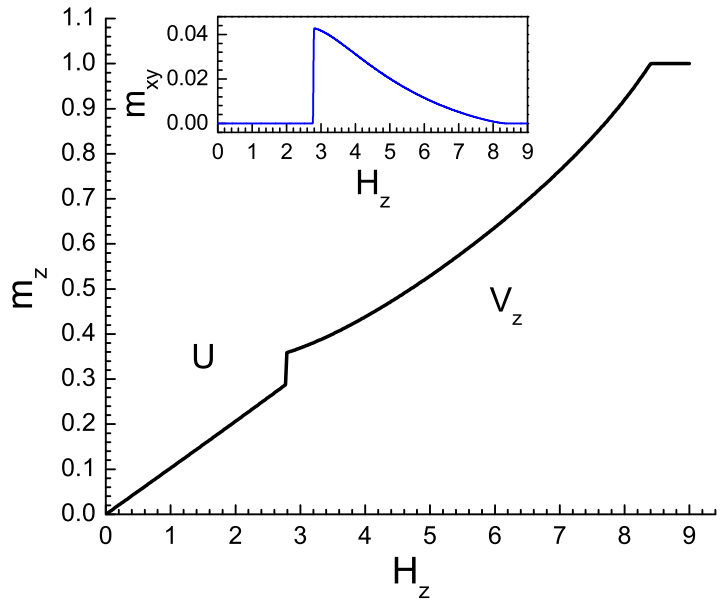

Figure 3.5: Magnetization process of the single-layer TLAF with $\gamma = -0.05$, $D = 0.05$, and $\mathbf{H} \parallel z$-axis. The inset shows the xy component of the magnetization. Reprinted with permission from [M Li, M L Plumer, and G Quirion, Journal of Physics: Condensed Matter, 32(13):135803, 2020]. Copyright (2020) by Institute of Physics.

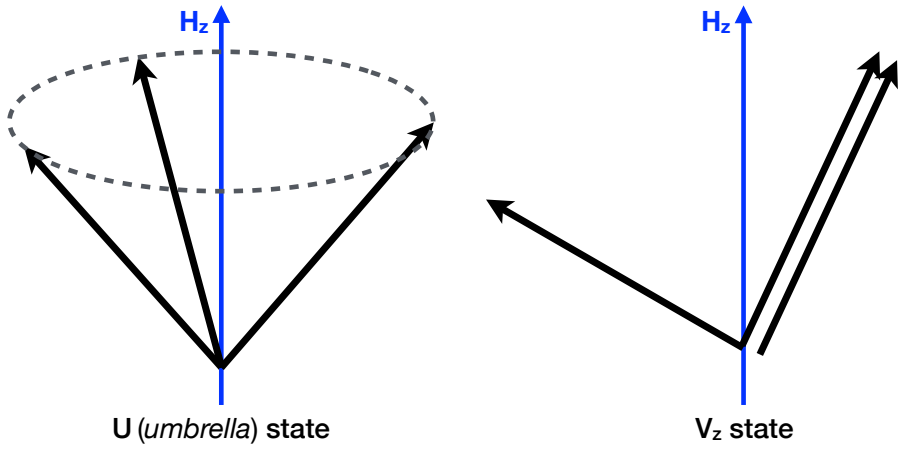

Figure 3.6: Spin configurations of a 2D TLAF with easy-plane anisotropy and $\mathbf{H} \parallel z$-axis in different phases. Arrows represent spins of the ions on the sublattice vertices. Reprinted with permission from [M Li, M L Plumer, and G Quirion, Journal of Physics: Condensed Matter, 32(13):135803, 2020]. Copyright (2020) by Institute of Physics.

The results are consistent with the experimental results [6, 9, 65] and previous theoretical 2D results [2,5,8,11,74,92–94]. Considering that the effective Hamiltonian (Eq. 3.2) adequately describes the magnetic properties of 2D TLAF, it can be easily modified (Eq. 3.3) in order to explore the properties of 3D TLAF with easy-plane anisotropy, which we present in the following section.

3.3 H $\parallel$ *ab*-plane: two planes

In this section, the effects of J_c with different values in the range $0 < J_c \leq 0.21$ are explored with $\mathbf{H} \parallel ab$-plane and fixed values of γ (-0.05) and D (0.05), the same as for the previous 2D model (Sec. 3.2). Different magnetization processes, obtained in specific ranges, are shown in the following subsections.

3.3.1 $0 < J_c < 0.1$

In this range, compared with the 2D model magnetization (Fig. 3.2), one additional C (canted) phase is obtained between the plateau and the V phase as shown in Fig. 3.7(a) (black curve) with the first derivative of the magnetization (red curve) assisting to identify phase transitions. This result is consistent with results of the quantum model published in Ref. [11] using a numerical cluster mean-field method with a scaling scheme. The spin configurations for the quasi-2D Y state, uud state, C state and V state are sketched in Fig. 3.8. In each layer of the C phase, two spins have a small angle with respect to each other, with the third one on the other side of $\mathbf{H}_x$ in xy-plane. Furthermore, as shown in Fig. 3.7(b), the Y and V phases have a small none-zero y-component (perpendicular to the x-axis) of the magnetization which alternates from one plane to the next. This figure (see the divergence of the red curve in Fig. 3.7(a)) also clearly illustrates the first order character of the phase transition between the C and V states. Consequently, we conclude that interlayer interaction, even weak compared with the intralayer exchange interaction, stabilizes a new state and modifies the spin configurations relative to the 2D system.

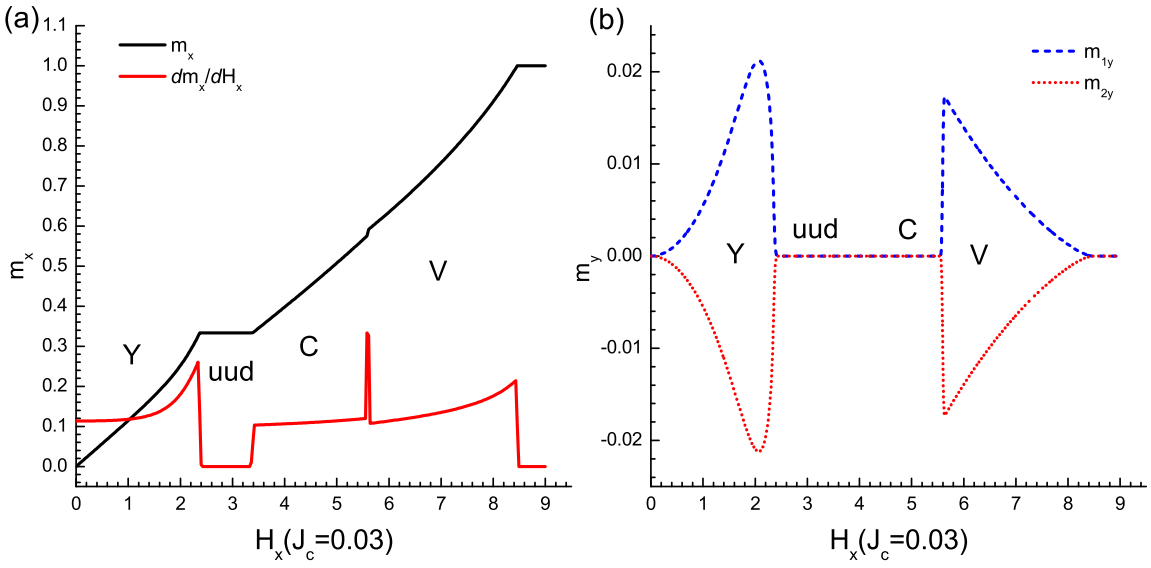

Figure 3.7: (a) The black curve represents the magnetization process of the two-layer TLAF with $\gamma = -0.05$, $D = 0.05$, $J_c = 0.03$, and $\mathbf{H} \parallel x$-axis. The first derivative of the magnetization (red curve) assists to identify phase transitions. (b) The dashed red and blue lines represent the y-component of the magnetization in each layer, respectively. Reprinted with permission from [M Li, M L Plumer, and G Quirion, Journal of Physics: Condensed Matter, 32(13):135803, 2020]. Copyright (2020) by Institute of Physics.

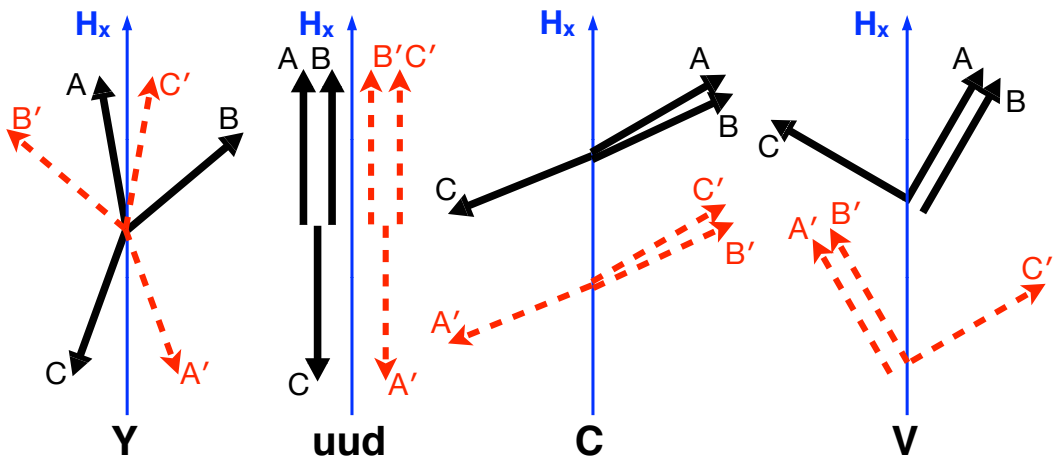

Figure 3.8: Spin configurations of TLAFs with interlayer interaction and $\mathbf{H} \parallel x$-axis in Y, uud, C and V states. Black solid arrows (A, B, C) and red dotted arrows (A′, B′, C′) represent spins at the sublattice vertices in different layers, respectively. (See Fig. 3.1) Reprinted with permission from [M Li, M L Plumer, and G Quirion, Journal of Physics: Condensed Matter, 32(13):135803, 2020]. Copyright (2020) by Institute of Physics.

3.3.2 $0.10 < J_c < 0.14$

For J_c larger than 0.10, as shown in Fig. 3.9(a), the magnetization plateau disappears. Therefore, in the range $0.10 < J_c < 0.14$, the system transforms directly from the Y state to the C state via a first-order transition indicated by a jump on the magnetization and the divergence of the first derivative of the magnetization in Fig. 3.9(a).

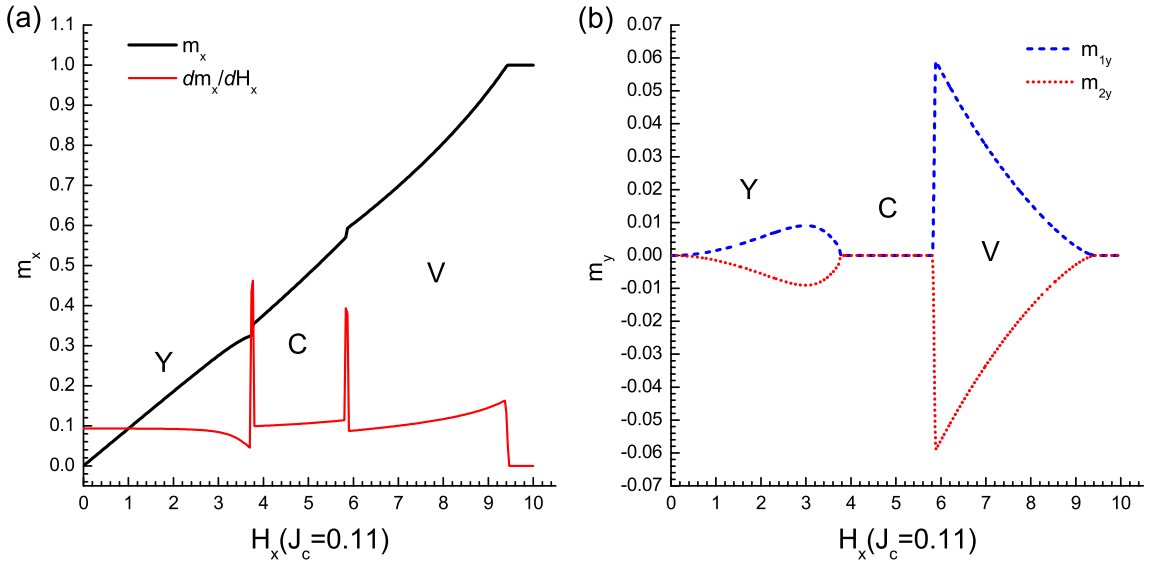

Figure 3.9: (a) The black curve represents the magnetization process of the two-layer TLAF with $\gamma = -0.05$, $D = 0.05$, $J_c = 0.11$, and $\mathbf{H} \parallel x$-axis. The first derivative of the magnetization (red curve) assists to identify phase transitions. (b) The dashed red and blue lines represent the y-component of the magnetization in each layer, respectively.

3.3.3 $0.14 < J_c < 0.16$

In this range of J_c, two new states, W state and V′, are obtained whose spin configurations are presented in Fig. 3.10, while the magnetization processes are different in the ranges $0.1400 < J_c < 0.1445$, $0.1445 < J_c < 0.1460$, $0.146 < J_c < 0.156$ and $0.156 < J_c < 0.160$. In the W state, each layer develops a small z-component of the magnetization which alternates from one layer to the next, while the configuration in the xy-plane forms a W shape and a Y shape in different layers, respectively. In the V′ state, while the spin configuration in the xy-plane is identical to that of the the V phase, two spins in each layer have a small z-component in opposite directions, maintaining the z-component magnetization per plane to zero.

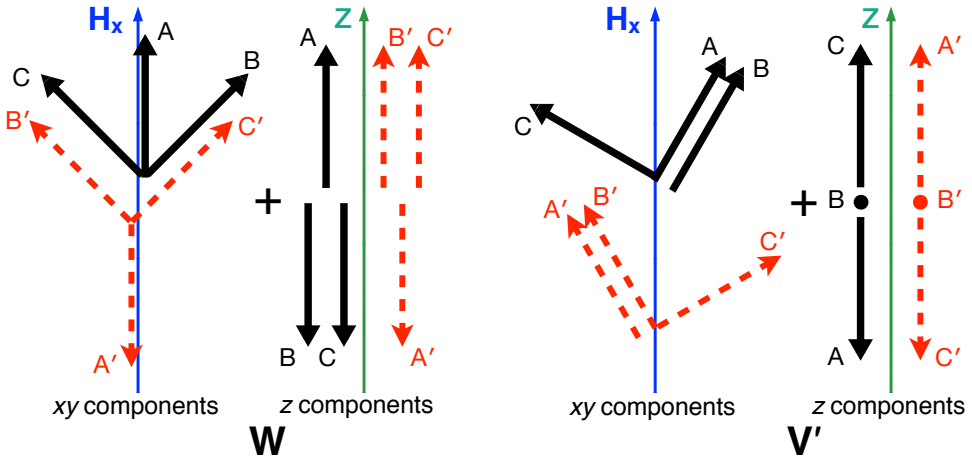

Figure 3.10: Spin configurations of TLAFs with interlayer interaction and $\mathbf{H} \parallel x$-axis in W and V′ states. Black solid arrows (A, B, C) and red dotted arrows (A′, B′, C′) represent spins at the sublattice vertices in different layers, respectively. (See Fig. 3.1) Reprinted with permission from [M Li, M L Plumer, and G Quirion, Journal of Physics: Condensed Matter, 32(13):135803, 2020]. Copyright (2020) by Institute of Physics.

For $0.1400 < J_c < 0.1445$, as shown in Fig. 3.11(a), only the V′ state appears between the C state and the V state with opposite nonzero y-component of magnetization in each plane (see Fig. 3.11(b)). Considering the spin configurations of V and V′ states with the magnetization process shown in Fig. 3.11, it indicates that the phase transition between V and V′ states is of the second order.

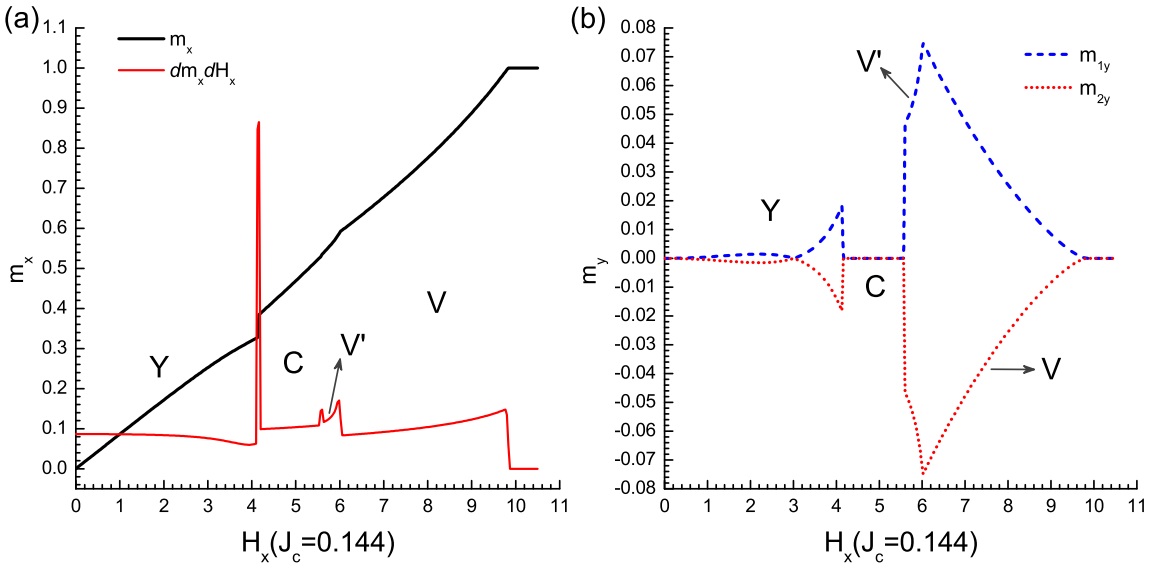

Figure 3.11: (a) The black curve represents the magnetization process of the two-layer TLAF with $\gamma = -0.05$, $D = 0.05$, $J_c = 0.144$, and $\mathbf{H} \parallel x$-axis. The first derivative of the magnetization (red curve) assists to identify phase transitions. (b) The dashed red and blue lines represent the y-component of the magnetization in each layer, respectively.

In the small range $0.1445 < J_c < 0.1460$, the W state exist between C and V′ state (see Fig. 3.12(a)). Fig. 3.12(b) presents that the W state have no y-component of magnetization, while Fig. 3.12(c) shows the opposite nonzero z-component of magnetization of the W state in each layer.

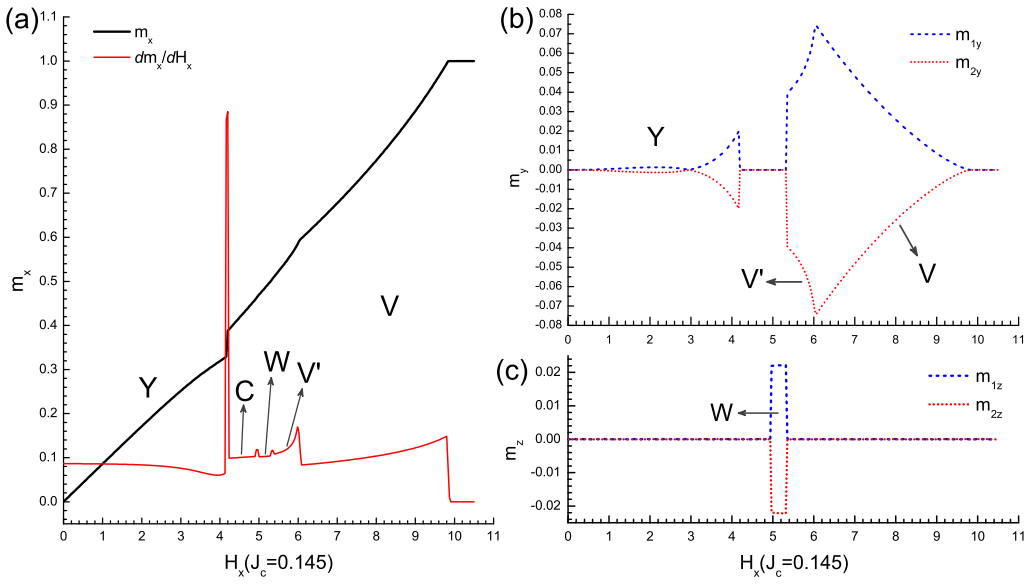

Figure 3.12: (a) The black curve represents the magnetization process of the two-layer TLAF with $\gamma = -0.05$, $D = 0.05$, $J_c = 0.145$, and $\mathbf{H} \parallel x$-axis. The first derivative of the magnetization (red curve) assists to identify phase transitions. (b) The dashed red and blue lines represent the y-component of the magnetization in each layer, respectively.

For $0.146 < J_c < 0.156$, the C state disappears while W and V′ states exist between Y and V states as shown in Fig. 3.13. Considering the jump of the magnetization and the divergence of the first derivative of the magnetization between Y and W states, it indicates the system transforms from the Y state to the W state via a first-order transition.

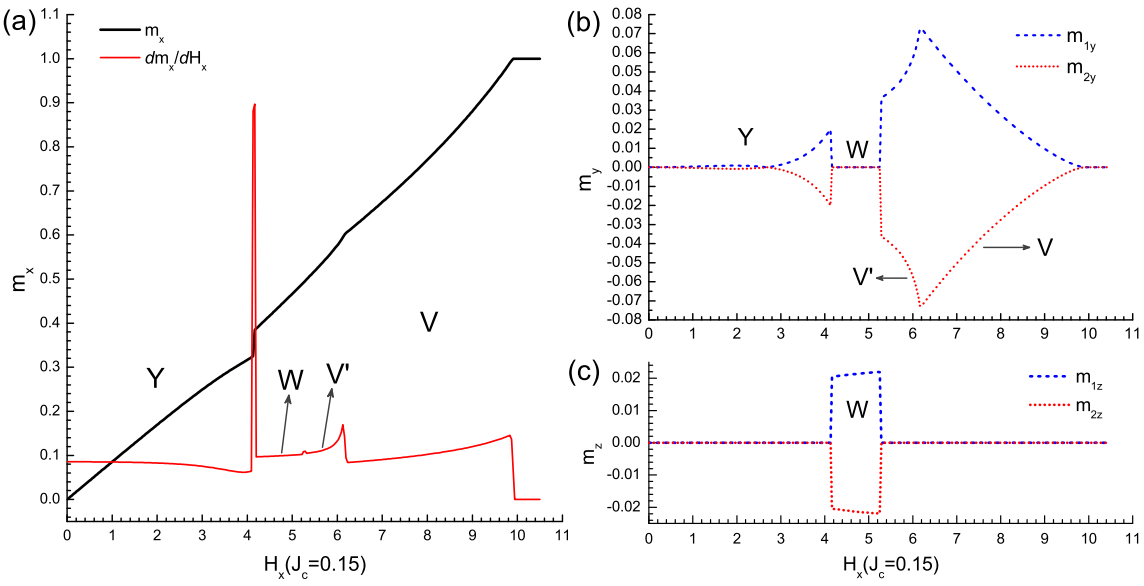

Figure 3.13: (a) The black curve represents the magnetization process of the two-layer TLAF with $\gamma = -0.05$, $D = 0.05$, $J_c = 0.15$, and $\mathbf{H} \parallel x$-axis. The first derivative of the magnetization (red curve) assists to identify phase transitions. (b) The dashed red and blue lines represent the y-component of the magnetization in each layer, respectively.

In the range $0.156 < J_c < 0.160$, only the y and z components of magnetizations for the two layers can distinguish W and V′ states as shown in Fig. 3.14(b) and (c) that the W state exist between two V′ states. Although the first derivative of magnetization cannot identify the phase transitions between W and V′ states (see Fig. 3.14(a)), it points out that the phase transition between Y and V′ states is of the first order by the divergence.

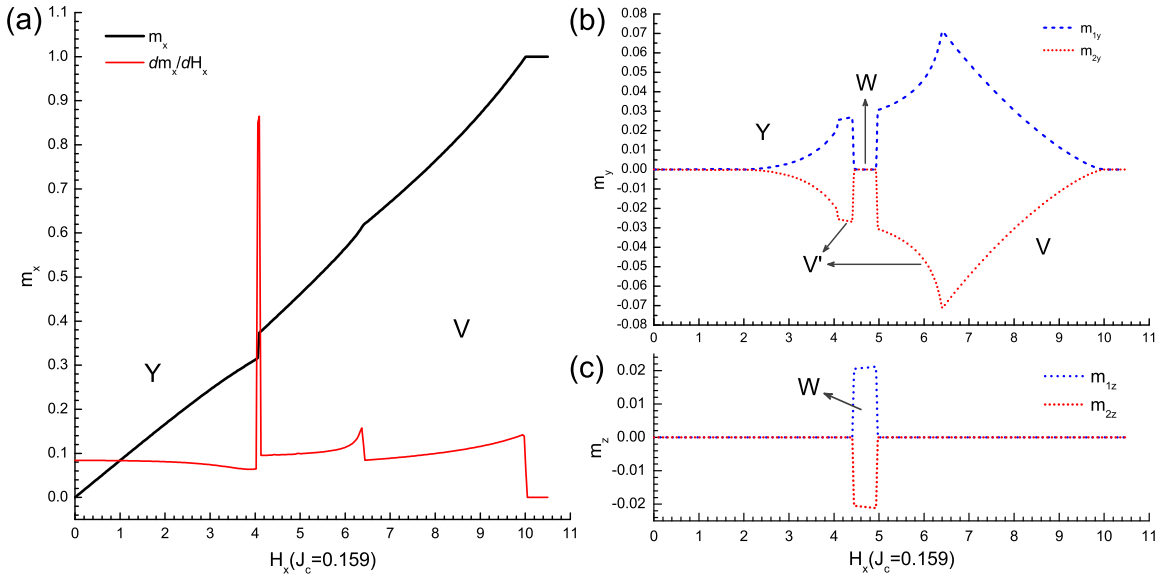

Figure 3.14: (a) The black curve represents the magnetization process of the two-layer TLAF with $\gamma = -0.05$, $D = 0.05$, $J_c = 0.159$, and $\mathbf{H} \parallel x$-axis. The first derivative of the magnetization (red curve) assists to identify phase transitions. (b) The dashed red and blue lines represent the y-component of the magnetization in each layer, respectively. Reprinted with permission from [M Li, M L Plumer, and G Quirion, Journal of Physics: Condensed Matter, 32(13):135803, 2020]. Copyright (2020) by Institute of Physics.

3.3.4 $0.16 < J_c < 0.21$

For $J_c > 0.16$, only the V′ state exists between the Y and V states as shown in Fig. 3.15.

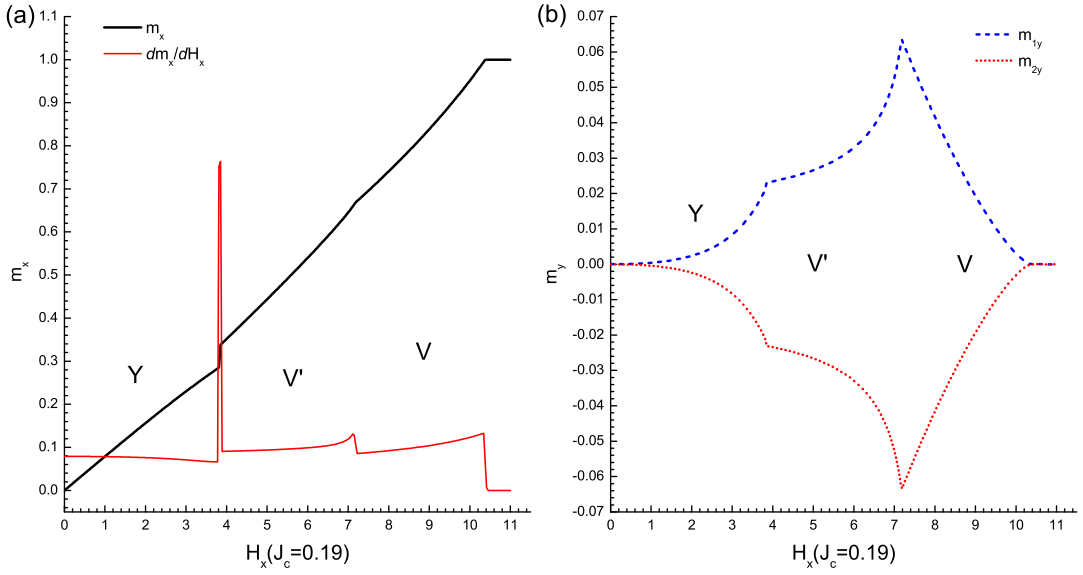

Figure 3.15: (a) The black curve represents the magnetization process of the two-layer TLAF with $\gamma = -0.05$, $D = 0.05$, $J_c = 0.19$, and $\mathbf{H} \parallel x$-axis. The first derivative of the magnetization (red curve) assists to identify phase transitions. (b) The dashed red and blue lines represent the y-component of the magnetization in each layer, respectively.

3.3.5 Analysis for W and V′ states

To explain the appearance of a spin polarization normal to the *ab*-plane in the W and V′ states, we compare the energy of the anisotropic term (E_a) and the interlayer interaction (E_c), which involve the z component of the spins (see Eq. 3.6).

$$\begin{aligned} E_a =& \frac{D}{2}(S_{Az}^2 + S_{A'z}^2 + S_{Bz}^2 + S_{B'z}^2 + S_{Cz}^2 + S_{C'z}^2) \\ E_c =& J_c(S_{Az}S_{A'z} + S_{Bz}S_{B'z} + S_{Cz}S_{C'z}) \end{aligned} \tag{3.6}$$

When J_c is zero or very small, the energy is minimized by having no z component ($D > 0$, easy-plane). However, when J_c is large enough ($\sim$0.14), the lowest energy can be reduced by having anti-parallel z component nearest neighbour interlayer spins as observed in the W and V′ states.

3.3.6 Summary

We present in Fig. 3.16 the H_x-J_c phase diagram for the two-layer TLAFs. The dashed and solid lines indicate first and second order phase transitions, respectively. As shown, the range of the magnetization plateau (uud state) decreases with increasing interlayer interaction and vanishes at $J_c = 0.1$. The C state is only obtained with a weak interlayer interaction and disappears at $J_c = 0.146$. When $0.14 < J_c < 0.16$, the W and V′ states, which have a spin z component, are stabilized. Especially in the small range $0.1445 < J_c < 0.1460$, the system presents the most complicated magnetization process with all new states, C, W and V′ states, which do not exist in 2D model. For $J_c > 0.16$, only the V′ state exists between the Y and V states. Therefore, we can conclude that the interlayer interaction plays an important role in the magnetization process of easy-plane TLAFs.

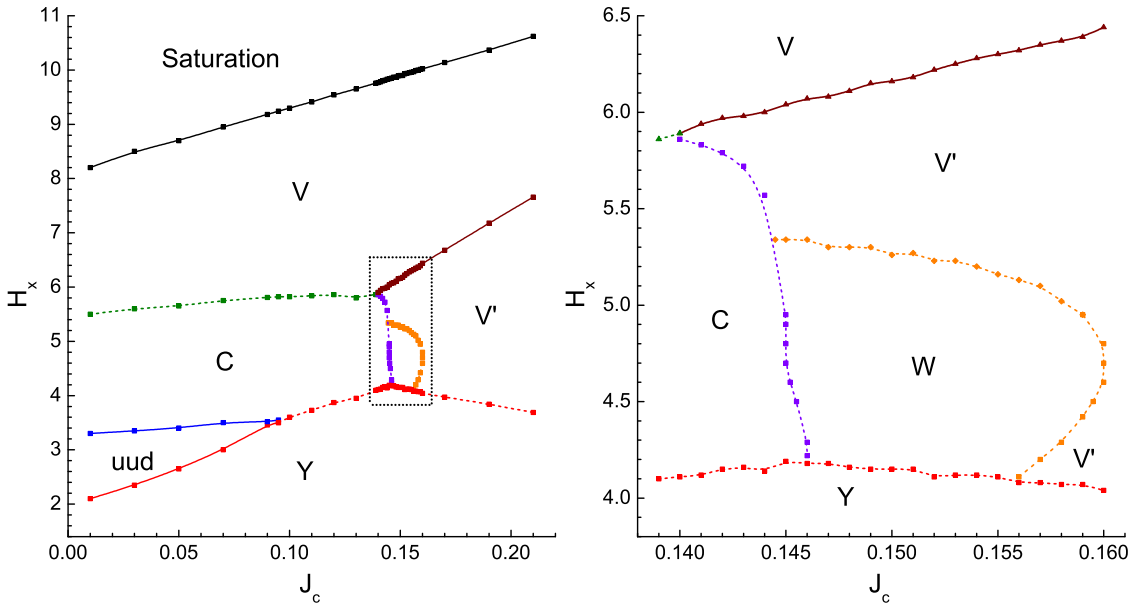

Figure 3.16: Left: H_x-J_c diagram of two-layer TLAFs with $\gamma = -0.05$, $D = 0.05$. Phases are described in Fig. 3.8 and Fig. 3.10. Right: The enlarged region indicated by the dotted rectangle in the left diagram. The dashed and solid lines indicate first and second order phase transitions, respectively. Reprinted with permission from [M Li, M L Plumer, and G Quirion, Journal of Physics: Condensed Matter, 32(13):135803, 2020]. Copyright (2020) by Institute of Physics.

3.4 H $\parallel$ c-plane: two planes

In this section, the effects of J_c with different values in the range $0 < J_c \leq 0.24$ are explored with $\mathbf{H} \parallel c \parallel z$-axis and fixed values of γ (-0.05) and D (0.05), the same as for the previous 2D model (Sec. 3.2). Different magnetization processes, obtained in specific ranges, are shown in the following subsections.

3.4.1 $0 < J_c < 0.06$

For a weak interlayer interaction ($0 < J_c < 0.06$), one extra C_z (canted) state, in comparison with the 2D model magnetization (Fig. 3.5), is obtained between the U state and the V_z state (see Fig. 3.17). The jumps in the magnetization (black curve) and the divergences of the first derivative of magnetization (red curve) indicate that the phase transitions U$\rightarrow$C$_z$ and C$_z$ $\rightarrow$V$_z$ are of the first order. The spin configurations for the quasi-2D U state, V$_z$ state and C$_z$ state are sketched in Fig. 3.18. In each layer of the C$_z$ phase, two spins have a small angle with respect to each other, with the third one is pointing in the opposite direction in a plane including the z-axis. Different from the 2D model, the two-layer V$_z$ state has no net xy-component magnetization perpendicular to the z-axis, while the C$_z$ state has a small transverse magnetization as shown in Fig. 3.17(b).

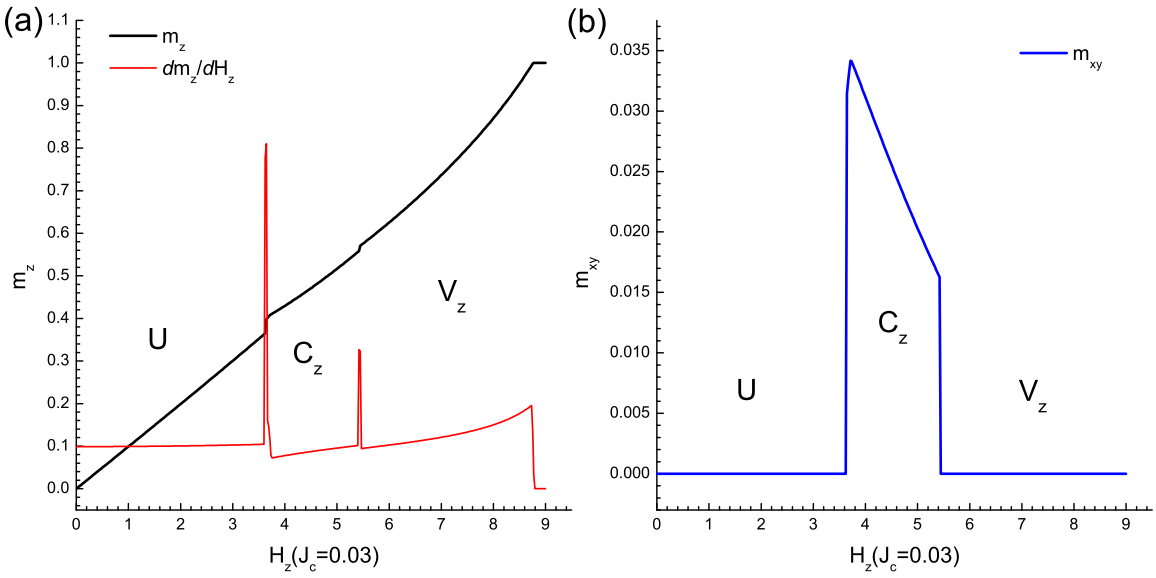

Figure 3.17: (a) The black curve represents the magnetization process of the two-layer TLAF with $\gamma = -0.05$, $D = 0.05$, $J_c = 0.03$, and $\mathbf{H} \parallel z$-axis. The first derivative of the magnetization (red curve) assists to identify phase transitions. (b) The blue curve shows the xy component of the magnetization.

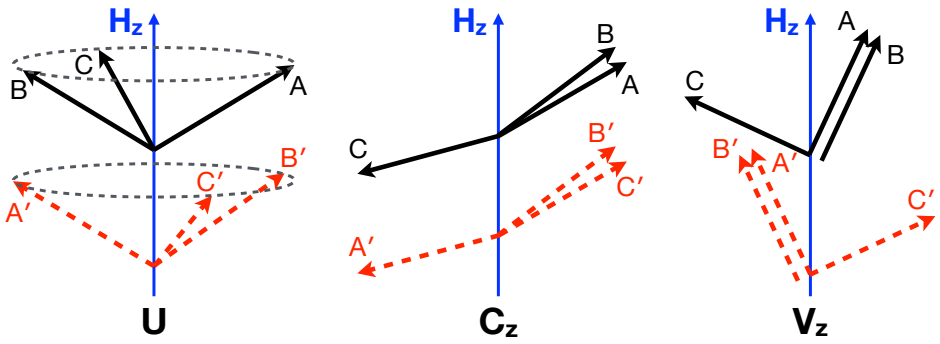

Figure 3.18: Spin configurations of TLAFs with the interlayer interaction and $\mathbf{H} \parallel z$-axis in different phases. Black solid arrows (A, B, C) and red dotted arrows (A′, B′, C′) represent spins at the sublattice vertices in different layers, respectively. Reprinted with permission from [M Li, M L Plumer, and G Quirion, Journal of Physics: Condensed Matter, 32(13):135803, 2020]. Copyright (2020) by Institute of Physics.

3.4.2 $0.06 < J_c < 0.20$

In this range, C_z states disappears while the system transforms from the U state to the V_z state via a first-order transition indicated by the jump on the magnetization (black curve) and the divergence of a first derivative of the magnetization (red curve) in Fig. 3.19.

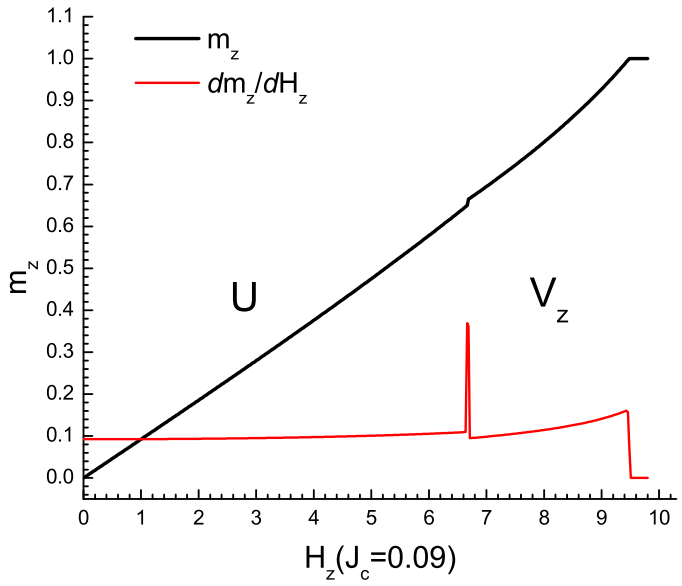

Figure 3.19: The black curve represents the magnetization process of the two-layer TLAF with $\gamma = -0.05$, $D = 0.05$, $J_c = 0.09$, and $\mathbf{H} \parallel z$-axis. The first derivative of the magnetization (red curve) assists to identify phase transitions.

3.4.3 $0.20 < J_c < 0.24$

For $J_c > 0.20$, only the U state exists before the magnetization saturation as shown in Fig. 3.20.

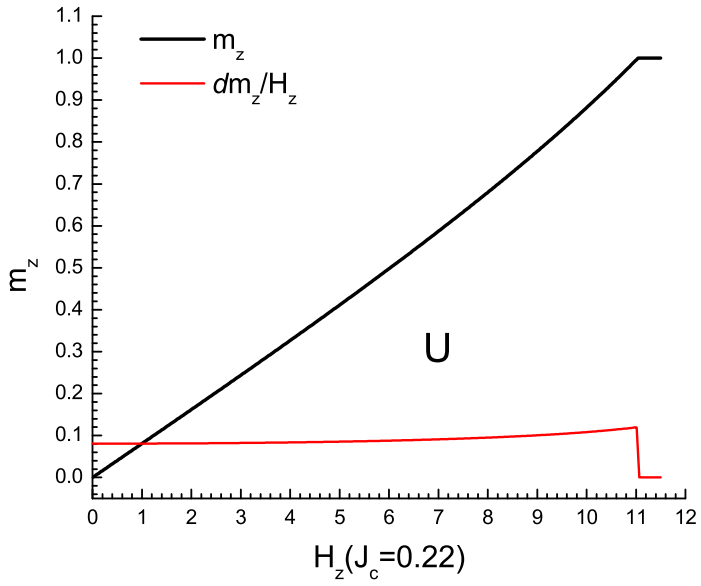

Figure 3.20: The black curve represents the magnetization process of the two-layer TLAF with $\gamma = -0.05$, $D = 0.05$, $J_c = 0.22$, and $\mathbf{H} \parallel z$-axis. The first derivative of the magnetization (red curve) assists to identify phase transitions.

3.4.4 Summary

The resulting H_z-J_c phase diagram for the two-layer TLAFs is presented in Fig. 3.21 with dashed and solid lines representing first and second order phase transitions, respectively. With weak interlayer interaction ($0 < J_c < 0.06$), the C_z state is predicted and its field stability range decreases as a function of J_c. The range of the V_z state increases in $0 < J_c < 0.06$, then decreases in the interval $0.06 < J_c < 0.20$. In contrast, the U state keeps increasing with the increment of J_c. In conclusion, the results for $\mathbf{H} \parallel z$-axis provides another evidence for the importance of the interlayer interaction of the TLAFs.

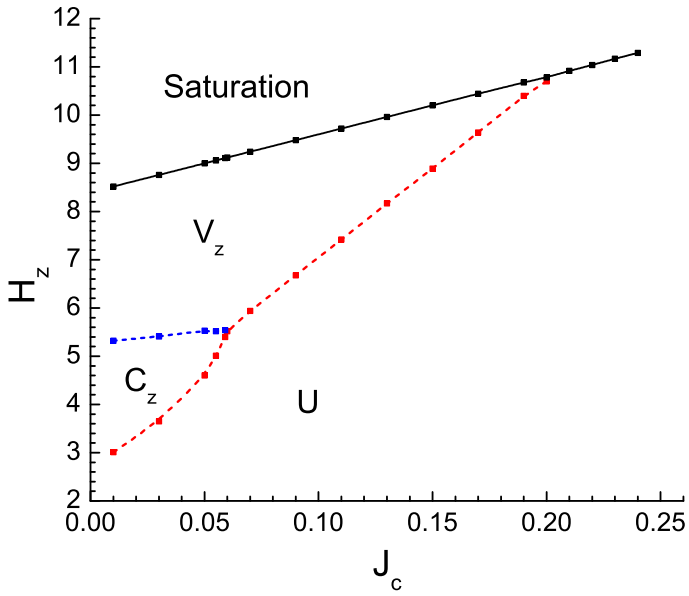

Figure 3.21: H_z-J_c diagram of two-layer TLAFs with $\gamma = -0.05$, $D = 0.05$. Phases are described in Fig. 3.18. The dashed and solid lines indicate first and second order phase transitions, respectively. Reprinted with permission from [M Li, M L Plumer, and G Quirion, Journal of Physics: Condensed Matter, 32(13):135803, 2020]. Copyright (2020) by Institute of Physics.

3.5 Summary and Discussion

The ground state magnetization processes of TLAFs are calculated for both **H** in the *ab*-plane and **H** $\parallel$ *c*-axis using a two-layer classical Heisenberg model with the single ion anisotropy (D) and the bi-quadratic exchange coupling (γ). To study realistic 3D TLAFs, we explored the effect of the antiferromagnetic interlayer interaction (J_c). Results with **H** $\parallel$ *ab*-plane and **H** $\parallel$ *c*-axis shows that the interlayer interaction plays a role for stabilizing the additional state (C state), consistent with Ref. [11]. This additional state could account for the magnetization anomaly observed near 3/5 M_s in $Ba_3CoSb_2O_9$ with **H** in the *ab*-plane [6]. Other new states, not previously reported, are also observed with higher values of the interlayer interaction. The range of field, over which all states are stabilized, depends on the value of J_c. Moreover, the spin configurations of the W and V$'$ states show the appearance of small z components associated with the interlayer interaction competing with the single ion anisotropy. Due to this competition, the system exhibits complex magnetization processes, especially when $0.144 < J_c < 0.146$ (see Fig. 3.16). It should be noticed that the values of J_c for the W and V$'s$ states are large compared with the small J_c value which accounts for the magnetization plateau, but still about one order of magnitude smaller than the intralayer interaction J. Therefore, this model can still be considered to be quasi-2D, with the interlayer exchange coupling playing an important role. Furthermore, all ground states of the two layer model have the same ordering wave vector $\mathbf{Q} = (1/3, 1/3, 1/2)$. Future work using Monte Carlo simulation to explore the H-T phase diagram, such as that on pyrochlore [72], would be of interest. We believe that a detailed analysis of relevant experimental results on existing and yet to be discovered TLAFs may benefit from the results present here.

Chapter 4

Ultrasonic velocity measurements

4.1 Sound velocity measurements

The measurement of the relative ultrasound velocity variation $\Delta v/v$ is a high-precision method to detect the critical behaviour close to a phase transition. This technique can also be used to determine the magnetoelastic coupling accurately, since strains and magnetic degrees of freedom couple with each other [9]. Therefore, in this work, we developed an experimental approach using the ultrasonic velocity measurements, which does not rely on traditional magnetostriction measurements [100], to study the contribution of the magnetoelastic coupling for lifting the classical degeneracy and stabilizing the magnetization plateau in TLAF.

The transducer, bonded on the $Ba_3CoSb_2O_9$ sample by a glue (white silicone), is a piezoelectric crystal coated with gold electrodes (see Fig. 4.1). The piezoelectric crystal can generate an ultrasonic pulse into the sample converting the ac electric signal at a frequency f, applied to the transducer electrodes, into mechanical vibration at the same frequency (inverse piezoelectric effect). Meanwhile, according to the

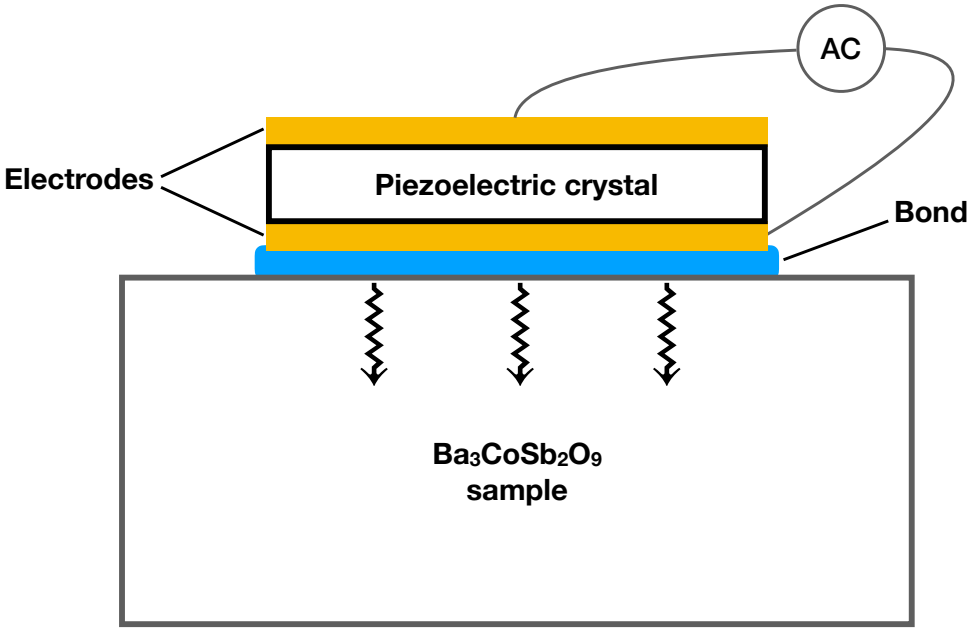

Figure 4.1: The transducer is bonded on the $Ba_3CoSb_2O_9$ sample by a glue.

piezoelectric effect, the piezoelectric crystal can also convert the mechanical vibration into an electrical signal. Therefore, the transducer can serve as both a sound wave generator and a detector. There are two modes of measurements shown in Fig. 4.2. On the left, the reflection mode has one transducer fixed to a surface of the crystal to generate and detect the acoustic wave reflected from the other parallel surface. The initial ultrasound waves travel back and forth between the parallel surfaces of the sample due to the reflection at the surfaces. Small portion of the mechanical wave is converted into an electrical signal. If the acoustic attenuation, which causes the reduction of the amplitude of the echoes (see Fig. 4.3), is not too large, multiple echoes can be detected. In this case, the sound velocity is determined using $v = 2L/t$, where L is the length of the sample and t is the time of flight for the acoustic wave which travels a distance $2L$. In the transmission configuration (right of Fig. 4.2), two transducers fixed on the parallel surfaces of the sample are used. One transducer (the

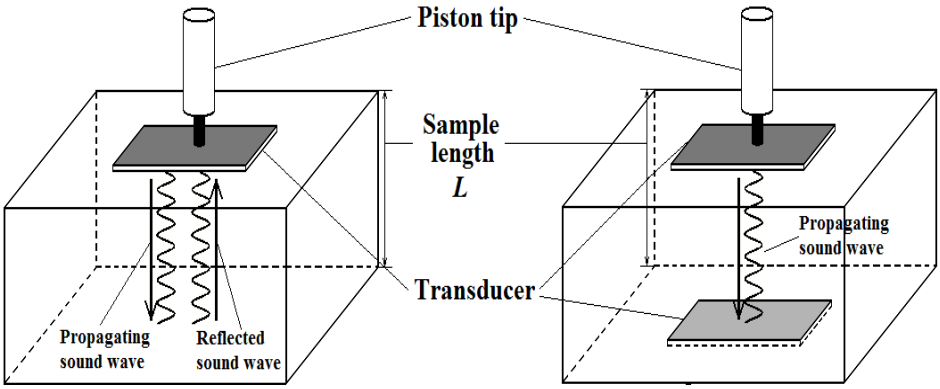

Figure 4.2: Sound velocity measurements: reflection configuration (left) and transmission configuration (right).

top one) generates the acoustic wave which is detected by the other transducer (on the bottom). In the experiment shown in Chapter 5, we use transmission mode in which the sound velocity is determined using $v = L/t$.

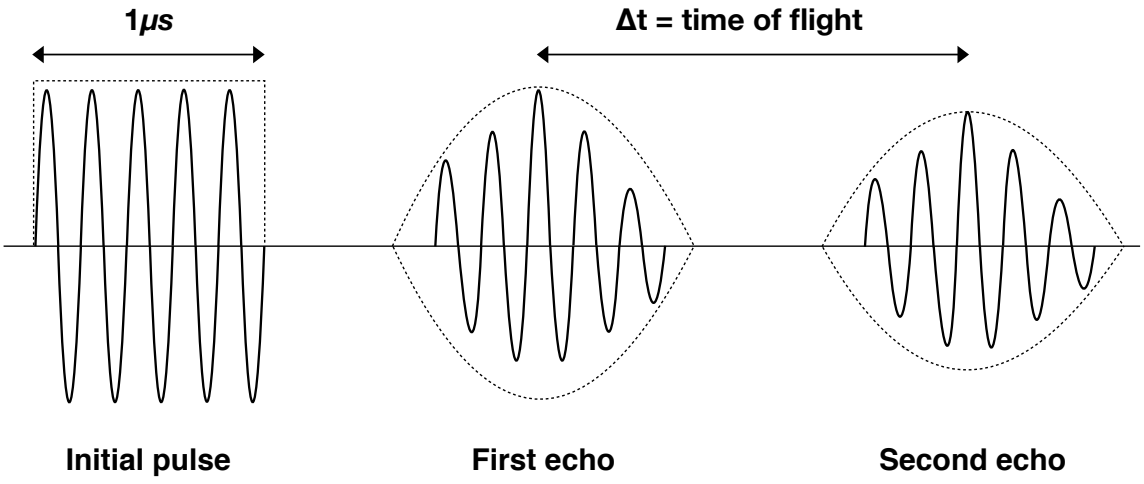

Figure 4.3: Consecutive echoes detected by the receiver in an ultrasonic measurement.

4.2 Acoustic interferometer

The radio frequency (RF) signal, generated by a RF synthesizer, is split into two signals by a power splitter (see Fig. 4.4). The first signal is used as the reference signal, while the other half of the signal is reshaped to form a 1 μs RF pulse signal by the Gate 1. After amplification by a 1 Watt broadband power amplifier, the signal reaches one transducer via the variable attenuator which sets the power of the signal. The transducer, mounted on one surface of the sample, converts the RF pulse signal into an acoustic wave which propagates to the other surface. The acoustic signal is then converted back into a RF signal by the other transducer. This RF signal is amplified by a low noise RF amplifier, after going through Gate 2 which prevents the saturation of the low noise RF amplifier. Finally, the phase detector compares the phase of the reference signal and the converted RF signal, producing an output signal proportional to the phase difference between both inputs. During the experiment, the phase difference is maintained to zero by changing the synthesizer frequency, and observed on the oscilloscope as shown in Fig. 4.4.

The phase difference can be expressed in terms of the time of flight $t = L/v$ and the period $T = 1/f$ of the RF signal as

$$\Phi = \frac{2\pi t}{T} = \frac{2\pi L f}{v}, \tag{4.1}$$

therefore the relative phase difference reduces to

$$\frac{\Delta\Phi}{\Phi} = \frac{\Delta L}{L} + \frac{\Delta f}{f} - \frac{\Delta v}{v} = 0. \tag{4.2}$$

As the phase variation $\Delta\Phi$ is maintained to zero by changing the working frequency, neglecting the thermal expansion of the sample, $\Delta L/L$, as a function of temperature

or magnetic field, the acoustic interferometer can determine the relative ultrasound velocity variation $\Delta v/v$ by directly measuring the variation of the relative frequency $\Delta f/f$:

$$\frac{\Delta v}{v} \approx \frac{\Delta f}{f}. \tag{4.3}$$

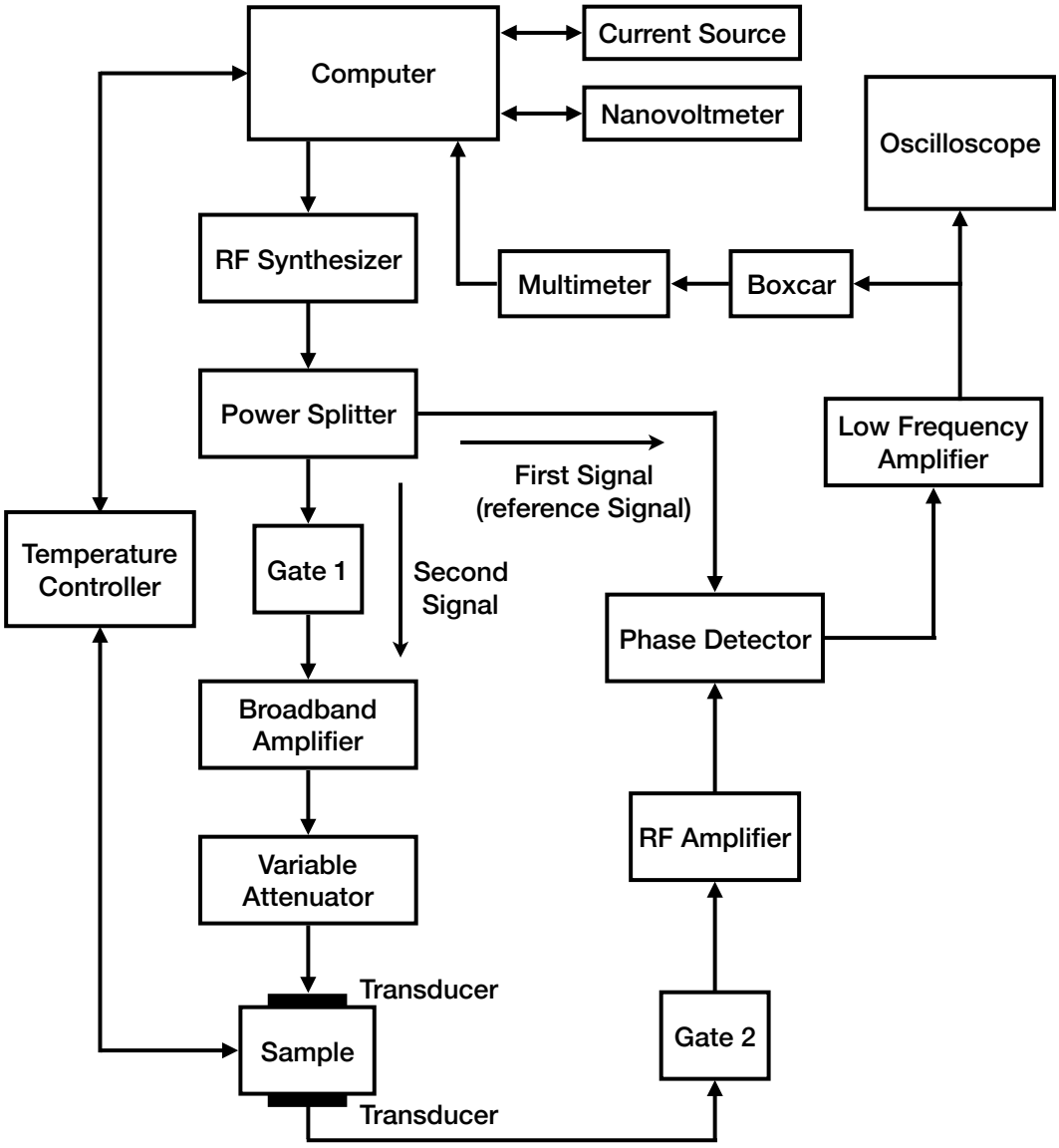

Figure 4.4: Brief block diagram of the acoustic interferometer.

4.3 Cryogenic system

In order to explore the ordered states of $Ba_3CoSb_2O_9$, a helium bath cryostat equipped with superconducting magnets was used for the ultrasonic measurements (see Fig. 4.5). Using this cryogenic system, the temperature can be as low as 2 K with a maximum magnetic field of 18 T.

Liquid helium is transferred into the reservoir after pumping out the air in the sample chamber. The outer chamber is also evacuated in order to reduce the heat transfer from the outside wall of the cryostat. The liquid helium cools down the lower part of the helium reservoir to 4.2 K. Meanwhile, the evaporated helium gas cools the radiation baffles at the higher part of the chamber, and reduces the heat flow due to room temperature radiation. In order to cool down to 4.2 K, the capillary opening (via a needle valve) is adjusted to let the helium flow into the sample chamber in which the $Ba_3CoSb_2O_9$ crystal is mounted. Moreover, a temperature of 2 K around the $Ba_3CoSb_2O_9$ sample can be achieved by decreasing the pressure of the sample chamber using a mechanical pump connected to the sample chamber evacuation valve. Furthermore, the temperature of the sample is controlled by adjusting the input power of the heater fixed on the sample holder, and monitored by a low temperature sensor. Both the heater and the sensor are connected to a temperature controller used for setting the rate of changing temperature of the sample or stabilizing the temperature to a specific value.

The superconducting magnet in the cryogenic system is a solenoid as shown in Fig. 4.5. This magnet can normally produce a variable magnetic field up to 16 T at 4.2 K and be enhanced up to 18 T at 2.2 K. In order to obtain 2.2 K around the magnet, a lambda refrigerator [101] consisting of a lambda plate, a liquid helium valve and a chamber with a pumping line is applied. Liquid helium continuously flows

via the valve into the chamber which is pumped to a low pressure. Therefore, the colder and denser helium below the lambda plate sinks to the bottom of the chamber, and induces convection currents. This convection of the liquid helium maintains the temperature of the magnet at 2.2 K.

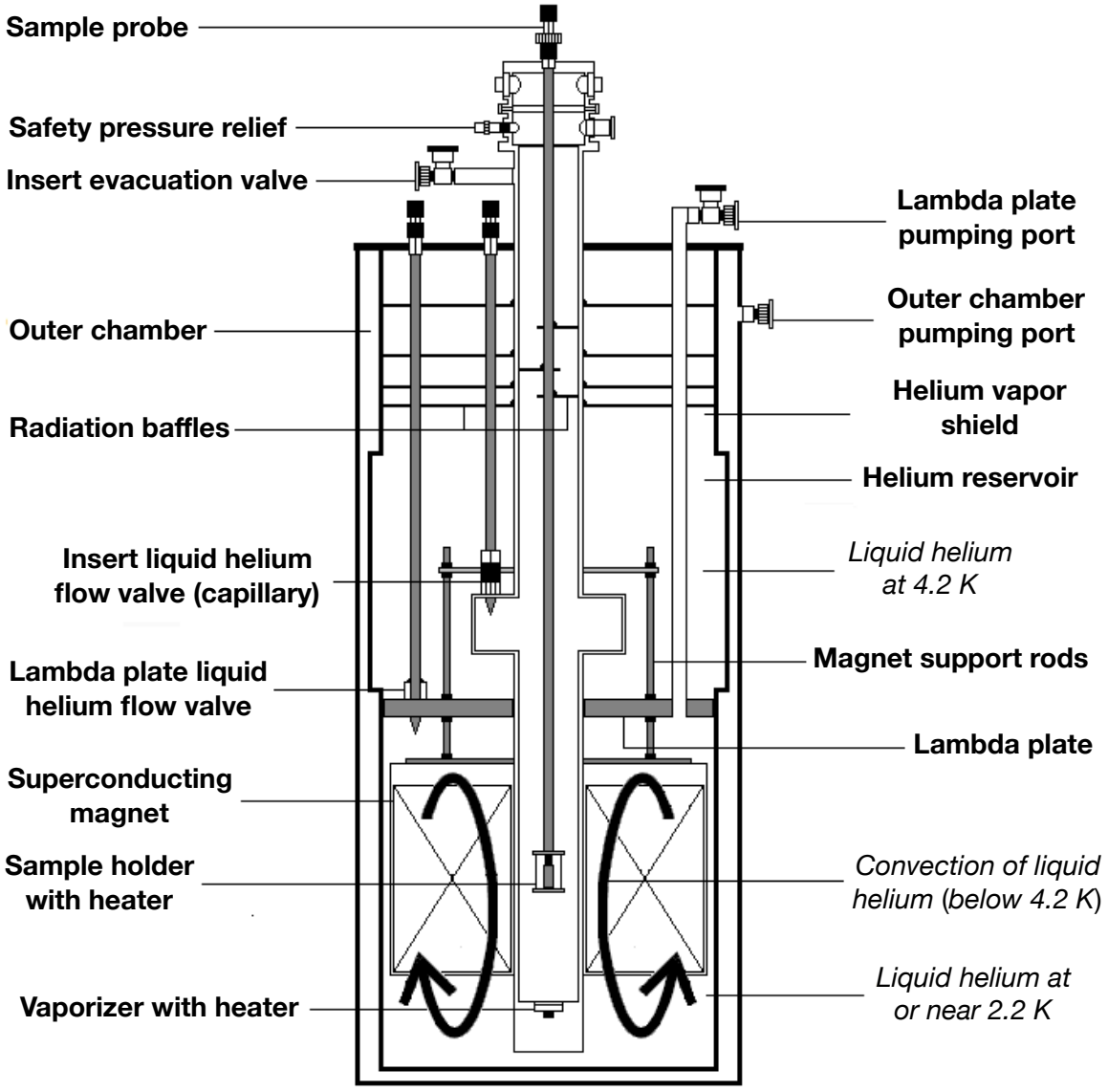

Figure 4.5: Liquid helium cryogenic system with superconducting magnets.

Chapter 5

Experimental setup and results

5.1 Bi-quadratic coupling derived from magnetoelastic coupling

The microscopic origin of the biquadratic exchange coupling term used in Section 3.1 can also be associated with the spin-lattice coupling (magnetoelastic coupling) [70–73], in addition to quantum and thermal fluctuations. As shown in Fig. 5.1, a lattice distortion e_{ij} can be induced by the interaction of magnetic ions leading to a magnetoelastic coupling. As a result, the energy including the magnetoelastic coupling energy and the elastic energy for three ions is

$$E_{Se} = J\sum_{i\neq j}\mathbf{S}_i\cdot\mathbf{S}_j + \sum_{i\neq j}Ke_{ij}(\mathbf{S}_i\cdot\mathbf{S}_j) + \frac{1}{2}\sum_{i\neq j}Ce_{ij}^2 - \frac{1}{3}\mathbf{H}\cdot\sum_i\mathbf{S}_i, \qquad (5.1)$$

where K is the spin-strain coupling constant, and C is the elastic constant. Minimizing relative to the strains, we obtain the solution

$$e_{ij} = -\frac{K}{C}\mathbf{S}_i \cdot \mathbf{S}_j. \tag{5.2}$$

After substituting Eq. 5.2 back into Eq. 5.1, we obtain the effective Hamiltonian

$$E = J\sum_{i\neq j}\mathbf{S}_i \cdot \mathbf{S}_j + \gamma\sum_{i\neq j}(\mathbf{S}_i \cdot \mathbf{S}_j)^2 - \frac{1}{3}\mathbf{H}\cdot\sum_i \mathbf{S}_i, \tag{5.3}$$

with γ giving by

$$\gamma = -\frac{K^2}{2C}. \tag{5.4}$$

Eq. 5.3 is identical to what is used in Chapter 3 for numerical calculation. As the elastic constant C is always positive, γ is negative. Meanwhile, considering $(\mathbf{S}_i \cdot \mathbf{S}_j)^2 > 0$, the Hamiltonian has minimum value with the collinear configuration of spins. Therefore, the magnetoelastic coupling can account for stabilizing the magnetization plateau.

This scenario is especially pertinent in the case of $Ba_3CoSb_2O_9$, since large sound velocity variations ($\Delta v/v \simeq 7\%$) are observed as a function of the magnetic field, reflecting strong magnetoelastic coupling [9]. In this section, we therefore study the relevance of the magnetoelastic coupling relative to quantum fluctuations in stabilizing the magnetization plateau in this archetype spin-1/2 quantum TLAF material [6, 46, 64, 78]. Our goal is achieved using an experimental approach based on ultrasound velocity measurements [102]. It consists in measuring the relative velocity variation of an acoustic mode at constant temperatures and fields as the in-plane field direction is changed relative to the a-axis. The measured field angular dependence, $\Delta v/v$, is then analyzed within the framework of a mean-field model (see Chapter 6) in

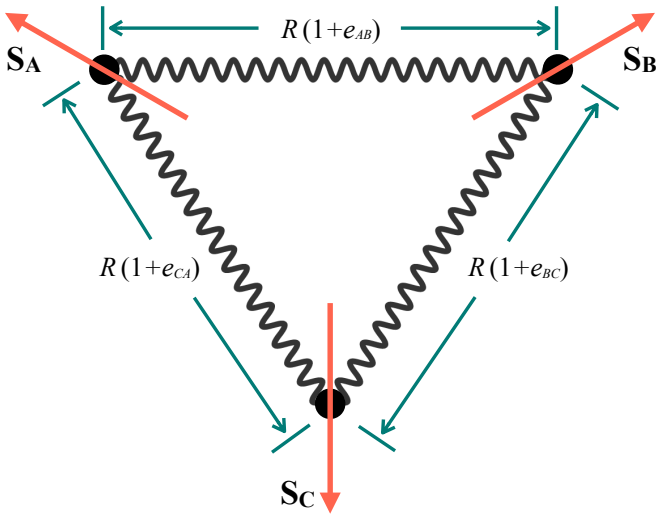

Figure 5.1: Sketch showing the lattice distortion e_{ij} induced by the exchange interaction between nearest magnetic ions on a triangular lattice.

order to determine the magnetoelastic coupling constants which account for the lattice distortions. Moreover, using this experimental measurement, we also measured the sample close to the phase boundary between uud and paramagnetic states (see Fig. 1.8) and at relative high temperature (20 K) to explore the effect of thermal and quantum fluctuations.

5.2 Field angular (ϕ) measurements of the sound velocity

Fig. 5.2 illustrates the geometry used for the field angular (ϕ) measurements of sound velocity obtained at constant temperatures and magnetic field. For this investigation, the velocity measurements were carried out using longitudinal acoustic modes generated and detected with two 30 MHz $LiNbO_3$ transducers mounted on opposite polished faces (transmission configuration). Thus longitudinal modes, propagating

along the a-axis of a single crystal with a length of 2.57 mm, were used to determine the ultrasound velocity $v_{L[100]}$. The relative velocity variation $\Delta v(\phi)/v$, measured at constant temperatures and magnetic fields using a pulsed acoustic interferometer operating around 100 MHz for higher resolution [83], was then recorded as the $Ba_3CoSb_2O_9$ crystal was rotated about the crystal c-axis by an angle ϕ (changing the field direction in the basal plane). Here, $\phi = 0°$ corresponds to the magnetic field parallel to the direction of propagation of the acoustic mode $v_{L[100]}$ (a-axis).

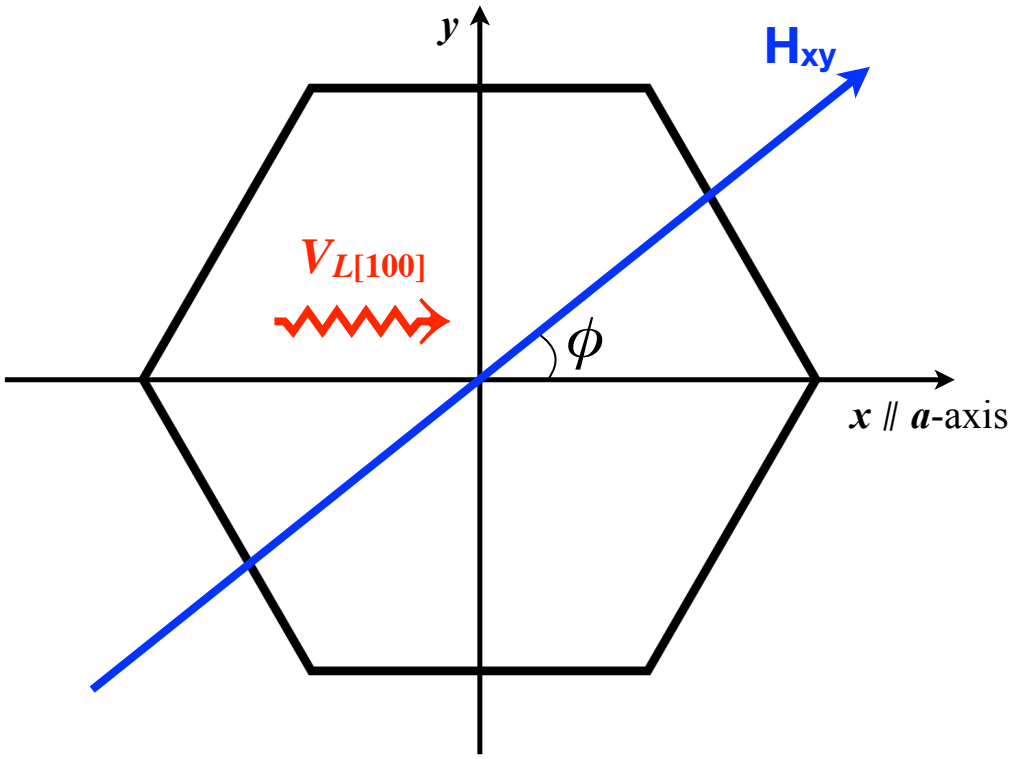

Figure 5.2: Geometry used for the sound velocity measurements as the crystal is rotated about the c-axis by the angle ϕ in the presence of a magnetic field applied in the crystal basal plane.

5.3 Experimental results

5.3.1 Experimental results at $T = 2.5$ K and $T = 10$ K

In Fig. 5.3, we present the field angular (ϕ) dependence of the relative variation of sound velocity ($\Delta v_{L[100]}/v$) measured at different field values: in the paramagnetic state at $T = 10$ K and in the ordered states at $T = 2.5$ K. These experimental results and analysis have been published in Ref. [3]. In the paramagnetic state, a well defined angular period of 180° is observed with a maximum at $\phi \sim 0$ (corresponding to $\mathbf{H} \parallel a$-axis) and a minimum close to $\phi = 90°$. In the Y state, additional extrema emerge around $\phi = 40°$ and 130° while the local minimum observed at 90° suddenly changes into a local maximum as we enter the uud state. Finally, although the amplitude of the relative variations generally increases as a function of the field, it suddenly drops by an order of magnitude in the V state ($\mathbf{H}_{xy} = 16.5$ T). While the evolution of the angular dependence shown in Fig. 5.3 is surprisingly complex, we present in Chapter 7 a magnetoelastic model to analyze these experimental observations.

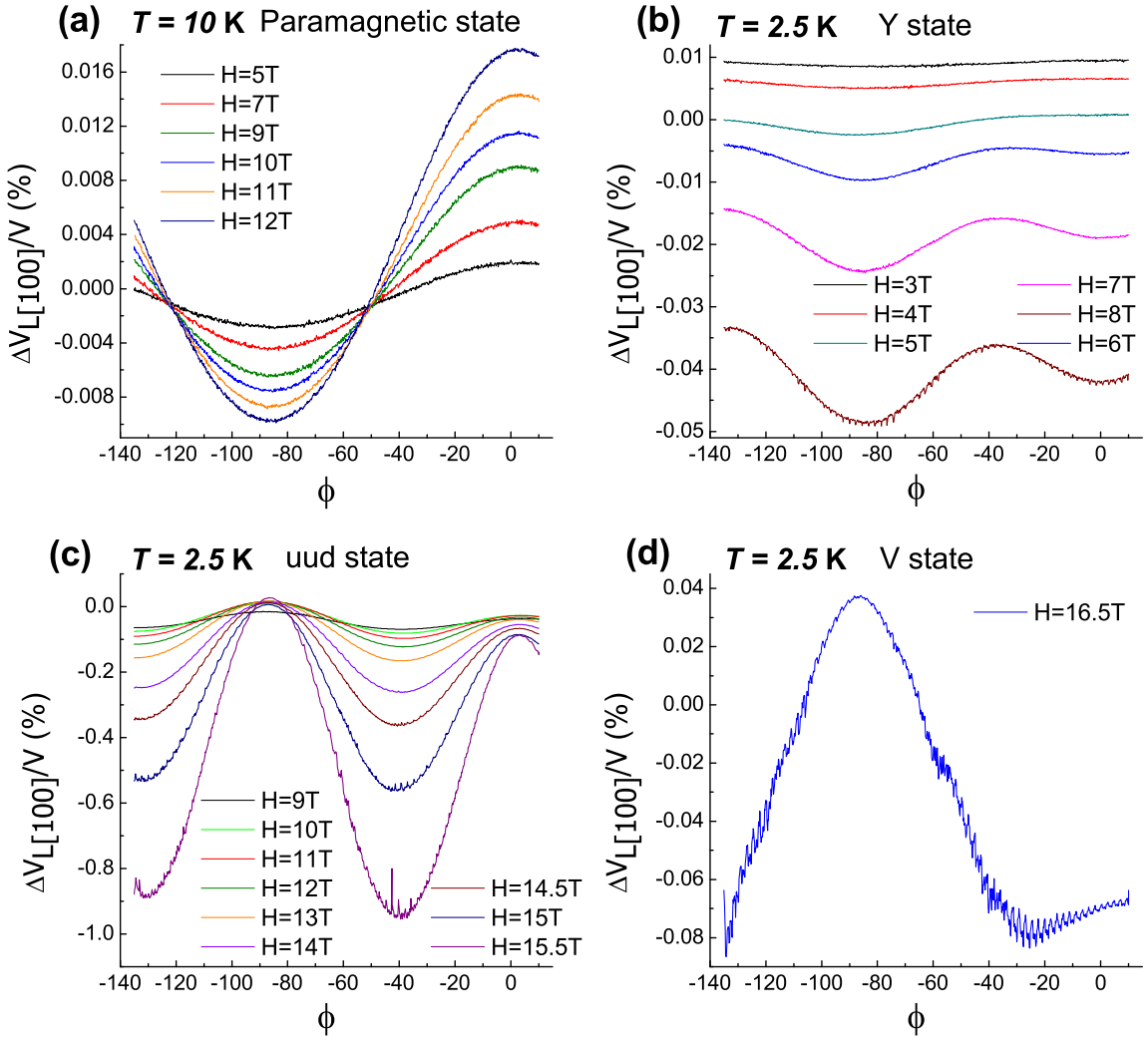

Figure 5.3: Field angular (ϕ) dependence of $v_{L[100]}/v$ for different magnetic field strengths in the basal plane of $Ba_3CoSb_2O_9$, with 0° corresponding to $\mathbf{H} \parallel a$-axis; (a) $T = 10$ K is chosen for paramagnetic state; (b), (c), (d) show results obtained at $T = 2.5$ K in the ordered states (Y, uud, V), respectively. Reprinted with permission from [M. Li, A. Zelenskiy, J. A. Quilliam, Z. L. Dun, H. D. Zhou, M. L. Plumer, and G. Quirion, Phys. Rev. B, 99:094408, 2019]. Copyright (2019) by American Physical Society.

5.3.2 Exploring the effect of thermal and quantum fluctuations

As quantum and thermal fluctuations are considered to be the mechanism lifting the classical degeneracy in favor of the uud state in quasi-2D TLAFs with easy-plane anisotropy [2, 5, 11, 75, 77], we explore the effect of spin fluctuations on the magnetoelastic coupling by measuring the sample at the temperatures as follows. According to the H-T phase diagram of $Ba_3CoSb_2O_9$ (see Fig. 1.8), $T = 5.5$ K and 4.4 K are chosen for exploring the system close to the phase boundary between the uud and the paramagnetic states. In order to compare the results of the ordered states obtained at $T = 2.5$ K, the sample was also measured at $T = 3$ K. Furthermore, we measured the system at a relative high temperature $T = 20$ K.

First we show in Fig. 5.4 the experimental results in the paramagnetic state at $T = 5.5$ K. At low fields ($H < 8$ T), the curves are similar to the results obtained at 10 K shown in Fig. 5.3(a). As the field increases, we approach the uud phase boundary, and a local maximum, which is presented in uud state (see Fig. 5.3(c)), shows up when $H > 9$ T at $\phi \simeq 90°$. Moreover, at $T = 4.4$ K, when the system is in the paramagnetic state with $H \leq 7$ T, the curves, similar to the results obtained at 10 K shown in Fig. 5.3(a), are presented in Fig. 5.5(a). Meanwhile, since the system is in the uud state with higher fields (8 T $\leq H \leq 16$ T), the curves shown in Fig. 5.5(b) are similar to the curves in Fig. 5.3(c). Furthermore, we present the experimental results of Y and uud states at $T = 3$ K in Fig. 5.6(a) and Fig. 5.6(b), respectively. The local maximums and local minimums of the curves in Fig. 5.6 are consistent with the results of the Y and uud states shown in Fig. 5.3(b) and (c). Finally, the curves with 180° period obtained in the paramagnetic state at $T = 20$ K (see Fig. 5.7) are comparable with the results in Fig. 5.3(a).

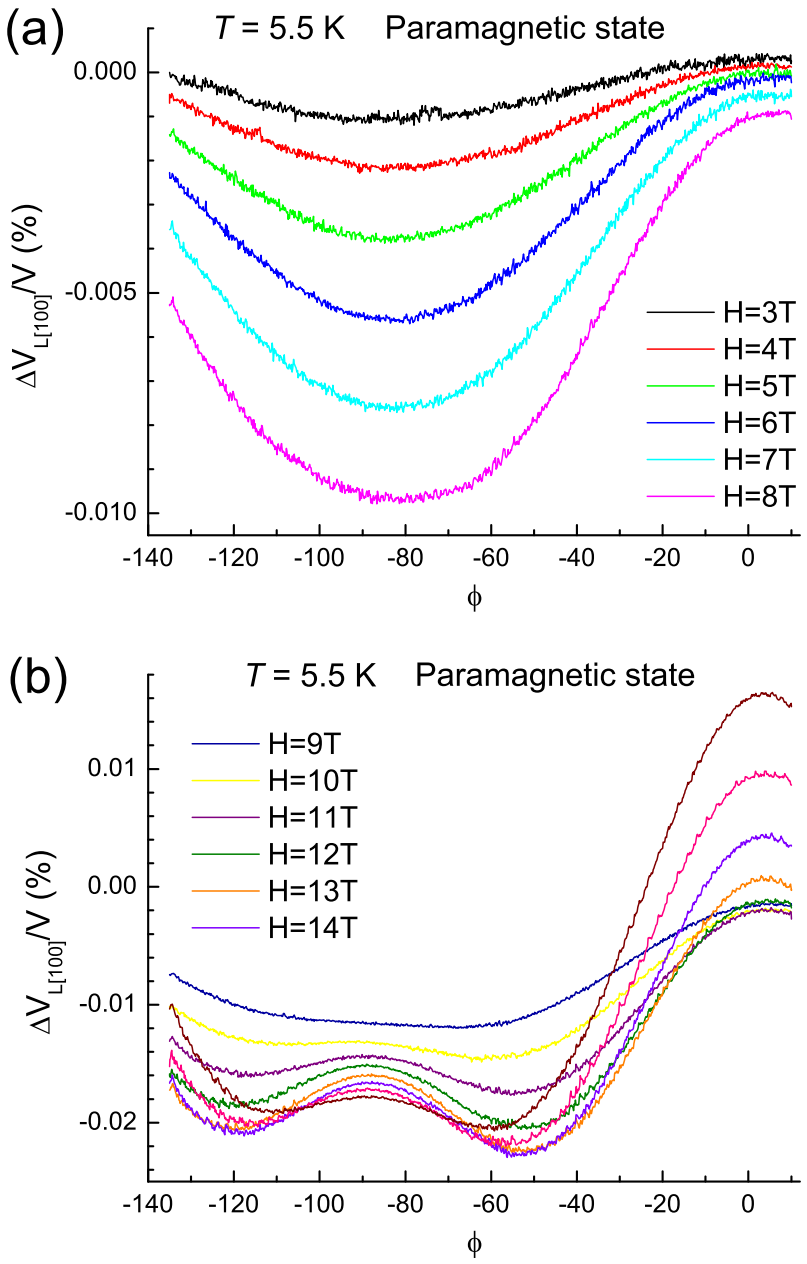

Figure 5.4: Field angular (ϕ) dependence of $v_{L[100]}/v$ for different magnetic field strengths in the basal plane of $Ba_3CoSb_2O_9$, with 0° corresponding to $\mathbf{H} \parallel a$-axis in paramagnetic state at $T = 5.5$ K; (a), (b) show the curves obtained relatively far from and close to the phase boundary between uud and paramagnetic states, respectively.

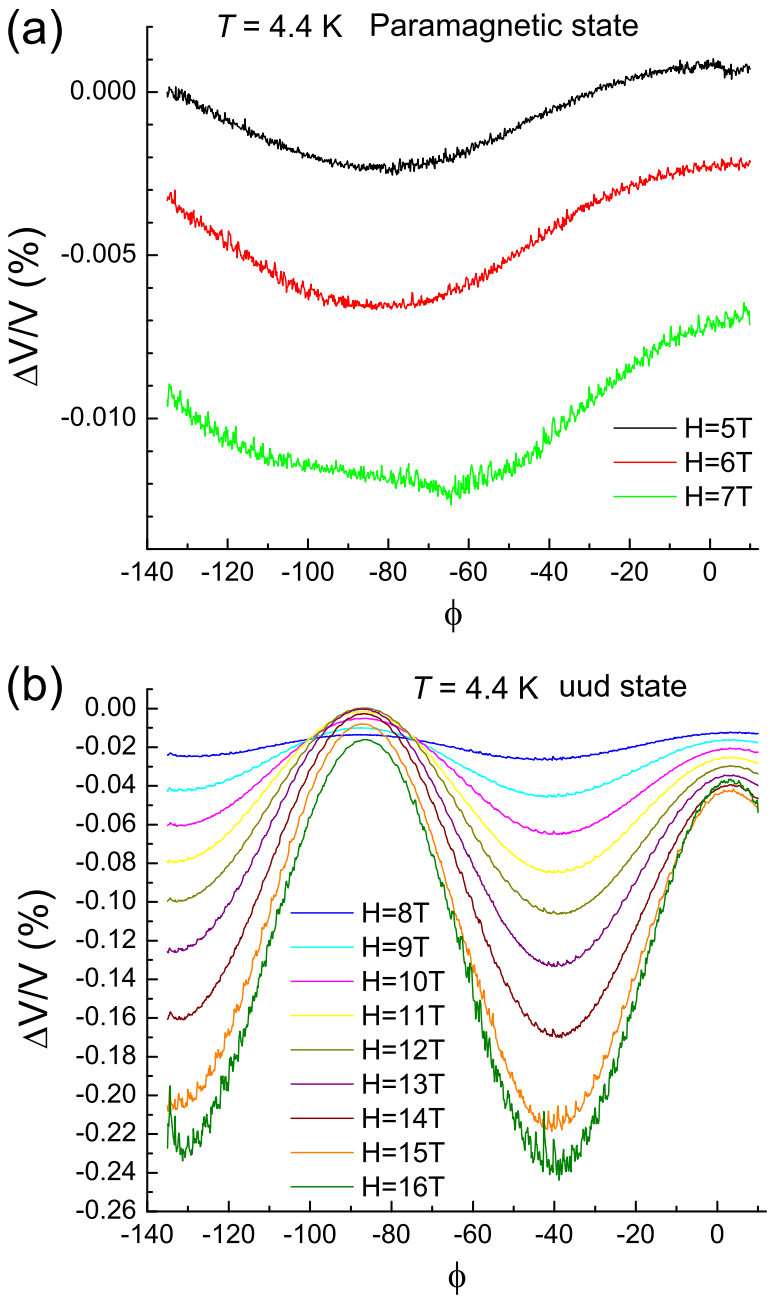

Figure 5.5: Field angular (ϕ) dependence of $v_{L[100]}/v$ for different magnetic field strengths in the basal plane of $Ba_3CoSb_2O_9$, with 0° corresponding to $\mathbf{H} \parallel a$-axis at 4.4 K; (a), (b) show the curves obtained in paramagnetic and uud states, respectively.

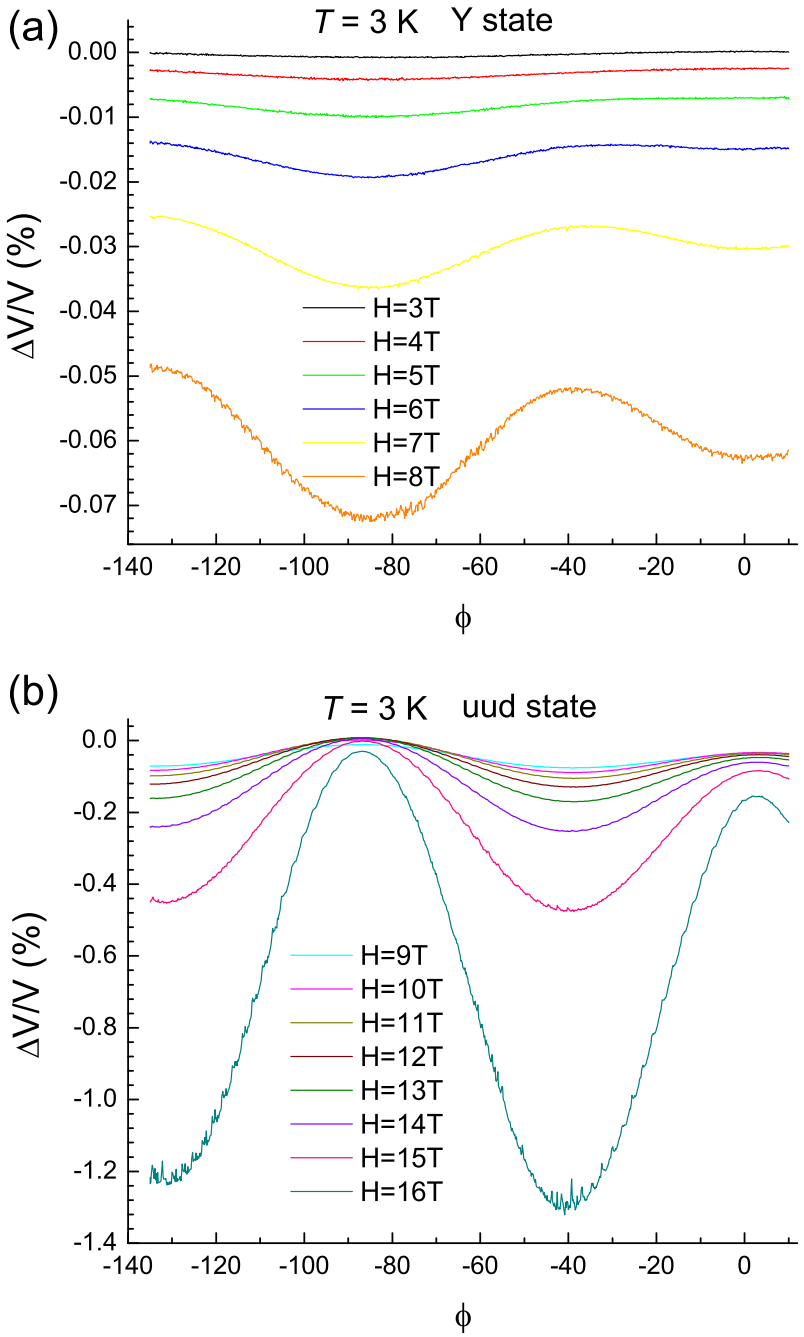

Figure 5.6: Field angular (ϕ) dependence of $v_{L[100]}/v$ for different magnetic field strengths in the basal plane of $Ba_3CoSb_2O_9$, with 0° corresponding to $\mathbf{H} \parallel a$-axis at $T = 3$ K; (a), (b) show the curves obtained in Y and uud states, respectively.

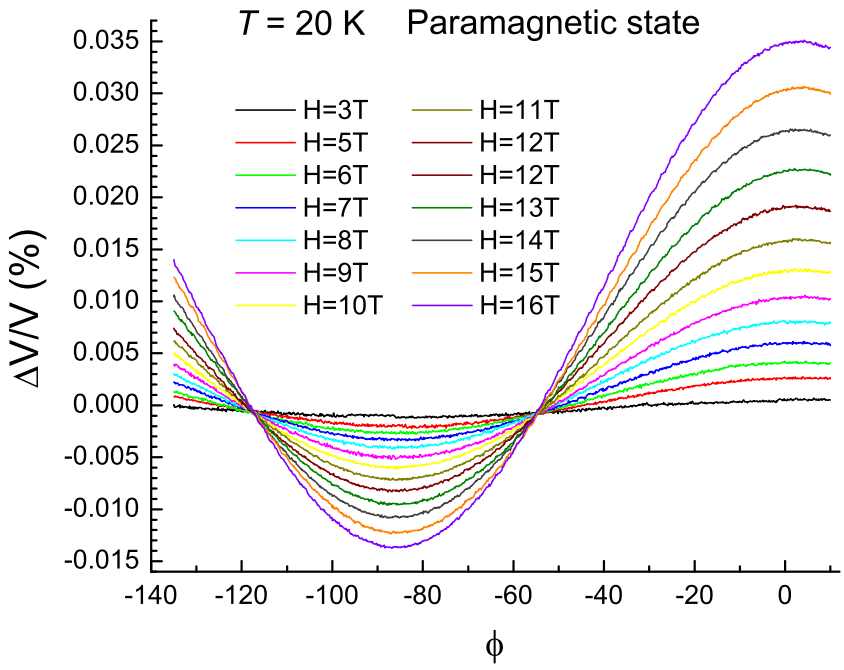

Figure 5.7: Field angular (ϕ) dependence of $v_{L[100]}/v$ for different magnetic field strengths in the basal plane of $Ba_3CoSb_2O_9$, with 0° corresponding to $\mathbf{H} \parallel a$-axis; The curves are obtained in paramagnetic state at 20 K.

Chapter 6

Mean-field model for magnetoelastic coupling

6.1 Total free energy

In order to analyze the experimental data in Section 5.3, a nonlocal Landau free energy approach [82, 83] with magnetoelastic couplings is used. This approach is useful as it links the sound velocity directly to the sample magnetization and the antiferromagnetic spin modulations, which are known in general. In that context, the total free energy is written as

$$F = F_s + F_{el} + F_{se}, \tag{6.1}$$

where F_s and F_{el} are the energy associated with the local spin density $\mathbf{s}(\mathbf{r}_i)$ and the elastic energy, while F_{se} represents the linear-quadratic coupling energy (lowest-order coupling invariants) between the strain components e_α (Voigt notation) and $\mathbf{s}_\alpha(\mathbf{r}_i)$. Higher-order terms at sixth order that would involve in-plane triangular anisotropy

are omitted from the present analysis as they appear to be unnecessary to explain the main features of the experimental results. Due to the quasi-2D character of $Ba_3CoSb_2O_9$ [6] with an easy-plane anisotropy [6], only the energy within the plane which includes the nearest neighbor exchange energy J, the elastic energy, and the magnetoelastic energy are considered, with the spins being confined to the ab plane due to the large exchange anisotropy $J_c/J = 0.026$ [6].

6.2 Elastic energy of $Ba_3CoSb_2O_9$

According to the Hooke's law, the crystalline elastic potential energy [103] is

$$F_{el} = \frac{1}{2} C_{ijkl} e_{ij} e_{kl}, \tag{6.2}$$

where C_{ijkl} are the bare elastic constants and e_{ij} are the strain components, with $i, j, k, l = x, y, z$ corresponding to the three orthogonal directions of a Cartesian coordinate system. Using the Voigt notation, the elastic tensor can be simplified as a 6×6 tensor through the transformation

$$\begin{array}{ccc} (11) \leftrightarrow 1 & (22) \leftrightarrow 2 & (33) \leftrightarrow 3 \\ (23) = (32) \leftrightarrow 4 & (13) = (31) \leftrightarrow 5 & (12) = (21) \leftrightarrow 6. \end{array}$$

Then the elastic potential energy can be written as

$$F_{el} = \frac{1}{2} C_{\alpha\beta} e_{\alpha} e_{\beta}, \tag{6.3}$$

where $\alpha, \beta = 1, 2, ...6$ and $C_{\alpha\beta} = C_{\beta\alpha}$ [103]. For the hexagonal symmetry, the elastic tensor must remain invariant under the symmetry operation I, C_y^2, C_z^2, C_z^3, where

$$I = \begin{pmatrix} -1 & 0 & 0 \\ 0 & -1 & 0 \\ 0 & 0 & -1 \end{pmatrix}, \qquad C_y^2 = \begin{pmatrix} -1 & 0 & 0 \\ 0 & 1 & 0 \\ 0 & 0 & -1 \end{pmatrix},$$
$$C_z^3 = \begin{pmatrix} -\frac{1}{2} & -\frac{\sqrt{3}}{2} & 0 \\ \frac{\sqrt{3}}{2} & -\frac{1}{2} & 0 \\ 0 & 0 & 1 \end{pmatrix}, \qquad C_z^2 = \begin{pmatrix} -1 & 0 & 0 \\ 0 & 1 & 0 \\ 0 & 0 & 1 \end{pmatrix}, \tag{6.4}$$

and therefore reduces to [103]

$$C = \begin{pmatrix} C_{11} & C_{12} & C_{13} & 0 & 0 & 0 \\ C_{12} & C_{11} & C_{13} & 0 & 0 & 0 \\ C_{13} & C_{13} & C_{33} & 0 & 0 & 0 \\ 0 & 0 & 0 & C_{44} & 0 & 0 \\ 0 & 0 & 0 & 0 & C_{44} & 0 \\ 0 & 0 & 0 & 0 & 0 & \frac{C_{11}-C_{12}}{2} \end{pmatrix}. \tag{6.5}$$

As only the elastic coupling in the basal plane of $Ba_3CoSb_2O_9$ is taken into consideration, the 2D elastic potential energy is determined as

$$F_{el} = \frac{1}{2}C_{11}(e_1 + e_2)^2 + \frac{1}{2}C_{66}(e_6^2 - 4e_1e_2), \tag{6.6}$$

where $C_{66} = \frac{C_{11}-C_{12}}{2}$.

6.3 Linear-quadratic magnetoelastic coupling energy of $Ba_3CoSb_2O_9$

The free energy of the linear-quadratic magnetoelastic coupling per unit cell of volume V with nearest-neighbor interaction is written as

$$F_{se} = \frac{1}{2V}\int d\mathbf{r_1} d\mathbf{r_2} K_{ijkl}(\mathbf{r_1}, \mathbf{r_2}) e_{ij} s_k(\mathbf{r_1}) s_l(\mathbf{r_2}), \tag{6.7}$$

where the coefficient K_{ijkl} depends on the spin separation $\tau_{ij} = \mathbf{r}_i - \mathbf{r}_j$. Integrating Eq. 6.7 and using the Voigt notation, we obtain

$$\begin{aligned} F_s &= F_{me} + F_{Se}, \\ F_{me} &= g^2 K^{(m)}_{\alpha\beta} e_\alpha \mathcal{M}_\beta, \\ F_{Se} &= K^{(S)}_{\alpha\beta} e_\alpha \mathcal{S}_\beta, \end{aligned} \tag{6.8}$$

where F_{me} and F_{Se} are associated with the uniform magnetization ($\mathbf{m}$) and the antiferromagnetic modulation ($\mathbf{S}$), respectively. The magnetization tensor $\mathcal{M}_\beta$ and the spin polarization tensor $\mathcal{S}_\beta$ are expressed in the Voigt notation as

$$\begin{aligned} \mathcal{M}_\beta = \{&m_x^2, m_y^2, m_z^2, 2m_y m_z, 2m_z m_x, 2m_x m_y\}, \\ \mathcal{S}_\beta = \{&S_x S_x^*, S_y S_y^*, S_z S_z^*, \frac{1}{2}(S_y S_z^* + S_y^* S_z), \\ &\frac{1}{2}(S_z S_x^* + S_z^* S_x), \frac{1}{2}(S_x S_y^* + S_x^* S_y)\}. \end{aligned} \tag{6.9}$$

For the hexagonal symmetry, the coefficients matrices $K_{\alpha\beta}^{(m/S)}$ must remain invariant under the symmetry operation I, C_y^2, C_z^2, C_z^3 (see Eqs. 6.4), and therefore reduce to

$$K^{(m/S)} = \begin{pmatrix} K_{11}^{(m/S)} & K_{12}^{(m/S)} & K_{13}^{(m/S)} & 0 & 0 & 0 \\ K_{12}^{(m/S)} & K_{11}^{(m/S)} & K_{13}^{(m/S)} & 0 & 0 & 0 \\ K_{31}^{(m/S)} & K_{31}^{(m/S)} & K_{33}^{(m/S)} & 0 & 0 & 0 \\ 0 & 0 & 0 & K_{44}^{(m/S)} & 0 & 0 \\ 0 & 0 & 0 & 0 & K_{44}^{(m/S)} & 0 \\ 0 & 0 & 0 & 0 & 0 & \frac{K_{11}^{(m/S)} - K_{12}^{(m/S)}}{2} \end{pmatrix}. \quad (6.10)$$

In this work, only the in-plane magnetoelastic coupling of $Ba_3CoSb_2O_9$ is taken into consideration, therefore F_{me} and F_{Se} are obtained as

$$\begin{aligned} F_{me} &= g^2 m^2 K_+^{(m)}(e_1 + e_2) + g^2 m^2 K_-^{(m)}\big[(e_1 - e_2)\cos(2\phi) + e_6 \sin(2\phi)\big], \\ F_{Se} &= S^2 K_+^{(S)}(e_1 + e_2) + S^2 K_-^{(S)} \cos(2\beta) \\ &\quad \times (e_1 - e_2)\big[\cos(2\theta)\cos(2\phi) - \sin(2\theta)\sin(2\phi)\big] \\ &\quad + S^2 K_-^{(S)} \cos(2\beta) e_6 \big[\sin 2\theta \cos(2\phi) + \cos(2\theta)\sin(2\phi)\big], \end{aligned} \quad (6.11)$$

where

$$K_\pm^{(m/S)} = \frac{1}{2}\big(K_{11}^{(m/S)} \pm K_{12}^{(m/S)}\big). \quad (6.12)$$

Chapter 7

Analysis of the experimental results

7.1 Effective elastic constant with magnetoelastic coupling

With the total free energy in Chapter 6, we can determine the angular dependence of the elastic constant $C^*_{\alpha\beta}(\phi)$ using [83]

$$C^*_{\alpha\beta}(\phi) = \frac{\partial^2 F}{\partial e_\alpha \partial e_\beta} - \chi_m \frac{\partial^2 F}{\partial e_\alpha \partial \mathcal{M}_\beta} \frac{\partial^2 F}{\partial \mathcal{M}_\alpha \partial e_\beta} - \chi_S \frac{\partial^2 F}{\partial e_\alpha \partial \mathcal{S}_\beta} \frac{\partial^2 F}{\partial \mathcal{S}_\alpha \partial e_\beta}, \tag{7.1}$$

where χ_m and χ_S are given by

$$\chi_m = \left(\frac{\partial^2 F}{\partial m^2}\right)^{-1}, \quad \chi_S = \left(\frac{\partial^2 F}{\partial S^2}\right)^{-1}, \tag{7.2}$$

which represent the uniform magnetic and the antiferromagnetic spin polarization susceptibilities, respectively. In Eq. 7.1, the tensor elements associated with the first term correspond to those given in Eq. 6.5, while the matrices of the second and third term for the Y and uud states ($\theta = 0$) are

$$
\begin{aligned}
&-\chi_m \frac{\partial^2 F}{\partial e_\alpha \partial \mathcal{M}_\beta} \frac{\partial^2 F}{\partial \mathcal{M}_\alpha \partial e_\beta} \\
&= \begin{pmatrix}
-4g^4\chi_m \left[K_+^{(m)} + K_-^{(m)} \cos(2\phi)\right]^2 m^2 & & & \\
2g^4\chi_m \left[K_-^{(m)^2} - 2K_+^{(m)^2} + K_-^{(m)^2} \cos(4\phi)\right] m^2 & \cdot & \cdot & \cdot \\
& \cdot & & \\
& \cdot & & \\
& \cdot & &
\end{pmatrix},
\end{aligned}
\tag{7.3}
$$

$$
\begin{aligned}
&-\chi_S \frac{\partial^2 F}{\partial e_\alpha \partial \mathcal{S}_\beta} \frac{\partial^2 F}{\partial \mathcal{S}_\alpha \partial e_\beta} \\
&= \begin{pmatrix}
-4\chi_S \left[K_+^{(S)} + K_-^{(S)} \cos(2\beta)\cos(2\phi)\right]^2 S^2 & & & \\
\chi_S \left[\big(1+\cos(4\beta)\big)\big(1+\cos(4\phi)\big) K_-^{(S)^2} - 4K_+^{(S)^2}\right] S^2 & \cdot & \cdot & \cdot \\
& \cdot & & \\
& \cdot & & \\
& \cdot & &
\end{pmatrix}.
\end{aligned}
$$

For a hexagonal crystal structure, the velocity of longitudinal modes propagating along the a-axis is given by $V_{L[100]} = \sqrt{C_{11}/\rho}$, where ρ is the mass density, and the relative velocity variation as a function of ϕ can be approximated using

$$
\begin{aligned}
\frac{\Delta V_{L[100]}}{V_{L[100]}} &\simeq \frac{\Delta C_{11}^*(\phi)}{2C_{11}} \simeq \frac{C_{11}^*(\phi) - C_{11}^*(0)}{2C_{11}}, \\
&= A\sin^2(\phi) + B\sin^2(\phi)\cos^2(\phi),
\end{aligned}
\tag{7.4}
$$

where, for the Y and plateau states, the angular magnetoelastic coefficients A and B correspond to

$$\begin{aligned} A =& \frac{8g^4 K_+^{(m)} K_-^{(m)}}{C_{11}} \chi_m m^2 + \frac{8K_+^{(S)} K_-^{(S)}}{C_{11}} \cos(2\beta)\chi_S S^2, \\ B =& \frac{8g^4 {K_-^{(m)}}^2}{C_{11}} \chi_m m^2 + \frac{8{K_-^{(S)}}^2}{C_{11}} \cos^2(2\beta)\chi_S S^2. \end{aligned} \tag{7.5}$$

Inspection of Eq. 7.4 immediately reveals that the 180° period is determined by A while B is responsible for a 90° modulation. All experimental data have been fitted using Eq. 7.4 in terms of the adjustable parameters A and B, as present in Fig. 7.1, where we show one experimental curve per magnetic state for clarity. We conclude that the analytical solution Eq. 7.4 (continuous red lines) accounts very well for the observed angular dependence at all temperatures and fields. The values of A and B are then used to evaluate the magnetoelastic coupling constants $K_\pm^{(m/S)}$ which determine the spin induced lattice distortions (strains).

In order to obtain the analytical solution for the strains, we minimize Eq. 6.1 with respect to e_α to have the equations

$$\begin{aligned} \frac{\partial F}{\partial e_1} &= C_{11}(e_1 + e_2) - 2C_{66}e_2 + g^2 K_+^{(m)} m^2 + K_+^{(S)} S^2 \\ &\quad + \left(g^2 K_-^{(m)} m^2 + K_-^{(S)} S^2 \cos(2\beta)\right) \cos(2\phi) = 0, \\ \frac{\partial F}{\partial e_2} &= C_{11}(e_1 + e_2) - 2C_{66}e_1 + g^2 K_+^{(m)} m^2 + K_+^{(S)} S^2 \\ &\quad - \left(g^2 K_-^{(m)} m^2 + K_-^{(S)} S^2 \cos(2\beta)\right) \cos(2\phi) = 0, \\ \frac{\partial F}{\partial e_6} &= C_{66}e_6 + \left(g^2 K_-^{(m)} m^2 + K_-^{(S)} S^2 \cos(2\beta)\right) \sin(2\phi) = 0. \end{aligned} \tag{7.6}$$

Solving Eqs. 7.6, we obtain

$$\begin{aligned} e_1 + e_2 &= \frac{g^2 K_+^{(m)} m^2 + K_+^{(S)} S^2}{C_{66} - C_{11}}, \\ e_1 - e_2 &= -\frac{g^2 K_-^{(m)} m^2 + K_-^{(S)} S^2 \cos(2\beta)}{C_{66}} \cos(2\phi), \\ e_6 &= -\frac{g^2 K_-^{(m)} m^2 + K_-^{(S)} S^2 \cos(2\beta)}{C_{66}} \sin(2\phi). \end{aligned} \tag{7.7}$$

Here, the isotropic term $e_1 + e_2$ corresponds to the relative area variation of the basal plane due to the uniform magnetization $\mathbf{m}$ and the antiferromagnetic modulation $\mathbf{S}$. However, $e_1 - e_2$ and e_6 correspond to longitudinal and shear distortions leading to a reduction of the crystal symmetry as the magnetic field is rotated away from the direction of propagation of the acoustic wave ($\hat{\mathbf{x}}(\phi = 0) \parallel a$-axis). These solutions also indicate that the lattice distortions ($e_1 - e_2$ and e_6) are exclusively related to the magnetoelastic coupling coefficients $K_-^{(m/S)}$. In other words, the magnitude of B provides information regarding the significance of the spin-induced distortions in the triangular lattice antiferromagnets such as $Ba_3CoSb_2O_9$.

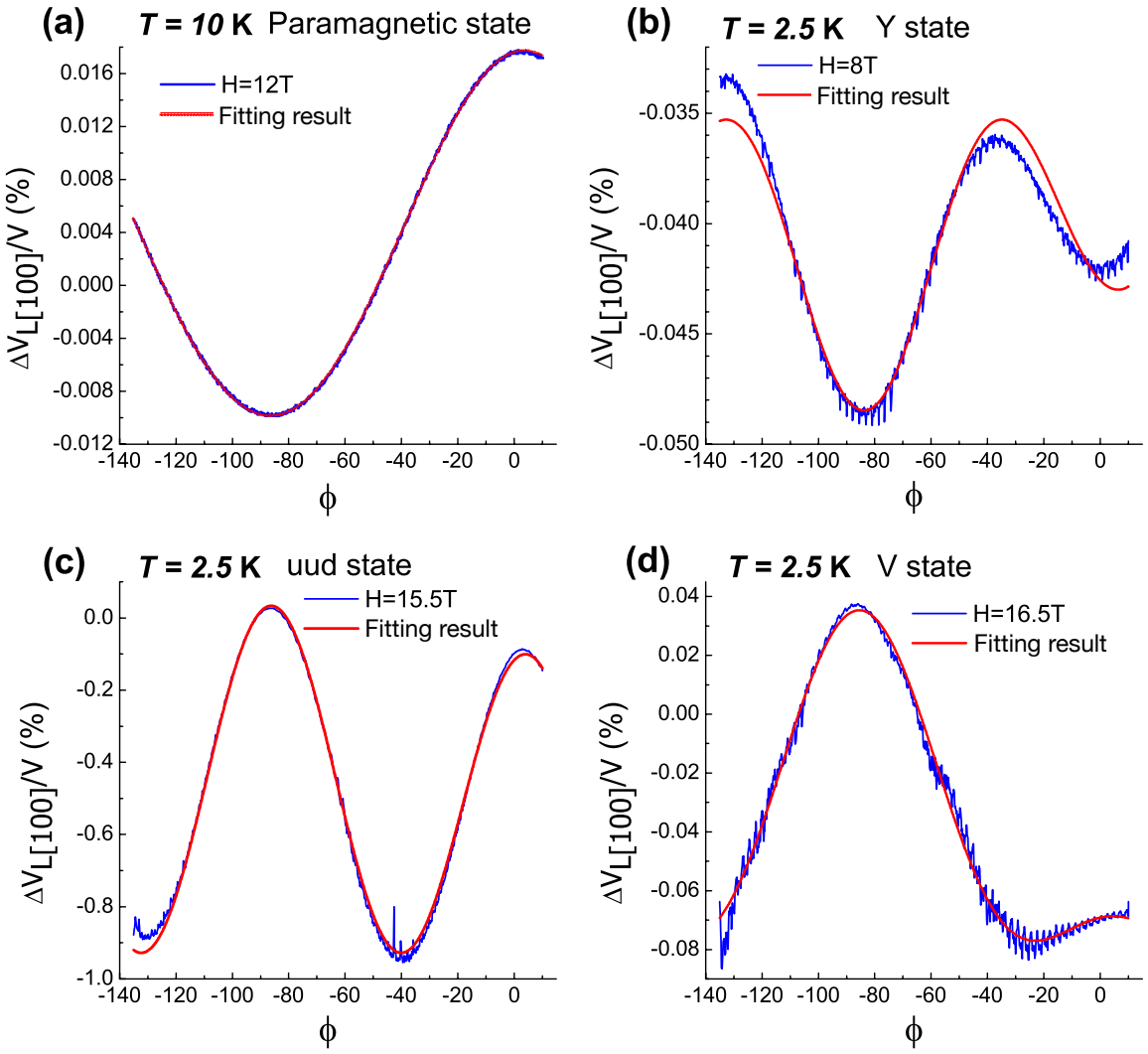

Figure 7.1: The red curves illustrate typical fits of $\Delta v_{L[100]}/v$ using Eq. 7.4 for the data obtained in the paramagnetic state and the different ordered states. Reprinted with permission from [M. Li, A. Zelenskiy, J. A. Quilliam, Z. L. Dun, H. D. Zhou, M. L. Plumer, and G. Quirion, Phys. Rev. B, 99:094408, 2019]. Copyright (2019) by American Physical Society.

7.2 Data analysis for paramagnetic state

We analyze the results by fitting the experimental curves obtained in the paramagnetic state at 10 K (see Fig. 5.3(a)) using Eq. 7.4, and show the values of the parameters A and B in Table 7.1. Considering that for the paramagnetic state the A and B coefficients (Eqs. 7.5) depends uniquely on the magnetization, $\mathbf{m} = \chi_m \mathbf{H}$, we obtain that A and B are linear functions of H^2:

$$\begin{aligned} A &= \frac{8K_+^{(m)}K_-^{(m)}}{C_{11}}\chi_m^3 H^2 = k_A H^2, \\ B &= \frac{8{K_-^{(m)}}^2}{C_{11}}\chi_m^3 H^2 = k_B H^2, \end{aligned} \tag{7.8}$$

where $k_A = -(1.911 \pm 0.001) \times 10^{-6}$ T^{-2} and $k_B = -(2.2 \pm 0.1) \times 10^{-7}$ T^{-2} are the slopes of the fitted lines presented in Fig. 7.2. Furthermore, using the Eqs. 7.8 with $\chi_m = 6.5 \times 10^{-2}(\mu_B/T)/Co^{2+}$ [65], $C_{11} = (17.3 \pm 0.4) \times 10^{10}$ N/m^2 and $C_{66} = (5.3 \pm 0.1) \times 10^{10}$ N/m^2 [9], we obtain the absolute values of magnetoelastic coupling constants $|K_+^{(m)}| = (51 \pm 1) \times 10^4$ N/m^2 and $|K_-^{(m)}| = (5.9 \pm 0.2) \times 10^4$ N/m^2. Consequently, we can estimate the field induced deformations using Eqs. 7.7 with these values. The magnitude of the deformations for $Ba_3CoSb_2O_9$, shown in Table 7.2, are comparable to magnetostriction data obtained for other triangular antiferromagnets such as $CsNiCl_3$ and $RbNiCl_3$ [104].

H(T)	5	7	9	10	11	12
$A(\times 10^{-4})$	-0.476	-0.933	-1.54	-1.91	-2.31	-2.75
$B(\times 10^{-5})$	0.088	-0.23	-0.96	-1.23	-1.87	-2.48

Table 7.1: Values of the parameters A and B are determined in the paramagnetic phase at 10 K.

$T = 10$ K	$H = 3$ T	$H = 8$ T
$\lvert e_1 - e_2 \rvert$	$\sim 6.2 \times 10^{-7}$	$\sim 4.4 \times 10^{-6}$
$\lvert e_1 + e_2 \rvert$	$\sim 2.5 \times 10^{-6}$	$\sim 1.7 \times 10^{-5}$

Table 7.2: Values of magnetostriction effects induced by the magnetic field aligned in the basal plane for $Ba_3CoSb_2O_9$ in paramagnetic state at $T = 10$ K.

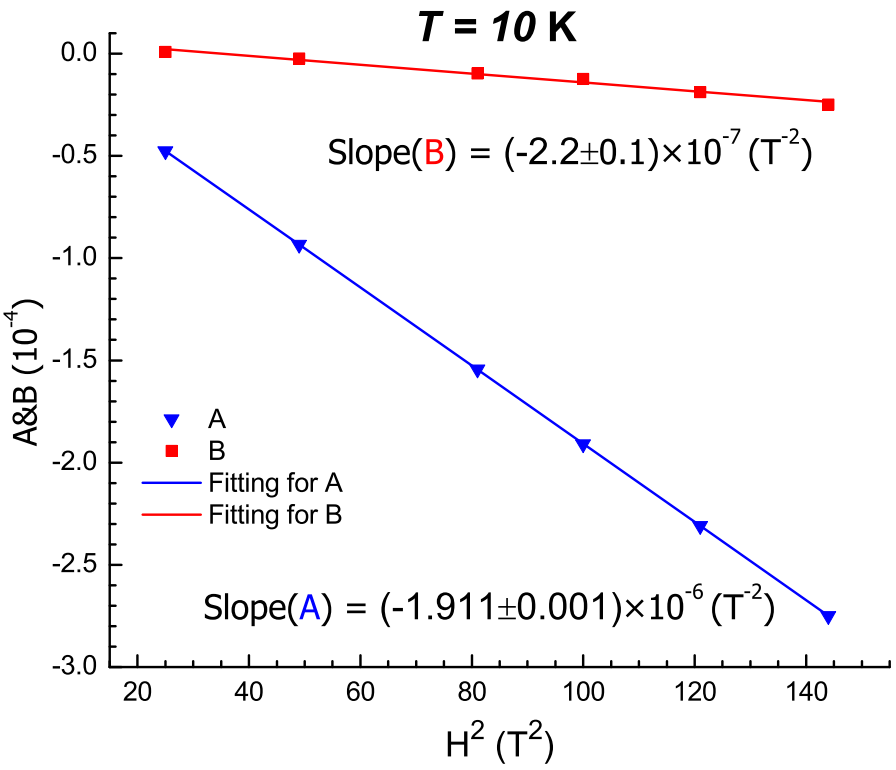

Figure 7.2: The blue triangles and red squares represent the field dependence of parameters A and B determined in the paramagnetic phase (10 K) and fitted using Eq. 7.4 (continuous lines). Reprinted with permission from [M. Li, A. Zelenskiy, J. A. Quilliam, Z. L. Dun, H. D. Zhou, M. L. Plumer, and G. Quirion, Phys. Rev. B, 99:094408, 2019]. Copyright (2019) by American Physical Society.

7.3 Data analysis for the ordered states

In Table 7.3, we show the values of the A and B coefficients determined by fitting the experimental curves using Eq. 7.4 in the different magnetically ordered states (see Fig. 5.3(b), (c),(d)) at 2.5 K. These values are compared to results obtained in the paramagnetic state at 10 K as shown in Fig. 7.3. The enhanced values of B in the ordered states suggest that the lattice distortions are mainly associated with the antiferromagnetic spin modulation S. Within the framework of the mean-field model presented in Section 7.1 (Eq. 7.5), considering that there is no microscopic model for χ_S, we simply use that $\chi_S = (\partial^2 F/\partial S^2)^{-1}$ for the evaluation of the magnetoelastic coupling coefficient $K_-^{(S)}$ presented in Fig. 7.4. What is unexpected regarding the field dependence of $K_-^{(S)}$ is that its value increases the most in the plateau state and suddenly drops in the V state. This tendency goes against the mean-field numerical predictions as m, S, and β are found to be field independent in the plateau phase. Since all static thermodynamic variables are constant in the plateau state, we can only account for the observed field dependence of $K_-^{(S)}$ by considering the possible contribution of spin fluctuations. So far we assume that the sound velocity measurements, presented in Fig.5.3, are only affected by a mean-field coupling term such as $\langle \mathbf{S}_i \rangle \cdot \langle \mathbf{S}_j \rangle$. However, there exist numerous experimental results that the sound velocity in magnetic systems is also sensitive to spin fluctuations. For example, at the approach of a magnetic state, the velocity generally decreases due to precursor effects associated with spin fluctuations. In that case, the results of $K_-^{(S)}$ presented in Fig.7.4 could then reflect the field dependence of the spin fluctuations via the dynamic coupling term $\langle \mathbf{S}_i \cdot \mathbf{S}_j \rangle$.

While the observed magnetoelastic coupling in $Ba_3CoSb_2O_9$ is large in comparison

H(T) (Y state)	3	4	5	6	7	8
$A(\times 10^{-5})$	-0.97	-1.5	-3.1	-3.9	-4.6	-5.5
$B(\times 10^{-4})$	0.014	0.12	0.33	1.2	2.5	4.1

H(T) (uud state)	9	10	11	12	13	14	14.5	15	15.5
$A(\times 10^{-4})$	2.2	3.8	4.4	5.0	5.8	7.2	8.2	9.8	13.4
$B(\times 10^{-2})$	-0.16	-0.28	-0.35	-0.44	-0.60	-0.94	-1.3	-2.0	-3.6

H(T) (V state)	16.5
$A(\times 10^{-3})$	1.0
$B(\times 10^{-3})$	-0.18

Table 7.3: Values of the parameters A and B are determined in the Y, uud and V phases at 2.5 K.

to other triangular lattice antiferromagnets, it is still too weak in order to fully account for the observed magnetization plateau width. Based on our numerical analysis, the magnetoelastic mechanism would lead to a plateau width of 0.1 T in comparison with the experimental value of 6 T. We estimate that lattice distortions of the order of $e_1 - e_2 \sim 10^{-3}$ would be required in order to account for the full width of the magnetization plateau in $Ba_3CoSb_2O_9$. To our knowledge, no such large distortions have been observed in $Ba_3CoSb_2O_9$. While we can probably rule out that the magnetization plateau is stabilized by magnetoelastic coupling in the case of $Ba_3CoSb_2O_9$, we attribute the field dependence of the magnetoelastic coefficient $K_{-}^{(S)}$ (Fig. 7.4) to

the effect of spin fluctuations increasing in order to induce and stabilize the magnetization plateau. Another remarkable observation is that our results indicate that these fluctuations are suddenly suppressed or reduced as the V phase is stabilized at higher fields. Thus, to fully account for the experimental results presented in contribution, models including magnetoelastic couplings influenced by spin fluctuations are clearly required. Moreover, as shown by recent experimental work on spin fluctuations on $Ba_3CoSb_2O_9$ [66, 105, 106], new theoretical approaches are needed to describe the dynamic magnetic properties of low-dimensional frustrated magnets.

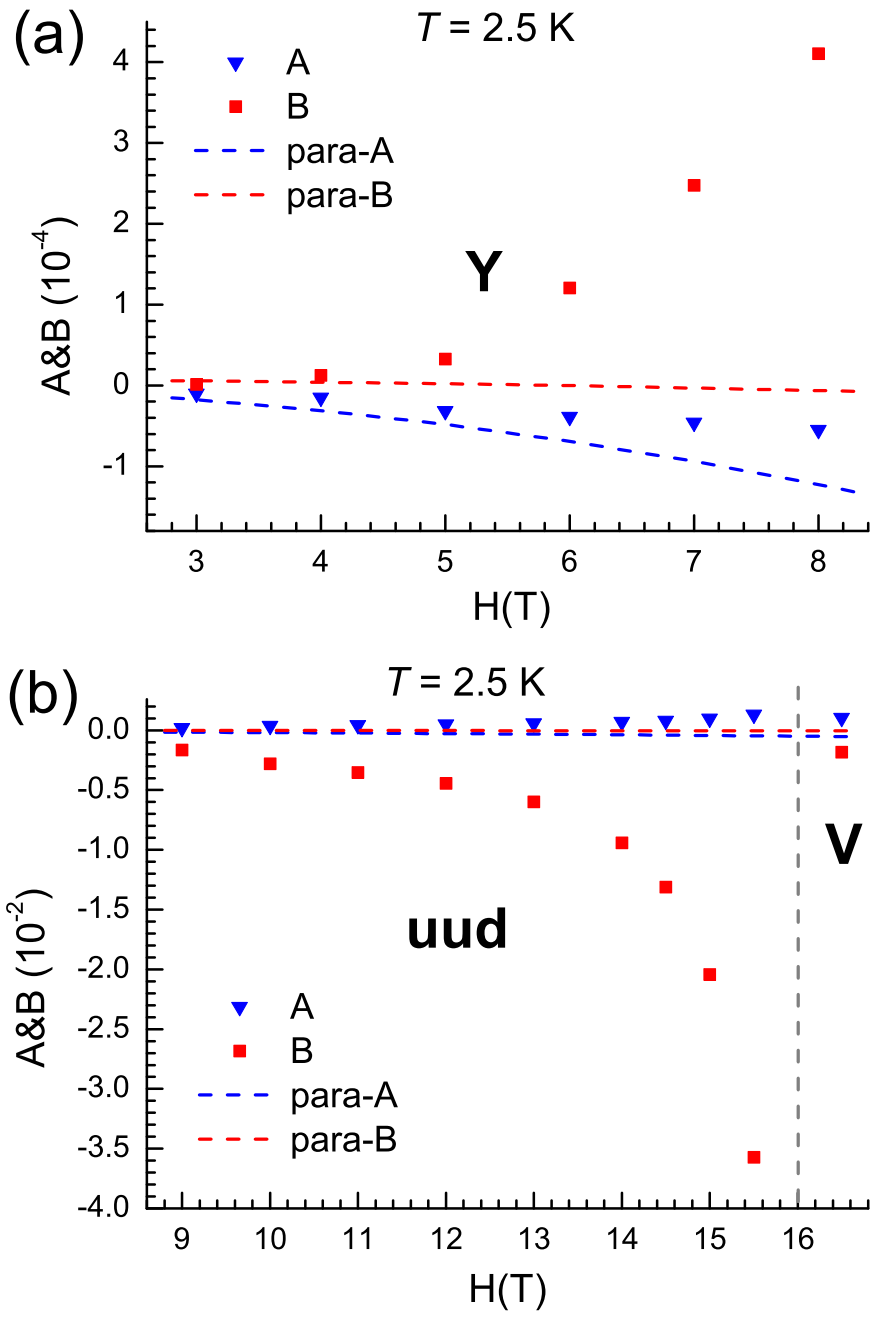

Figure 7.3: Angular magnetoelastic coefficients A and B determined at $T = 2.5$ K using Eq. 7.4. The blue triangles and red squares represent the values of A and B in the different ordered states, which are compared with the values determined in the paramagnetic state (the dashed lines).

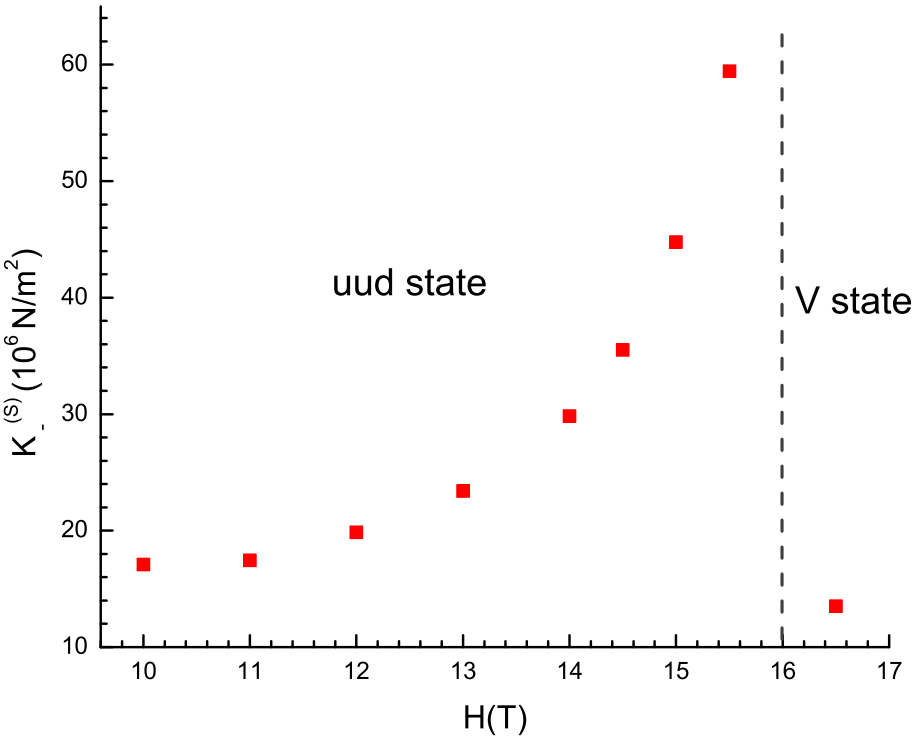

Figure 7.4: Field dependence of the magnetoelastic constant $K_-^{(S)}$ obtained at 2.5 K. Reprinted with permission from [M. Li, A. Zelenskiy, J. A. Quilliam, Z. L. Dun, H. D. Zhou, M. L. Plumer, and G. Quirion, Phys. Rev. B, 99:094408, 2019]. Copyright (2019) by American Physical Society.

7.4 Data analysis for thermal and quantum fluctuations

Since the field dependence of magnetoelastic coupling in $Ba_3CoSb_2O_9$ is influenced significantly by spin fluctuations in ordered states [3], we explore the effect of thermal and quantum fluctuations by measuring the sample at the temperatures shown in Fig. 7.5, 10 K and 20 K. Comparing the results determined at 2.5 K, 3 K and 4.4 K, we can distinguish the contributions of the thermal and quantum fluctuations in Y and uud states. The measured points with medium fields are close to the boundary of uud and paramagnetic state at $T = 5.5$ K, which are used for presenting the short range correlation with effect of spin fluctuations. Furthermore, the results at higher temperatures, $T = 10$ K and 20 K, are shown for the paramagnetic state with strong thermal fluctuations.

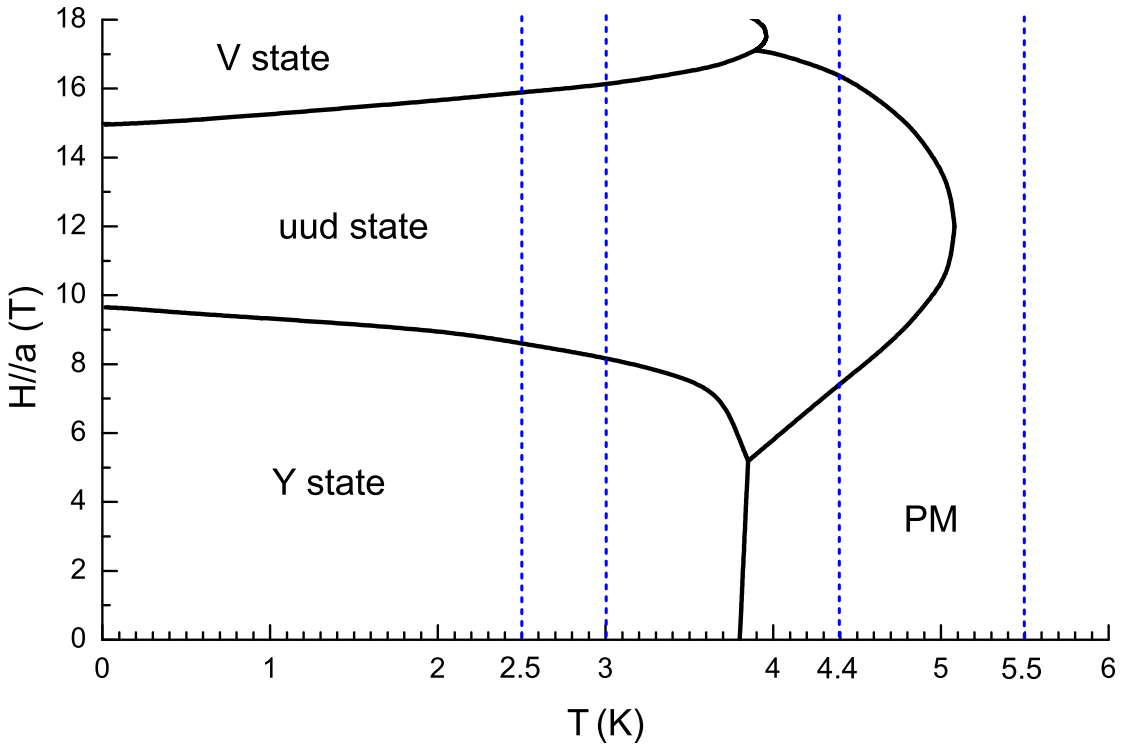

Figure 7.5: The chosen temperatures, 2.5 K, 3 K, 4.4 K and 5.5 K, are shown in the experimental H-T phase diagram of $Ba_3CoSb_2O_9$ obtained by ultrasonic measurements for $\mathbf{H} \parallel a$-axis [9].

7.4.1 Effect of thermal fluctuations at 20 K

We analyze the results obtained in the paramagnetic state at 20 K by fitting the experimental curves shown in Fig. 5.7, and show the values of the parameters A and B in Table 7.4. Considering $\mathbf{m} = \chi_m \mathbf{H}$ in the paramagnetic state, we can fit A and B using Eq. 7.8, and present the fitted lines in Fig. 7.6. The slope of the parameter A, $k_A(T = 20K) = -(1.910 \pm 0.001) \times 10^{-6}$ T^{-2}, is same as the value at 10 K, while $k_B(T = 20K) = -(1.3 \pm 0.6) \times 10^{-8}$ T^{-2} is at least one order of magnitude smaller than the slope of the parameter B at 10 K (see Fig. 7.2). According to Eq. 7.7, compared with the results obtained at 10 K, the parameter B and k_B at 20 K indicate smaller lattice distortion which corresponds to weaker magnetoelastic coupling. Moreover, the neighboring magnetic ions interact very weakly with each other in the paramagnetic state at high temperature due to the strong thermal fluctuations [17]. Therefore, with the decrease of temperature which is related to weaker thermal fluctuations, the short range correlation and the magnetoelastic coupling play more important roles in the system, which account for the increment of the lattice distortion.

H(T)	3	5	6	7	8	9	10
$A(\times 10^{-4})$	-0.16	-0.47	-0.68	-0.93	-1.2	-1.5	-1.9
$B(\times 10^{-6})$	1.0	3.8	2.6	3.6	4.3	3.3	3.8
H(T)	11	12	13	14	15	16	
$A(\times 10^{-4})$	-2.3	-2.7	-3.2	-3.7	-4.3	-4.9	
$B(\times 10^{-6})$	2.7	2.3	3.3	1.8	1.1	-4.3	

Table 7.4: Values of the parameters A and B are determined in the paramagnetic phase at 20 K.

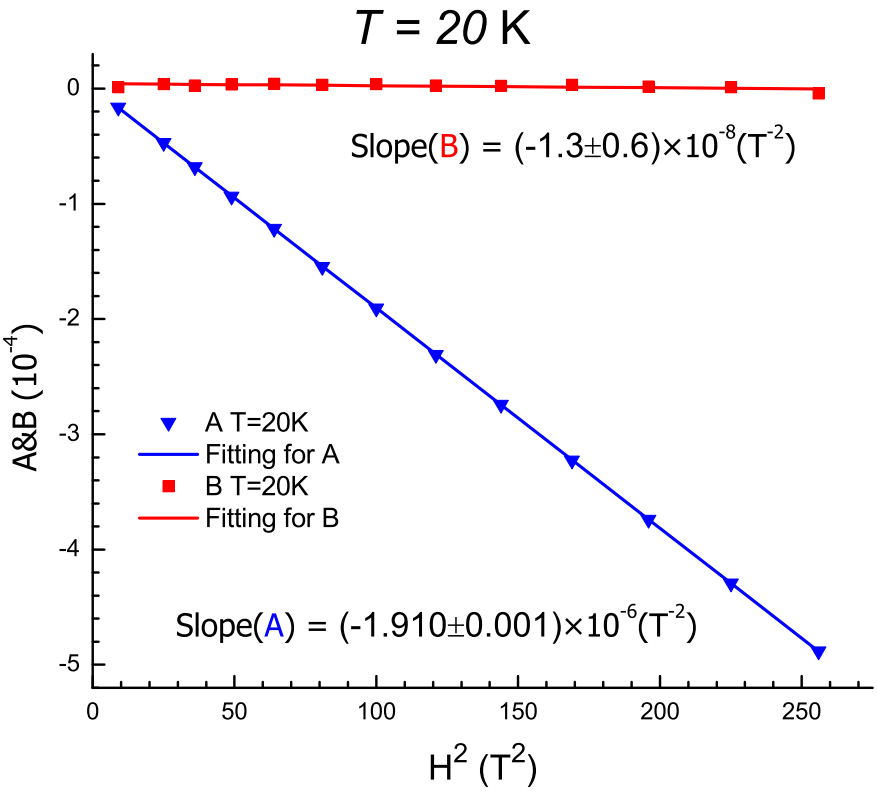

Figure 7.6: The blue triangles and red squares represent the field dependence of parameters A and B determined in the paramagnetic phase (20 K) and fitted using Eq. 7.4 (continuous lines).

7.4.2 Effect of spin fluctuations close to phase boundary

In Table 7.5, we show the values of the coefficients A and B determined by fitting the experimental curves in Fig. 5.4 measured at 5.5 K using Eq. 7.4, and compare these values with the results obtained in the paramagnetic state at 10 K in Fig. 7.7. As shown in Fig. 7.7(a), the values of the parameters A and B with $H < 8$ T are close to the dashed lines obtained at 10 K. When $H > 8$ T, the parameter A deviates from the blue line (A values at 10 K) quickly as shown in Fig. 7.7(b). Moreover, the absolute value of B increases rapidly as the measured points are close to the phase boundary of uud and paramagnetic states, while drops for $H > 15$ T due to the deviation from the phase boundary. Previous theoretical works [5, 107, 108] have proved that the stabilization of the uud state and the increment of T_N at the P→uud phase boundary are mainly accounted for by the entropic order by disorder mechanism which is produced by thermal fluctuations. Our work presents an experimental evidence of the thermal fluctuations through the magnetoelastic coupling. On the other hand, although the system is still in paramagnetic state close to the phase boundary between uud and paramagnetic states, the short range correlation is very important, and the magnetoelastic coupling is influenced intensely by spin fluctuations.

H(T)	3	4	5	6	7	8
$A(\times 10^{-5})$	-1.4	-2.4	-3.8	-5.6	-7.2	-9.0
$B(\times 10^{-5})$	0.18	0.15	0.11	-0.35	-1.4	-3.7

H(T)	9	10	11	12	13	14	15	16
$A(\times 10^{-4})$	-1.1	-1.2	-1.3	-1.4	-1.7	-2.1	-2.7	-3.5
$B(\times 10^{-4})$	-0.87	-1.6	-2.7	-3.9	-4.9	-5.3	-5.4	-5.2

Table 7.5: Values of the parameters A and B are determined in paramagnetic state with the points relatively far from ($H \leq 8$ T and $H \geq 16$ T) and close to (9 T $\leq H \leq$ 15 T) the phase boundary between uud and paramagnetic states at 5.5 K.

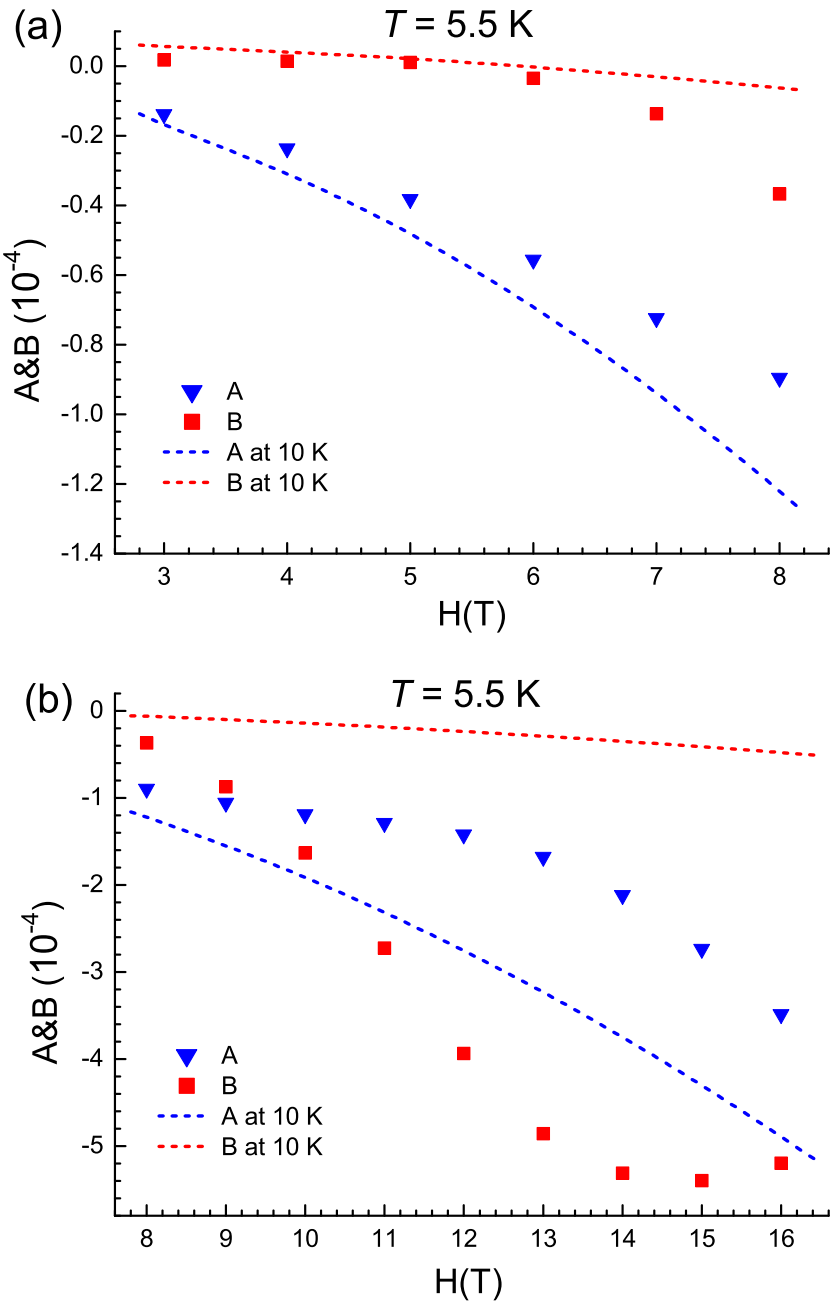

Figure 7.7: Angular magnetoelastic coefficients A and B determined at $T = 5.5$ K using Eq. 7.4. The blue triangles and red squares represent the values of A and B for the paramagnetic state at 5.5 K, which are compared with the values determined in the paramagnetic state at 10 K (the dashed lines).

7.4.3 Effect of quantum fluctuations in ordered states

The values of A and B coefficients, determined by fitting the experimental curves in Fig. 5.5 at 4.4 K and Fig. 5.6 at 3 K using Eq. 7.4, are shown in Table 7.6 and Table 7.7, respectively. As shown in Fig. 7.8(a), the parameters A and B in paramagnetic at T = 4.4 K state with low magnetic field ($H < 7.6$ T) are close to the values obtained at 10 K. In uud state at $T = 4.4$ K as shown in Fig. 7.8(b), the A and B coefficients are of the same order of magnitude as the values obtained in uud state at 2.5 K. While different from the values of parameter B at 2.5 K which increase rapidly closing to the phase boundary of uud and V state, B value at 4.4 K increases slowly closing to the top side of the phase boundary of uud and paramagnetic states. Comparing the fitting results obtained in Y and uud state at $T = 3$ K and 2.5 K shown in Fig. 7.9, we present that the values of the parameters A and B are almost same, except the points very close to the phase boundaries (with $H = 8$ T and 16 T). As a result, also considering the ranges of the Y and uud states are almost not changed with $T < 3$ K (see Fig. 7.5), the magnetoelastic coupling of the Y and uud states is temperature independent between $T = 3$ K and 2.5 K. These results indicate that the thermal fluctuations are still important in the uud state with $T > 3.8$ K, which is consistent with the entropic order by disorder mechanism [5, 107, 108]. In contrast, the effect of the thermal fluctuations on magnetoelastic coupling are negligible in the Y and uud states of $Ba_3CoSb_2O_9$ at low temperature, while the quantum fluctuations are dominant. However, in order to confirm this conclusion, more experimental data, especially for $T < 2.5$ K, is needed.

H(T)(paramagnetic state)	5	6	7
$A(\times 10^{-5})$	-3.2	-4.4	-5.2
$B(\times 10^{-5})$	1.4	1.5	-3.2

H(T)(uud state)	8	9	10	11	12	13	14	15	16
$A(\times 10^{-4})$	-0.078	0.68	1.7	2.5	3.2	3.7	4.1	3.9	2.8
$B(\times 10^{-3})$	-0.51	-1.2	-2.0	-2.8	-3.5	-4.5	-5.8	-7.4	-8.2

Table 7.6: Values of the parameters A and B are determined in paramagnetic state and uud state at 4.4 K.

H(T) (Y state)	3	4	5	6	7	8
$A(\times 10^{-5})$	-0.91	-1.7	-2.8	-4.1	-5.2	-7.9
$B(\times 10^{-4})$	0.024	0.11	0.37	1.1	2.8	6.7

H(T) (uud state)	9	10	11	12	13	14	15	16
$A(\times 10^{-4})$	2.5	3.6	4.3	4.9	5.7	6.9	8.9	14.9
$B(\times 10^{-2})$	-0.20	-0.28	-0.35	-0.44	-0.58	-0.88	-1.7	-4.7

Table 7.7: Values of the parameters A and B are determined in the Y, uud phases at 3 K.

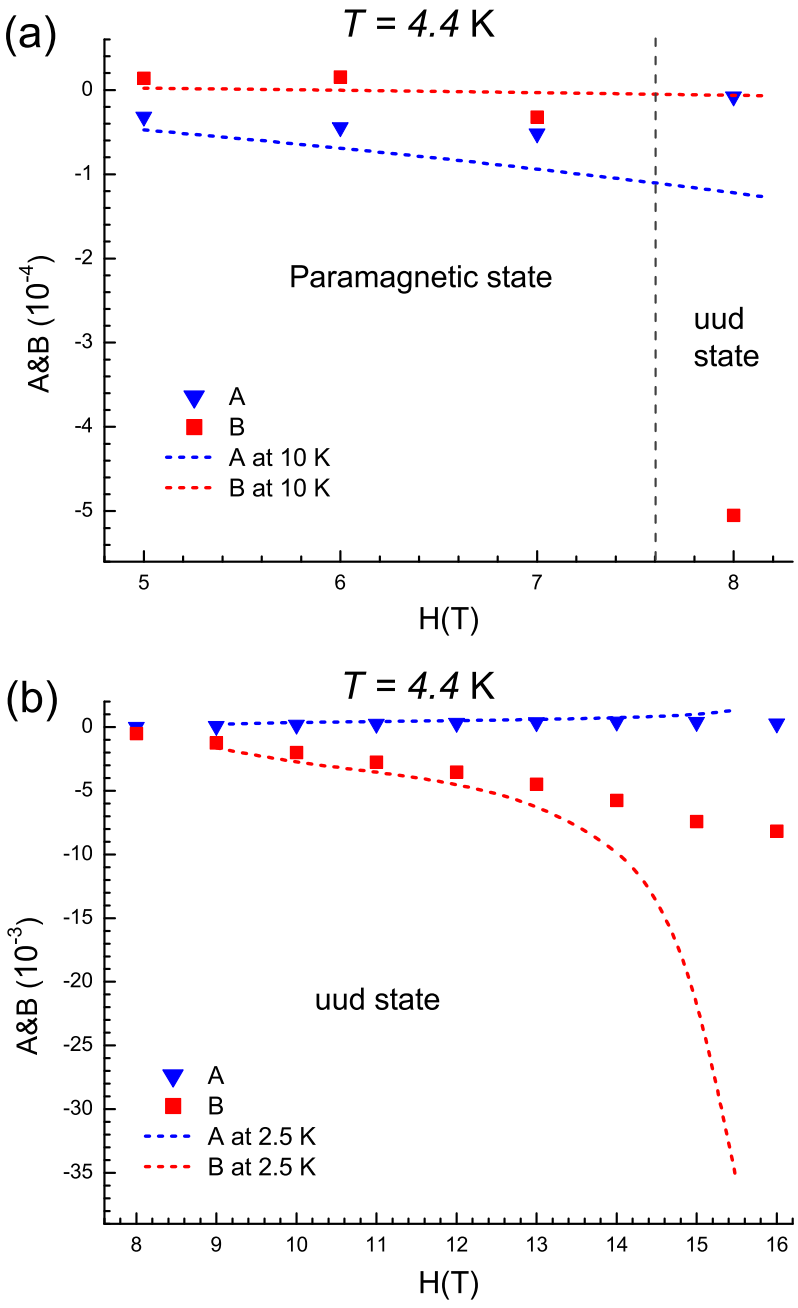

Figure 7.8: Angular magnetoelastic coefficients A and B determined at $T = 4.4$ K using Eq. 7.4. The blue triangles and red squares represent the values of A and B for paramagnetic state and uud states at 4.4 K, which are compared with the values determined in the paramagnetic state at 10 K (a) and the uud state at 2.5 K (b).

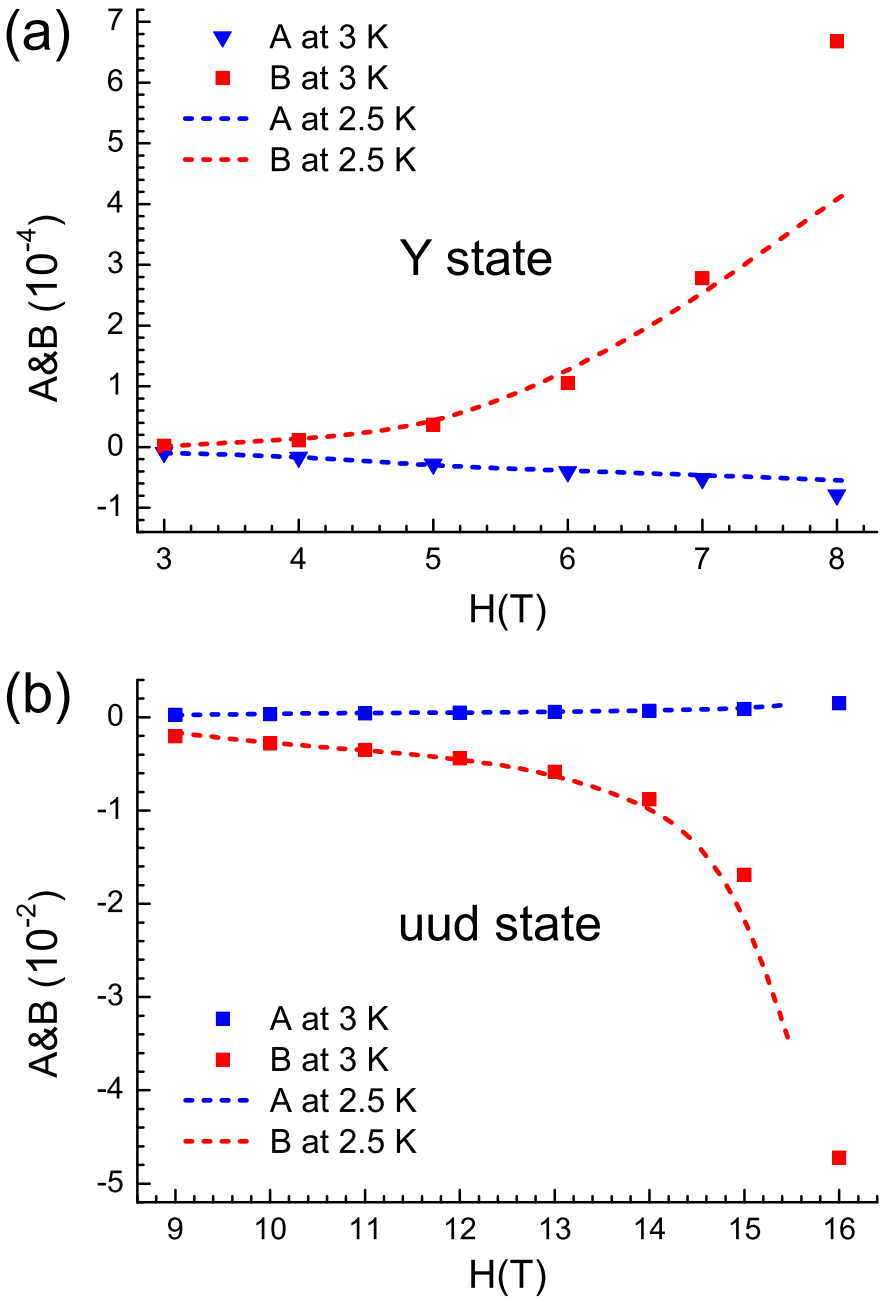

Figure 7.9: Angular magnetoelastic coefficients A and B determined at $T = 3$ K using Eq. 7.4. The blue triangles and red squares represent the values of A and B in Y and uud states, which are compared with the values determined at 2.5K (the dashed lines).

Chapter 8

Summary and conclusion

Due to the interest in the magnetic properties discovered in the quasi-2D frustrated triangular lattice antiferromagnet, we studied $Ba_3CoSb_2O_9$ which has equilateral triangular lattice and easy-plane anisotropy in this project. As the importance of the interlayer interaction has been proved in the experiments on $Ba_3CoSb_2O_9$ [6, 80], the effect of the antiferromagnetic interlayer interaction on the ground states of the layered easy-plane TLAFs is explored using a 3D classical Heisenberg model with bi-quadratic exchange coupling between nearest-neighbour ions within the basal plane. In order to explore the contribution of the spin fluctuations and the magnetoelastic coupling for stabilizing the magnetization plateau, a new method based on ultrasonic measurement is applied on the $Ba_3CoSb_2O_9$ sample.

To study the ground state magnetization processes of realistic quasi-2D TLAFs, we take into consideration in a two-layer classical Heisenberg model the single ion anisotropy ($D = 0.05$), the bi-quadratic exchange coupling (γ = -0.05) for mimicking the the effect of spin fluctuations [2] and the antiferromagnetic interlayer interaction (J_c). For $\mathbf{H} \parallel ab$-plane, the additional state (C state) is obtained with $0 < J_c < 0.14$.

This result is consistent with Ref. [11] and could account for the experimental results of $Ba_3CoSb_2O_9$ with **H** in the *ab*-plane [6,80]. Meanwhile, the magnetization plateau decreases with the increment of J_c and vanishes with $J_c > 0.1$. For larger values of J_c ($J_c > 0.14$), other new states (the W and V$'$ states), not previously reported, are also observed. The spin configurations of the W and V$'$ states show the appearance of small z components due to the interlayer interaction competing with the single ion anisotropy. For $\mathbf{H} \parallel c$-axis, a new state (C_z state) is obtained with $0 < J_c < 0.06$. Moreover, when J_c is large enough, only the state corresponding to the Umbrella phase in the 2D model exits. Furthermore, all ground states of the two-layer model have the same ordering wave vector $\mathbf{Q} = (1/3, 1/3, 1/2)$. We believe that a detailed analysis of relevant experimental results on existing and yet to be discovered TLAFs may benefit from the results present here.

Analyzing the results of the ultrasonic measurement, we conclude that the magnetoelastic coupling in $Ba_3CoSb_2O_9$ is large in comparison to other triangular lattice antiferromagnets, while it is still too weak in order to fully account for the observed magnetization plateau width. In order to account for the full width of the magnetization plateau in $Ba_3CoSb_2O_9$ which is about 6 T, the lattice distortions of the order of $e_1 - e_2 \sim 10^{-3}$ would be required. However, the remarkable observations, that the values of the magnetoelastic coefficient $K_-^{(S)}$ (Fig. 7.4) are large and field dependent in the plateau state while suddenly suppressed or reduced in the V state, indicate that models including magnetoelastic couplings influenced by spin fluctuations are needed. Moreover, comparing the experimental results at 2.5 K, 3 K, 4.4 K, 5.5 K, we explore the effects of the quantum and thermal fluctuations on the magnetoelastic couplings. When the system in paramagnetic state is close to the phase boundary between uud and paramagnetic states, the short range correlation becomes very important, and the magnetoelastic coupling is influenced intensely by spin fluctuations.

The analysis of ordered states at different temperatures indicates that the effect of the thermal fluctuations on magnetoelastic coupling are negligible at low temperature, while the quantum fluctuations are dominant. However, in order to confirm this conclusion, more experimental data, especially for $T < 2.5$ K, is needed. Meanwhile, Monte Carlo simulations with the biquadratic exchange coupling ($\gamma < 0$) would also be useful.

Bibliography

[1] M Li, M L Plumer, and G Quirion. Effects of interlayer and bi-quadratic exchange coupling on layered triangular lattice antiferromagnets. *Journal of Physics: Condensed Matter*, 32(13):135803, Jan 2020.

[2] M E Zhitomirsky. Real-space perturbation theory for frustrated magnets: application to magnetization plateaus. *Journal of Physics: Conference Series*, 592(1):012110, 2015.

[3] M. Li, A. Zelenskiy, J. A. Quilliam, Z. L. Dun, H. D. Zhou, M. L. Plumer, and G. Quirion. Magnetoelastic coupling and the magnetization plateau in $Ba_3CoSb_2O_9$. *Phys. Rev. B*, 99:094408, Mar 2019.

[4] M F Collins and O A Petrenko. Review/synthse: Triangular antiferromagnets. *Canadian Journal of Physics*, 75(9):605–655, 1997.

[5] M V Gvozdikova, P-E Melchy, and M E Zhitomirsky. Magnetic phase diagrams of classical triangular and kagome antiferromagnets. *Journal of Physics: Condensed Matter*, 23(16):164209, 2011.

[6] Takuya Susuki, Nobuyuki Kurita, Takuya Tanaka, Hiroyuki Nojiri, Akira Matsuo, Koichi Kindo, and Hidekazu Tanaka. Magnetization process and collective excitations in the S=1/2 triangular-lattice Heisenberg antiferromagnet

$Ba_3CoSb_2O_9$. *Phys. Rev. Lett.*, 110:267201, Jun 2013.

[7] D J J Farnell, R Zinke, J Schulenburg, and J Richter. High-order coupled cluster method study of frustrated and unfrustrated quantum magnets in external magnetic fields. *Journal of Physics: Condensed Matter*, 21(40):406002, Sep 2009.

[8] Tôru Sakai and Hiroki Nakano. Critical magnetization behavior of the triangular- and kagome-lattice quantum antiferromagnets. *Phys. Rev. B*, 83:100405, Mar 2011.

[9] G. Quirion, M. Lapointe-Major, M. Poirier, J. A. Quilliam, Z. L. Dun, and H. D. Zhou. Magnetic phase diagram of $Ba_3CoSb_2O_9$ as determined by ultrasound velocity measurements. *Phys. Rev. B*, 92:014414, Jul 2015.

[10] M. L. Plumer, A. Caillé, and Kevin Hood. Multicritical points in the magnetic phase diagrams of axial and planar antiferromagnets. *Phys. Rev. B*, 39:4489–4499, Mar 1989.

[11] Daisuke Yamamoto, Giacomo Marmorini, and Ippei Danshita. Magnetization process of spin-1/2 Heisenberg antiferromagnets on a layered triangular lattice. *Journal of the Physical Society of Japan*, 85(2):024706, 2016.

[12] R. Moessner and A. P. Ramirez. Geometrical frustration. *Phys. Today*, 59:24, 2006.

[13] A P Ramirez. Strongly geometrically frustrated magnets. *Annual Review of Materials Science*, 24(1):453–480, 1994.

[14] J Wosnitza, S A Zvyagin, and S Zherlitsyn. Frustrated magnets in high magnetic fields-selected examples. *Reports on Progress in Physics*, 79(7):074504, 2016.

[15] C. Lacroix, P. Mendels, and F. Mila. *Introduction to Frustrated Magnetism: Materials, Experiments, Theory*. Springer Series in Solid-State Sciences. Springer Berlin Heidelberg, 2011.

[16] H T Diep. *Frustrated Spin Systems*. WORLD SCIENTIFIC, 2nd edition, 2013.

[17] S. Blundell. *Magnetism in Condensed Matter*. Oxford Master Series in Condensed Matter Physics. OUP Oxford, 2001.

[18] Patrick A. Lee. An end to the drought of quantum spin liquids. *Science*, 321(5894):1306–1307, 2008.

[19] Leon Balents. Spin liquids in frustrated magnets. *Nature*, 464(7286):199–208, 3 2010.

[20] Yi Zhou, Kazushi Kanoda, and Tai-Kai Ng. Quantum spin liquid states. *Rev. Mod. Phys.*, 89:025003, Apr 2017.

[21] Takashi Imai and Young S. Lee. Do quantum spin liquids exist? *Phys. Today*, 69:30, 2016.

[22] Mingxuan Fu, Takashi Imai, Tian-Heng Han, and Young S. Lee. Evidence for a gapped spin-liquid ground state in a kagome Heisenberg antiferromagnet. *Science*, 350(6261):655–658, 2015.

[23] Simeng Yan, David A. Huse, and Steven R. White. Spin-liquid ground state of the $S = 1/2$ kagome Heisenberg antiferromagnet. *Science*, 332(6034):1173–1176, 2011.

[24] Stefan Depenbrock, Ian P. McCulloch, and Ulrich Schollwöck. Nature of the spin-liquid ground state of the $S = 1/2$ Heisenberg model on the kagome lattice. *Phys. Rev. Lett.*, 109:067201, Aug 2012.

[25] Tian-Heng Han, Joel S. Helton, Shaoyan Chu, Daniel G. Nocera, Jose A. Rodriguez-Rivera, Collin Broholm, and Young S. Lee. Fractionalized excitations in the spin-liquid state of a kagome-lattice antiferromagnet. *Nature*, 492(7429):406–410, 2012.

[26] J. S. Gardner, S. R. Dunsiger, B. D. Gaulin, M. J. P. Gingras, J. E. Greedan, R. F. Kiefl, M. D. Lumsden, W. A. MacFarlane, N. P. Raju, J. E. Sonier, I. Swainson, and Z. Tun. Cooperative paramagnetism in the geometrically frustrated pyrochlore antiferromagnet $Tb_2Ti_2O_7$. *Phys. Rev. Lett.*, 82:1012–1015, Feb 1999.

[27] M. J. P. Gingras, B. C. den Hertog, M. Faucher, J. S. Gardner, S. R. Dunsiger, L. J. Chang, B. D. Gaulin, N. P. Raju, and J. E. Greedan. Thermodynamic and single-ion properties of Tb^{3+} within the collective paramagnetic-spin liquid state of the frustrated pyrochlore antiferromagnet $Tb_2Ti_2O_7$. *Phys. Rev. B*, 62:6496–6511, Sep 2000.

[28] J. S. Gardner, B. D. Gaulin, A. J. Berlinsky, P. Waldron, S. R. Dunsiger, N. P. Raju, and J. E. Greedan. Neutron scattering studies of the cooperative paramagnet pyrochlore $Tb_2Ti_2O_7$. *Phys. Rev. B*, 64:224416, Nov 2001.

[29] T. Fennell, M. Kenzelmann, B. Roessli, H. Mutka, J. Ollivier, M. Ruminy, U. Stuhr, O. Zaharko, L. Bovo, A. Cervellino, M. K. Haas, and R. J. Cava. Magnetoelastic excitations in the pyrochlore spin liquid $Tb_2Ti_2O_7$. *Phys. Rev. Lett.*, 112:017203, Jan 2014.

[30] Joseph A. M. Paddison, Marcus Daum, Zhiling Dun, Georg Ehlers, Yaohua Liu, Matthew B. Stone, Haidong Zhou, and Martin Mourigal. Continuous excitations of the triangular-lattice quantum spin liquid $YbMgGaO_4$. *Nature Physics*,

13(2):117–122, 2017.

[31] Yuesheng Li, Devashibhai Adroja, Pabitra K. Biswas, Peter J. Baker, Qian Zhang, Juanjuan Liu, Alexander A. Tsirlin, Philipp Gegenwart, and Qingming Zhang. Muon spin relaxation evidence for the U(1) quantum spin-liquid ground state in the triangular antiferromagnet $YbMgGaO_4$. *Phys. Rev. Lett.*, 117:097201, Aug 2016.

[32] Yuesheng Li, Devashibhai Adroja, Robert I. Bewley, David Voneshen, Alexander A. Tsirlin, Philipp Gegenwart, and Qingming Zhang. Crystalline electric-field randomness in the triangular lattice spin-liquid $YbMgGaO_4$. *Phys. Rev. Lett.*, 118:107202, Mar 2017.

[33] F. Alex Cevallos, Karoline Stolze, and Robert J. Cava. Structural disorder and elementary magnetic properties of triangular lattice $ErMgGaO_4$ single crystals. *Solid State Communications*, 276:5–8, 2018.

[34] Y. Cai, C. Lygouras, G. Thomas, M. N. Wilson, J. Beare, S. Sharma, C. A. Marjerrison, D. R. Yahne, K. A. Ross, Z. Gong, Y. J. Uemura, H. A. Dabkowska, and G. M. Luke. μSR study of the triangular Ising antiferromagnet $ErMgGaO_4$. *Phys. Rev. B*, 101:094432, Mar 2020.

[35] J. D. Bernal and R. H. Fowler. A theory of water and ionic solution, with particular reference to hydrogen and hydroxyl ions. *The Journal of Chemical Physics*, 1(8):515–548, 1933.

[36] M. J. Harris, S. T. Bramwell, D. F. McMorrow, T. Zeiske, and K. W. Godfrey. Geometrical frustration in the ferromagnetic pyrochlore $Ho_2Ti_2O_7$. *Phys. Rev. Lett.*, 79:2554–2557, Sep 1997.

[37] S. T. Bramwell, M. J. Harris, B. C. den Hertog, M. J. P. Gingras, J. S. Gardner, D. F. McMorrow, A. R. Wildes, A. L. Cornelius, J. D. M. Champion, R. G. Melko, and T. Fennell. Spin correlations in $Ho_2Ti_2O_7$: A dipolar spin ice system. *Phys. Rev. Lett.*, 87:047205, Jul 2001.

[38] A. P. Ramirez, A. Hayashi, R. J. Cava, R. Siddharthan, and B. S. Shastry. Zero-point entropy in 'spin ice'. *Nature*, 399(6734):333–335, 1999.

[39] T. Fennell, O.A. Petrenko, G. Balakrishnan, S.T. Bramwell, J.D.M. Champion, B. Fåk, M.J. Harris, and D.McK. Paul. Field-induced partial order in the spin ice dysprosium titanate. *Applied Physics A*, 74(1):s889–s891, Dec 2002.

[40] Hiroaki Kadowaki, Yoshinobu Ishii, Kazuyuki Matsuhira, and Yukio Hinatsu. Neutron scattering study of dipolar spin ice $Ho_2Sn_2O_7$: frustrated pyrochlore magnet. *Phys. Rev. B*, 65:144421, Mar 2002.

[41] T. Ono, H. Tanaka, H. Aruga Katori, F. Ishikawa, H. Mitamura, and T. Goto. Magnetization plateau in the frustrated quantum spin system Cs_2CuBr_4. *Phys. Rev. B*, 67:104431, Mar 2003.

[42] N. A. Fortune, S. T. Hannahs, Y. Yoshida, T. E. Sherline, T. Ono, H. Tanaka, and Y. Takano. Cascade of magnetic-field-induced quantum phase transitions in a spin-$\frac{1}{2}$ triangular-lattice antiferromagnet. *Phys. Rev. Lett.*, 102:257201, Jun 2009.

[43] H. Tsujii, C. R. Rotundu, T. Ono, H. Tanaka, B. Andraka, K. Ingersent, and Y. Takano. Thermodynamics of the up-up-down phase of the $S = \frac{1}{2}$ triangular-lattice antiferromagnet Cs_2CuBr_4. *Phys. Rev. B*, 76:060406, Aug 2007.

[44] M. Kenzelmann, G. Lawes, A. B. Harris, G. Gasparovic, C. Broholm, A. P. Ramirez, G. A. Jorge, M. Jaime, S. Park, Q. Huang, A. Ya. Shapiro, and L. A.

Demianets. Direct transition from a disordered to a multiferroic phase on a triangular lattice. *Phys. Rev. Lett.*, 98:267205, Jun 2007.

[45] J. S. White, Ch. Niedermayer, G. Gasparovic, C. Broholm, J. M. S. Park, A. Ya. Shapiro, L. A. Demianets, and M. Kenzelmann. Multiferroicity in the generic easy-plane triangular lattice antiferromagnet $RbFe(MoO_4)_2$. *Phys. Rev. B*, 88:060409, Aug 2013.

[46] Yutaka Shirata, Hidekazu Tanaka, Akira Matsuo, and Koichi Kindo. Experimental realization of a spin-1/2 triangular-lattice Heisenberg antiferromagnet. *Phys. Rev. Lett.*, 108:057205, Jan 2012.

[47] H. D. Zhou, Cenke Xu, A. M. Hallas, H. J. Silverstein, C. R. Wiebe, I. Umegaki, J. Q. Yan, T. P. Murphy, J.-H. Park, Y. Qiu, J. R. D. Copley, J. S. Gardner, and Y. Takano. Successive phase transitions and extended spin-excitation continuum in the $S{=}\frac{1}{2}$ triangular-lattice antiferromagnet $Ba_3CoSb_2O_9$. *Phys. Rev. Lett.*, 109:267206, Dec 2012.

[48] M. L. Plumer, Kevin Hood, and A. Caillé. Multicritical point in the magnetic phase diagram of $CsNiCl_3$. *Phys. Rev. Lett.*, 60:45–48, Jan 1988.

[49] Xiaodong Zhu and M. B. Walker. Phenomenological theory of the magnetic transitions in $CsNiCl_3$. *Phys. Rev. B*, 36:3830–3832, Sep 1987.

[50] G. Quirion, X. Han, M. L. Plumer, and M. Poirier. First order phase transition in the frustrated triangular antiferromagnet $CsNiCl_3$. *Phys. Rev. Lett.*, 97:077202, Aug 2006.

[51] G. Quirion, X. Han, and M. L. Plumer. Magnetoelastic coupling within a Landau model of phase transitions: Application to the frustrated triangular antiferromagnet $CsNiCl_3$. *Phys. Rev. B*, 84:014408, Jul 2011.

[52] R. Ishii, S. Tanaka, K. Onuma, Y. Nambu, M. Tokunaga, T. Sakakibara, N. Kawashima, Y. Maeno, C. Broholm, D. P. Gautreaux, J. Y. Chan, and S. Nakatsuji. Successive phase transitions and phase diagrams for the quasi-two-dimensional easy-axis triangular antiferromagnet $Rb_4Mn(MoO_4)_3$. *EPL (Europhysics Letters)*, 94(1):17001, Mar 2011.

[53] Hironori Yamaguchi, Shojiro Kimura, Rieko Ishii, Satoru Nakatsuji, and Masayuki Hagiwara. Electron spin resonance in the quasi-two-dimensional triangular-lattice antiferromagnet $Rb_4Mn(MoO_4)_3$. *Journal of the Physical Society of Japan*, 80(6):064705, 2011.

[54] T. Ono, H. Tanaka, H. Aruga Katori, F. Ishikawa, H. Mitamura, and T. Goto. Magnetization plateau in the frustrated quantum spin system Cs_2CuBr_4. *Phys. Rev. B*, 67:104431, Mar 2003.

[55] H. Tsujii, C. R. Rotundu, T. Ono, H. Tanaka, B. Andraka, K. Ingersent, and Y. Takano. Thermodynamics of the up-up-down phase of the $S = \frac{1}{2}$ triangular-lattice antiferromagnet Cs_2CuBr_4. *Phys. Rev. B*, 76:060406, Aug 2007.

[56] Jason Alicea, Andrey V. Chubukov, and Oleg A. Starykh. Quantum stabilization of the 1/3-magnetization plateau in Cs_2CuBr_4. *Phys. Rev. Lett.*, 102:137201, Mar 2009.

[57] L. E. Svistov, A. I. Smirnov, L. A. Prozorova, O. A. Petrenko, L. N. Demianets, and A. Ya. Shapiro. Quasi-two-dimensional antiferromagnet on a triangular lattice $RbFe(MoO_4)_2$. *Phys. Rev. B*, 67:094434, Mar 2003.

[58] L.A. Prozorova, L.E. Svistov, A.I. Smirnov, O.A. Petrenko, L.N. Demianets, and A.Ya. Shapiro. Triangular lattice antiferromagnet $RbFe(MoO_4)_2$ in an applied

magnetic field. *Journal of Magnetism and Magnetic Materials*, 258-259:394 – 397, 2003. Second Moscow International Symposium on Magnetism.

[59] L. E. Svistov, A. I. Smirnov, L. A. Prozorova, O. A. Petrenko, A. Micheler, N. Büttgen, A. Ya. Shapiro, and L. N. Demianets. Magnetic phase diagram, critical behavior, and two-dimensional to three-dimensional crossover in the triangular lattice antiferromagnet $RbFe(MoO_4)_2$. *Phys. Rev. B*, 74:024412, Jul 2006.

[60] A. I. Smirnov, H. Yashiro, S. Kimura, M. Hagiwara, Y. Narumi, K. Kindo, A. Kikkawa, K. Katsumata, A. Ya. Shapiro, and L. N. Demianets. Triangular lattice antiferromagnet $RbFe(MoO_4)_2$ in high magnetic fields. *Phys. Rev. B*, 75:134412, Apr 2007.

[61] J L Ribeiro and J M Perez-Mato. Symmetry and magnetic field driven transitions in the 2D triangular lattice compound $RbFe(MoO_4)_2$. *Journal of Physics: Condensed Matter*, 23(44):446003, Oct 2011.

[62] H. Mitamura, R. Watanuki, K. Kaneko, N. Onozaki, Y. Amou, S. Kittaka, R. Kobayashi, Y. Shimura, I. Yamamoto, K. Suzuki, S. Chi, and T. Sakakibara. Spin-chirality-driven ferroelectricity on a perfect triangular lattice antiferromagnet. *Phys. Rev. Lett.*, 113:147202, Oct 2014.

[63] A. I. Smirnov, T. A. Soldatov, O. A. Petrenko, A. Takata, T. Kida, M. Hagiwara, A. Ya. Shapiro, and M. E. Zhitomirsky. Order by quenched disorder in the model triangular antiferromagnet $RbFe(MoO_4)_2$. *Phys. Rev. Lett.*, 119:047204, Jul 2017.

[64] Yoshihiro Doi, Yukio Hinatsu, and Kenji Ohoyama. Structural and magnetic properties of pseudo-two-dimensional triangular antiferromagnets

$Ba_3MSb_2O_9$(M = Mn, Co, and Ni). *Journal of Physics: Condensed Matter*, 16(49):8923, 2004.

[65] A. Sera, Y. Kousaka, J. Akimitsu, M. Sera, T. Kawamata, Y. Koike, and K. Inoue. $S = \frac{1}{2}$ triangular-lattice antiferromagnets $Ba_3CoSb_2O_9$ and $CsCuCl_3$: Role of spin-orbit coupling, crystalline electric field effect, and Dzyaloshinskii-Moriya interaction. *Phys. Rev. B*, 94:214408, Dec 2016.

[66] J. Ma, Y. Kamiya, Tao Hong, H. B. Cao, G. Ehlers, W. Tian, C. D. Batista, Z. L. Dun, H. D. Zhou, and M. Matsuda. Static and dynamical properties of the spin-1/2 equilateral triangular-lattice antiferromagnet $Ba_3CoSb_2O_9$. *Phys. Rev. Lett.*, 116:087201, Feb 2016.

[67] Villain, J., Bidaux, R., Carton, J.-P., and Conte, R. Order as an effect of disorder. *J. Phys. France*, 41(11):1263–1272, 1980.

[68] Christopher L. Henley. Ordering due to disorder in a frustrated vector antiferromagnet. *Phys. Rev. Lett.*, 62:2056–2059, Apr 1989.

[69] Yukitoshi Motome, Karlo Penc, and Nic Shannon. Monte Carlo study of half-magnetization plateau and magnetic phase diagram in pyrochlore antiferromagnetic Heisenberg model. *Journal of Magnetism and Magnetic Materials*, 300(1):57 – 61, 2006. The third Moscow International Symposium on Magnetism 2005.

[70] Fa Wang and Ashvin Vishwanath. Spin phonon induced collinear order and magnetization plateaus in triangular and kagome antiferromagnets: Applications to $CuFeO_2$. *Phys. Rev. Lett.*, 100:077201, Feb 2008.

[71] Doron L. Bergman, Ryuichi Shindou, Gregory A. Fiete, and Leon Balents. Models of degeneracy breaking in pyrochlore antiferromagnets. *Phys. Rev. B*, 74:134409, Oct 2006.

[72] Karlo Penc, Nic Shannon, and Hiroyuki Shiba. Half-magnetization plateau stabilized by structural distortion in the antiferromagnetic Heisenberg model on a pyrochlore lattice. *Phys. Rev. Lett.*, 93:197203, Nov 2004.

[73] M. L. Plumer. Magnetoelastic coupling in helimagnets: A molecular-field theory of the 1/4 lock-in phase of holmium. *Phys. Rev. B*, 44:12376–12381, Dec 1991.

[74] Daisuke Yamamoto, Giacomo Marmorini, and Ippei Danshita. Microscopic model calculations for the magnetization process of layered triangular-lattice quantum antiferromagnets. *Phys. Rev. Lett.*, 114:027201, Jan 2015.

[75] Hikaru Kawamura and Seiji Miyashita. Phase transition of the Heisenberg antiferromagnet on the triangular lattice in a magnetic field. *Journal of the Physical Society of Japan*, 54(12):4530–4538, 1985.

[76] Hikaru Kawamura. Spin-wave analysis of the antiferromagnetic plane rotator model on the triangular latticesymmetry breaking in a magnetic field. *Journal of the Physical Society of Japan*, 53(8):2452–2455, 1984.

[77] G. Koutroulakis, T. Zhou, Y. Kamiya, J. D. Thompson, H. D. Zhou, C. D. Batista, and S. E. Brown. Quantum phase diagram of the $S = \frac{1}{2}$ triangular-lattice antiferromagnet $Ba_3CoSb_2O_9$. *Phys. Rev. B*, 91:024410, Jan 2015.

[78] S.Ya Istomin, V.A Koutcenko, E.V Antipov, F Lindberg, and G Svensson. Synthesis and characterization of novel 6-H perovskites $Ba_2Co_{2-x}Sb_xO_{6-y}$, $0.6 \leq x \leq 0.8$ and $x = 1.33$ ($Ba_3CoSb_2O_9$). *Materials Research Bulletin*, 39(7):1013 – 1022, 2004.

[79] M. T. Heinilä and A. S. Oja. Selection of the ground state in type-I fcc antiferromagnets in an external magnetic field. *Phys. Rev. B*, 48:7227–7237, Sep 1993.

[80] X. Z. Liu, O. Prokhnenko, D. Yamamoto, M. Bartkowiak, N. Kurita, and H. Tanaka. Microscopic evidence of a quantum magnetization process in the $S = \frac{1}{2}$ triangular-lattice Heisenberg-like antiferromagnet $Ba_3CoSb_2O_9$. *Phys. Rev. B*, 100:094436, Sep 2019.

[81] J. C. Tolédano and P. Tolédano. *The Landau Theory of Phase Transitions*. WORLD SCIENTIFIC, 1987.

[82] M. L. Plumer and A. Caillé. Nonlocal Landau free-energy functional: Application to the magnetic phase transition in $CsNiF_3$. *Phys. Rev. B*, 37:7712–7725, May 1988.

[83] G. Quirion, X. Han, and M. L. Plumer. Magnetoelastic coupling within a Landau model of phase transitions: Application to the frustrated triangular antiferromagnet $csnicl_3$. *Phys. Rev. B*, 84:014408, Jul 2011.

[84] M. L. Plumer and A. Caillé. Magnetic phase diagrams of the antiferromagnetic planar model on a stacked triangular lattice. *Phys. Rev. B*, 42:10388–10396, Dec 1990.

[85] J. Goodyear and D. J. Kennedy. The crystal structure of $CsMnBr_3$. *Acta Crystallographica Section B*, 28(5):1640–1641, May 1972.

[86] B. D. Gaulin, M. F. Collins, and W. J. L. Buyers. Spin waves in the triangular antiferromagnet $CsMnBr_3$. *Journal of Applied Physics*, 61(8):3409–3411, 1987.

[87] M. L. Plumer and A. Caillé. Landau theory of the magnetic phase diagram of $CsMnBr_3$. *Phys. Rev. B*, 41:2543–2546, Feb 1990.

[88] B. D. Gaulin, T. E. Mason, M. F. Collins, and J. Z. Larese. Tetracritical behavior of $CsMnBr_3$. *Phys. Rev. Lett.*, 62:1380–1383, Mar 1989.

[89] G. Quirion, X. Han, M. L. Plumer, and M. Poirier. First order phase transition in the frustrated triangular antiferromagnet $CsNiCl_3$. *Phys. Rev. Lett.*, 97:077202, Aug 2006.

[90] T Ono, H Tanaka, O Kolomiyets, H Mitamura, T Goto, K Nakajima, A Oosawa, Y Koike, K Kakurai, J Klenke, P Smeibidle, and M Meißner. Magnetization plateaux of the S = 1/2 two-dimensional frustrated antiferromagnet Cs_2CuBr_4. *Journal of Physics: Condensed Matter*, 16(11):S773, 2004.

[91] Y. Fujii, T. Nakamura, H. Kikuchi, M. Chiba, T. Goto, S. Matsubara, K. Kodama, and M. Takigawa. NMR study of $S = 1/2$ quasi-two-dimensional antiferromagnet Cs_2CuBr_4. *Physica B: Condensed Matter*, 346-347:45–49, 2004. Proceedings of the 7th International Symposium on Research in High Magnetic Fields.

[92] A Honecker, J Schulenburg, and J Richter. Magnetization plateaus in frustrated antiferromagnetic quantum spin models. *Journal of Physics: Condensed Matter*, 16(11):S749, 2004.

[93] Shin-ichiro Yoshikawa, Kouichi Okunishi, Makoto Senda, and Seiji Miyashita. Quantum fluctuation-induced phase transition in S = 1/2 XY-like Heisenberg antiferromagnets on the triangular lattice. *Journal of the Physical Society of Japan*, 73(7):1798–1804, 2004.

[94] O. Gtze, J. Richter, R. Zinke, and D.J.J. Farnell. Ground-state properties of the triangular-lattice Heisenberg antiferromagnet with arbitrary spin quantum number s. *Journal of Magnetism and Magnetic Materials*, 397:333 – 341, 2016.

[95] D. H. Lee, J. D. Joannopoulos, J. W. Negele, and D. P. Landau. Symmetry analysis and Monte Carlo study of a frustrated antiferromagnetic planar (XY) model in two dimensions. *Phys. Rev. B*, 33:450–475, Jan 1986.

[96] Seiji Miyashita. Magnetic properties of Ising-like Heisenberg antiferromagnets on the triangular lattice. *Journal of the Physical Society of Japan*, 55(10):3605–3617, 1986.

[97] J. A. Oyedele and M. F. Collins. Theory of spin waves in triangular antiferromagnets. *Canadian Journal of Physics*, 56(11):1482–1487, 1978.

[98] M. E. Zhitomirsky. (Private communication). 2019.

[99] J. A. Nelder and R. Mead. A Simplex Method for Function Minimization. *The Computer Journal*, 7(4):308–313, 01 1965.

[100] N.B. Ekreem, A.G. Olabi, T. Prescott, A. Rafferty, and M.S.J. Hashmi. An overview of magnetostriction, its use and methods to measure these properties. *Journal of Materials Processing Technology*, 191(1):96 – 101, 2007. Advances in Materials and Processing Technologies, July 30th - August 3rd 2006, Las Vegas, Nevada.

[101] N.H. Balshaw and Oxford Instruments Group. Scientific Research Division. *Practical Cryogenics: An Introduction to Laboratory Cryogenics*. Oxford Instruments, Scientific Research Division, 1996.

[102] G. Quirion, C. Bidaud, J. A. Quilliam, P. Lejay, V. Simonet, and R. Ballou. Experimental evidence of symmetry breaking in the multiferroic $Ba_3NbFe_3Si_2O_{14}$ using sound velocity measurements. *Phys. Rev. B*, 96:134433, Oct 2017.

[103] D. Royer E. Dieulesaint. *Elastic Waves in Solids*. John Wiley and Sons Ltd., Chichester, 1980.

[104] J.A. Rayne, J.G. Collins, and G.K. White. Low temperature magnetostriction studies in $CsNiCl_3$. *Solid State Communications*, 45(8):681 – 683, 1983.

[105] Saya Ito, Nobuyuki Kurita, Hidekazu Tanaka, Seiko Ohira-Kawamura, Kenji Nakajima, Shinichi Itoh, Keitaro Kuwahara, and Kazuhisa Kakurai. Structure of the magnetic excitations in the spin-1/2 triangular-lattice Heisenberg antiferromagnet $Ba_3CoSb_2O_9$. *Nature Communications*, 8(1):235, 2017.

[106] Y. Kamiya, L. Ge, Tao Hong, Y. Qiu, D. L. Quintero-Castro, Z. Lu, H. B. Cao, M. Matsuda, E. S. Choi, C. D. Batista, M. Mourigal, H. D. Zhou, and J. Ma. The nature of spin excitations in the one-third magnetization plateau phase of $Ba_3CoSb_2O_9$. *Nature Communications*, 9(1):2666, 2018.

[107] Seizo Watarai, Seiji Miyashita, and Hiroyuki Shiba. Entropy effect on the magnetization process of hexagonal XY-like Heisenberg antiferromagnets. *Journal of the Physical Society of Japan*, 70(2):532–537, 2001.

[108] Seiji MIYASHITA. Phase transition in spin systems with various types of fluctuations. *Proceedings of the Japan Academy, Series B*, 86(7):643–666, 2010.

Appendix A

Effective elastic constant matrix C^*

In order to determine the general formula of the effective elastic constant C^*, Eq. 7.1, we first define the free energy as the function of strain e and the variable Q:

$$F = F(e_\alpha, Q_\beta), \tag{A.1}$$

where α, $\beta = 1 \sim 6$ in Voigt notation. Considering the total second derivative of F respect to e_α and e_β, we give

$$\begin{aligned} C^*_{\alpha\beta} &= \frac{d^2F}{de_\alpha de_\beta} \\ &= \frac{d}{de_\beta}\left(\frac{\partial F}{\partial e_\alpha} + \sum_\eta \frac{dQ_\eta}{de_\alpha}\frac{\partial F}{\partial Q_\beta}\right) \\ &= \left(\frac{\partial}{\partial e_\beta} + \sum_\eta \frac{dQ_\eta}{de_\beta}\frac{\partial}{\partial Q_\eta}\right)\left(\frac{\partial F}{\partial e_\alpha} + \sum_\eta \frac{dQ_\gamma}{de_\alpha}\frac{\partial F}{\partial Q_\gamma}\right). \end{aligned} \tag{A.2}$$

Since $\partial F/\partial Q_\gamma = 0$ at equilibrium, we obtain

$$C^*_{\alpha\beta} = C_{\alpha\beta} + \sum_\eta \frac{dQ_\eta}{de_\beta}\frac{\partial^2 F}{\partial e_\alpha \partial Q_\eta}, \tag{A.3}$$

where $C_{\alpha\beta} = \partial^2 F/(\partial e_\alpha \partial e_\beta)$ is the bare elastic constants. In order to generate the expression of dQ_η/de_β, we use $\frac{d}{de_\alpha}(\partial F/\partial Q_\beta) = 0$ to get the equations:

$$\begin{aligned}\frac{d}{de_\alpha}\left(\frac{\partial F}{\partial Q_\beta}\right) &= \left(\frac{\partial}{\partial e_\alpha} + \sum_\eta \frac{dQ_\eta}{de_\alpha}\frac{\partial}{\partial Q_\eta}\right)\left(\frac{\partial F}{\partial Q_\beta}\right) \\ &= \frac{\partial^2 F}{\partial e_\alpha \partial Q_\beta} + \sum_\eta \frac{dQ_\eta}{de_\alpha}\frac{\partial^2 F}{\partial Q_\beta \partial Q_\eta} \\ &= 0.\end{aligned} \tag{A.4}$$

Writing Eq. A.4 in matrix form, we have

$$\hat{R} + \hat{M}\hat{P} = 0. \tag{A.5}$$

Here $\hat{M}$ is a 6×6 matrix, $\hat{P}$ and $\hat{R}$ are 6×1 column vectors with fixed α, as shown

$$\hat{M} = \begin{pmatrix} \frac{\partial^2 F}{\partial Q_1 \partial Q_1} & \frac{\partial^2 F}{\partial Q_1 \partial Q_2} & \cdot & \cdot & \cdot & \\ \frac{\partial^2 F}{\partial Q_1 \partial Q_2} & \frac{\partial^2 F}{\partial Q_2 \partial Q_2} & & & & \\ \cdot & & \cdot & & & \\ \cdot & & & \cdot & & \\ \cdot & & & & \cdot & \\ & & & & & \frac{\partial^2 F}{\partial Q_6 \partial Q_6} \end{pmatrix}, \tag{A.6}$$

$$\hat{P} = \begin{pmatrix} \frac{dQ_1}{de_\alpha} \\ \frac{dQ_2}{de_\alpha} \\ \cdot \\ \cdot \\ \cdot \\ \frac{dQ_6}{de_\alpha} \end{pmatrix}, \qquad \hat{R} = \begin{pmatrix} \frac{\partial^2 F}{\partial e_\alpha \partial Q_1} \\ \frac{\partial^2 F}{\partial e_\alpha \partial Q_2} \\ \cdot \\ \cdot \\ \cdot \\ \frac{\partial^2 F}{\partial e_\alpha \partial Q_6} \end{pmatrix}.$$

Therefore, the solution of the elements of $\hat{P}$ is

$$\hat{P}_\eta = \frac{D_\eta}{D}, \tag{A.7}$$

where D is the determent of $\hat{M}$, and D_η is the determent of the matrix which is generated by substituting the column vector $-\hat{R}$ for the ηth column of $\hat{M}$. Finally, including α, we derive the general formula of the effective elastic constant

$$C^*_{\alpha\beta} = C_{\alpha\beta} + \sum_\eta \hat{P}_{\alpha\eta}\hat{M}_{\beta\eta}. \tag{A.8}$$